THE UNIVERSITY OF CHICAGO

DEFINING MYOSIN-10 NAVIGATION RULES

A DISSERTATION SUBMITTED TO
THE FACULTY OF THE DIVISION OF THE BIOLOGICAL SCIENCES
AND THE PRITZKER SCHOOL OF MEDICINE
IN CANDIDACY FOR THE DEGREE OF
DOCTOR OF PHILOSOPHY

DEPARTMENT OF BIOCHEMISTRY AND MOLECULAR BIOLOGY

BY
KEVIN CHRISTOPHER VAVRA

CHICAGO, ILLINOIS
AUGUST 2016

CONTENTS

LIST OF FIGURES

LIST OF TABLES

ABBREVATIONS

aa	amino acid(s)
CD	Circular Dichroism
HMM	Heavy Meromyosin
M5CC	Myosin-5 Coiled-coil
M10CC	Myosin-10 Coiled-coil
PH	Pleckstrin Homology
SAH	Single-Alpha Helix
SAXS	Small-Angle X-ray Scattering
SEC-SAXS	Size-exclusion chromatography Small-Angle X-ray Scattering
TIRF	Total internal reflection fluorescent

ACKNOWLEDGMENTS

A considerable about of effort went into the work presented in this thesis, and there are many people who supported me throughout my graduate studies. First, I'd like to thank Ronald Rock for supporting me as a thesis advisor and for letting me explore a variety of biochemistry techniques I was curious about early in my career. Granting me freedom to utilize NMR and SAXS allowed for a successful project, and Ron connected with internal and external collaborators to provide me with the machinery and technical education needed for this thesis. He also joined me on the front line when I was learning more about each of the different techniques, software packages, and technical limitations. My time in his lab has set me up for a strong start as a research scientist, and I am grateful for all the learning opportunities he provided me. I would also like to thank Ron for his support in my personal and professional development throughout my time in his lab.

I would also like to thank the other members of the Rock Lab for their support throughout my thesis research. Ala Santos was in the lab when I started and taught me biochemistry techniques used in our lab. Agata Krenc and I joined Ron's lab at the same time, and we always supported each other throughout the process. Marie Wu was a positive and fun undergraduate student in our lab and I had the pleasure to work closely with her to develop a research project. Joanna Kalita was a strong lab manager who added the right amount of humor to science. Caitlin Sullivan Trejo acted as the senior graduate student in our lab and always contributed biophysical perspectives on our projects. Benjamin Zalisko answered many of our chemistry questions and provided great group discussions in our lab meetings. Lastly, we had a group of Polish masters students who I am glad to have spent a year with each of them: Ewa Warchol, Natalia Zapiorkowska, Lukasz Truszkowski, Jagoda Rokicka, and Natalia Plewa.

Members of many other labs provided significant support during my graduate students at The University of Chicago. Muriel Laine, Alison Zarnke and Brad Green from Geoffrey Greene's group were a group of people who I spent a summer research rotation with and

often visited with after the end of my rotation. The entirety of Robert Keenan's group provided suggestions, knowledge and assistance during our studies and I am grateful to the equipment and space sharing agreements that the Rock and Keenan labs have. I am grateful to Claire Atkinson, Brittney McClymonds, Agnieszka Mateja, Phil McGilvray, Matt Wohlever, Andrei Anghel, Marta Borowska, and Gosia Macias for their scientific support and camaraderie. Lydia Blachowicz, Matthew Pond, Brigitte Ziervogel and Shelly Wright from Benoit Roux's group provided additional scientific support in this thesis and made coming into lab in the early morning a pleasure. Many other members of the Adams, Sosnick, Rice, and Perozo labs were also people with whom I shared the pleasure of working with every day.

The work presented in this thesis was enhanced by the support of collaborators and faculty. Youlin Xia, Gianluigi Veglia and members of the University of Minnesota NMR community were a great group of collaborators who I met and worked closely with over the course of this project. Scientists at beamlines 12 and 18 of the Advanced Photon Source at Argonne National Laboratory, in particular Srinivas Chakravarthy, provided support for SAXS data collection. My thesis committee members Tobin Sosnick, Erin Adams and David Kovar provided feedback and strengthened the scope and depth of the findings presented in this research. I thank everyone above for their help and feedback throughout this process.

Graduate school started with our group of six Biochemistry and Molecular Biology students, and I would like to thank Agata Krenc, Alex French, James Fuller, Jenny Lin, and Kate Malecek for their friendship during the past six years. I would also like to thank everyone else I met at the University of Chicago during this time, especially the Triathlon and Master Swimming Teams. I met many awesome people through running, swimming and biking here and around the country. This achievement could not be completed without the support and friendship of many, including Eric Dudiak, Lauren Spiegel, Kevin Ziegler, Shruti Gupta, Brandon Goldberg, Jennifer Steeb, Mike Gleason, and Jeremy Frank Olechnowicz, and Alex Murray.

Lastly, I would like to thank my family for their support during my research, studies, and adventures. Thank you to my mom and dad for supporting me from day one and visiting me everywhere I have lived. Thank you also to Margot Vavra, Diane Palecek, Jerry Palecek, Whitney Watson, Chase Watson, Jim Masturzo, and Jenny Vavra for listening and gathering for memorable celebrations around the country. And I would like to thank my partner, Cesar Favila, for his patience and support throughout the research and dissertation steps. I could not have done it without you all, so thank you and I love you all.

ABSTRACT

Myosin-10 an unconventional myosin motor that localizes to tips of filopodia, long finger-like projections from cells, to help relocate its cargo proteins to the tips and bodies of filopodia. While it is known that myosin-10 moves along filopodial actin, how myosin-10 specifically selects for filopodial actin tracks is currently unknown. Three research groups attempted to determine myosin-10's track selection ability using single molecule techniques to measure myosin-10 actin bundle selection behavior. Due to the low dimerization affinity for myosin-10 without a high local motor concentration encouraged by cargo binding, additional nucleation domains were needed to be attached to shortened constructs with the regulatory cargo-binding domains removed. These studies disagreed about myosin-10 track sensitivity because one construct demonstrated clear bundle selection not seen the other two constructs. After these studies were performed, the native myosin-10 coiled-coil structure was solved and showed that all three research groups had inadvertently fused an antiparallel coiled-coil to a parallel coiled-coil. We studied the coiled-coils of the three previously designed constructs to determine the source of different behaviors between constructs and link myosin-10 bundle selection back to full-length wild-type myosin-10. The bundle selective construct, which attempted to create a continuous coiled-coil, forms an antiparallel oriented coiled-coil. Additionally this project tests the flexibility of a single-alpha helix domain connecting the motor domain that binds actin to the coiled-coil to demonstrate how rigidity and orientation of the coiled-coil in myosin-10 leads to actin track selection.

CHAPTER 1

INTRODUCTION TO MYOSIN-10 AND FILOPODIAL LOCALIZATION

1.1 Filopodia as structures for cellular motion and formation of endothelial layers

Filopodia are formed in numerous cells and participate in a variety of cellular functions, particularly cellular motion, adhesion, and environmental sensory [170]. Filopodia are thin, arm-like projections from the cell enriched with bundles composed of parallel, cross-linked networks of actin filaments [16, 101]. At the center of filopodial function is the dynamic nature of filopodia with polymerizing and depolymerizing actin bundles. Many filopodial functions are regulated or mediated by actin polymerization or depolymerization proteins and the motor protein associated with filopodia, myosin-10 [76] . Similarly, the formation of filopodia is mediated by numerous actin-associated proteins that encourage the polymerization of actin, which could also include myosin-10 [165]. Understanding the formation and growth of filopodia requires a better understanding of the underlying cytoskeletal actin inside this cellular projection.

1.1.1 Structure of actin in filopodia and filopodial enrichment of actin bundling proteins

Filopodial actin is comprised of bundled actin, with each bundle typically contains 15-30 cross-linked actin filaments [16, 18, 40, 69, 103]. Actin cross-linking mediated by fascin, which cross-links actin in a parallel orientation, forms bundles [27, 160, 175]. Knockdown of fascin in cells causes a decrease in filopodial formation and a change in filopodial actin structure [108, 160]. Ena/VASP proteins assist with the elongation of actin within the filopodia, by binding actin filaments at the growing, barbed ends of the filaments and enhancing elongation

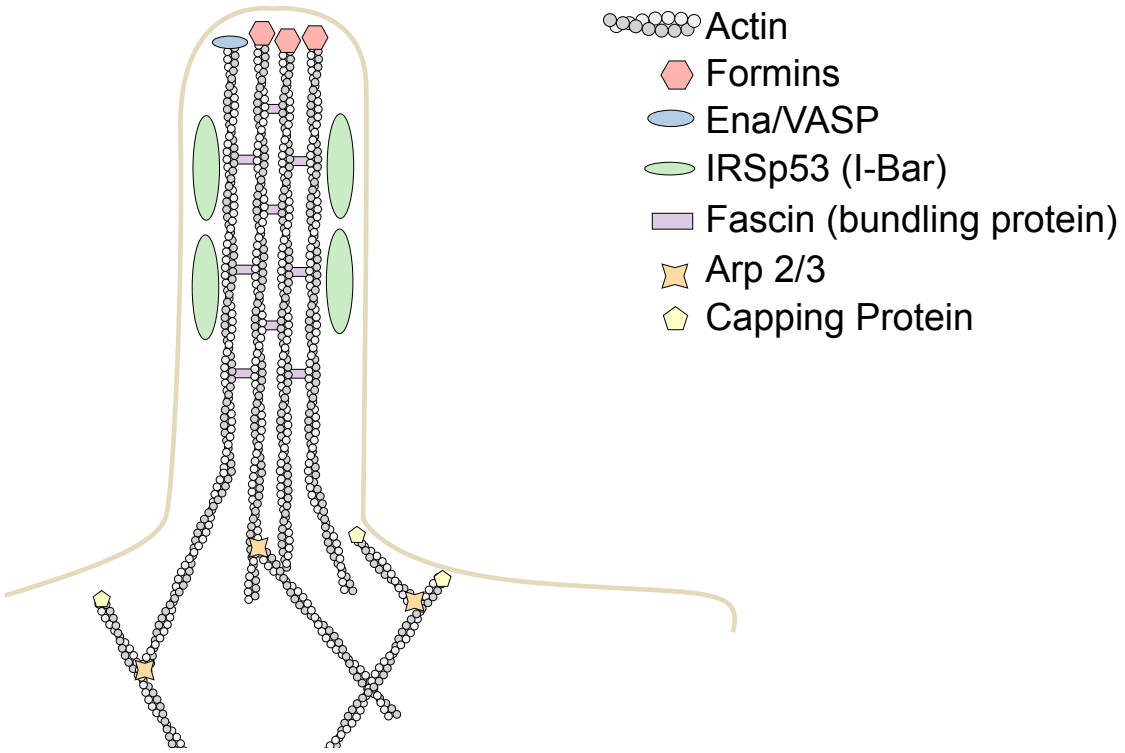

Figure 1.1: Filopodial bundles contain proteins that form the appropriate actin track for myosin-10. Simplified model of actin and proteins recruited in filopodia actin bundle formation. Actin filaments are cross-linked by fascin and other actin-bundling proteins in a parallel orientation so the barbed-ends of filaments point towards the filopodial tip. Ena/VASP and formins localize to the growing ends of the filaments within the bundle to assist with nucleation and polymerization of the actin filaments. IRSp53 is an example of an I-BAR protein that stabilizes the membrane geometry to favor the protruding shape of filopodia. The presence of the bundled actin provides a favorable track for myosin-10 in filopodia, and the formation of this actin results from coordinated functions of multiple proteins.

[57, 145]. Formins also enhance filopodial formation by nucleating actin filaments, and promoting addition of monomers at the barbed end in cooperation with profilin [84, 116, 117, 128, 180]. Ena/VASP and formin proteins play a secondary role in filopodial growth by binding the barbed end of elongating actin. This antagonizes the binding of actin capping proteins, which inhibit actin filament elongation, to the actin barbed ends and prevents actin elongation inhibition [11].

Lastly, the I-BAR protein family is predicted to deform the membrane and form convex membrane protrusions. Membrane protrusions induced solely by *in vivo* I-BAR protein

overexpression take on similar geometries as small filopodia, indicating that the I-BAR proteins could stabilize the membrane structure to a shape that encourages filopodial growth [126]. One studied I-BAR member is IRSp53, which binds lipids and actin in addition to associating with Ena/VASP and formins [2, 132]. I-BAR proteins directly interact with phosphoinositide-rich membranes to form a negative membrane curvature to deform the membrane into a tubular structure [178].

Although a diverse set of proteins initiate and elongate filopodia, the Rho GTPase family drives many pathways in filopodia initiation and growth. RhoGTPases provide the regulation to control the concerted activity of the proteins to lead to controlled filopodial actin formation and depolymerization [124]. Cdc42 is the Rho GTPase most closely associated with increased actin growth leading to filopodial formation [101, 110]. Cdc42 forms a complex with I-bar protein IRSp53 to produce filopodia by directly interacting with proteins associated with actin dynamics and membrane protrusion [86]. IRSp53 interacts with proteins involved in actin elongation, including formin mDia1, Ena/VASP member Mena, and N-WASP (neural Wiskott-Aldrich syndrom protein) [46]. Additionally IRSp53 is associated with signaling proteins WAVE1 and WAVE2 (WASP family verpolin homology), Eps8, and ACK (Cdc42-associated kinase) [4, 46]. Interactions with the signaling proteins by the Cdc42-IRSp53 complex leads to activation of other RhoGTPases associated with actin dynamics in other cellular structures, such as Rac, Rif, and Rho, if these RhoGTPases are not already activated [101, 110]. These proteins all work in a coordinated fashion to create an organized and stable parallel actin bundles that act as tracks for myosin-10, a motor protein enriched in filopodia at filopodial tips explained below. However a good example of the roles played by each protein is the controlled initiation and growth of filopodia.

Initiation of filopodial formation from the cell is a heavily debated topic, and two non-mutually exclusive models are currently proposed to describe this process. The first model, the convergent elongation model, proposes that filopodial growth is initiated by actin branching in lamellipodia by the Arp2/3 complex. The filopodia are predicted to form by fascin-

mediated cross-linking of growing actin filaments, with actin elongation being the driving force in the production of small protrusions [16, 18]. The alternate hypothesis, the tip nucleation model, predicts that formins, proteins implicated in the nucleating and elongation of actin filaments, act as the activating factor in filopodial actin polymerization. Formins, such as Dia2, encourage the nucleation of actin filaments and the elongation occurring at actin barbed ends, eventually pushing the plasma membrane to form filopodia [40, 175]. Both theories demonstrate that the filopodial growth and retraction is regulated by coordinated actin polymerization and cross-linking, which involves numerous proteins acting in a regulated fashion [100, 101, 53].

1.1.2 Function of filopodia

The extension of filopodia from the cell body to the external environment is suggestive of probing or signal detection functions for filopodia. Filopodia act as sensory fingers in neuronal growth cones to sample local environments and locate cellular adhesion sites [43]. The increased membrane surface area of filopodia allows for a larger population of chemical receptors to be located on cellular projections during stimulus detection. Endothelial tip cells noted to produce many filopodia produce longer and more numerous filopodia on top of vascular endothelial growth factor (VEGF-A)-producing astrocytes, with the astrocytes acting as a scaffold for the promotion of filopodial extension for the tip cells [44]. Additionally the knockdown of filopodia causes cells to fail chemoattractant detection and diminishes organized transport and signal activation transmission [73, 92]. The upregulation of filopodia-producing proteins can lead to an increase in migratory and invasive behavior in cancer cells [60, 161]. For example higher levels in fascin expression, and therefore potentially increased filopodial formation, is a good predictor of increased metastatic and invasive behavior for cancer cells [99].

While filopodia have been implicated as environmental probes, these cellular fingers perform a variety of biological functions. Intercellular adhesion and signalling is initiated and

mediated by proteins enriched in filopodia [63, 70]. Adherens junctions in epithelial are one such intercellular adhesion structure mediated by E-cadherin, a protein enriched at filopodial tips [158]. Filopodia allow epithelial cells to align with junction partners and close gaps between cells to form a tight junction [68]. Tentacle-like behavior of filopodia has also been demonstrated by macrophage cells during the binding and retraction of target molecules: the filopodia retract inwards towards the cell upon binding the macrophage's target [85]. Filopodia also have a vital role in building an actin network that can successfully support neuronal growth [138]. Filopodia extending from neuronal growth cones are one of the most studied filopodial formations [18, 95]. Neurite initiation is knocked down by Ena/VASP-null mutants, but mDia2 can rescue the neuritogenesis by restoring filopodia growth [36]. Filopodia and lamellipodia both work in concert with actomyosin activity to adhere growth cones to different surfaces and apply forces needed to pull elongating growth cones towards targets [47].

Lastly, there has been some evidence for other unique filopodial functions amongst specialized cells. One example is the transfer of melanin and melanosomes, organelles that produce melanin, and between skin cells [5, 133, 136]. Another specialized function is the adaptation of viruses to use filopodia to assist with viral infection and transfer. For example, retroviruses create a stablized bridge between infected and uninfected cells to form a synapse that allows the virus to move to the uninfected target cells [135]. Additionally some viruses can move from the filopodial tips to the center of the cell before infection by "surfing" along the filopodial surface and using the underlying actin and myosin network to localize the virus to the central part of the cell [89]. The prevalence of filopodia across numerous cell functions demonstrate how filopodia are involved in impotant cellular functions and the formation of tissues in higher organisms. However the myosin-10 motor is important in the organization and localization of the filopodia-associated proteins and promotes the formation of filopodia in cells.

1.2 Myosin-10 and filopodial localization

1.2.1 Myosin-10 concentrates at filopodial tips

Myosin-10 is a group of motors in the myosin superfamily that localizes to the tips of filopodia in most organisms by walking along the actin network contained in filopodia. Originally discovered in the inner ear, myosin-10 is expressed in most cells at significantly lower levels than other myosin superfamily members. For example myosin-10 comprises only 0.0005% of total protein content in kidney tissue, one of the tissues previously determined to have the highest level of myosin-10 mRNA expression [14]. Numerous *in vivo* myosin-10 studies demonstrate that myosin-10 localizes to high concentrations in the filopodial tips [76, 140]. Lower concentrations of myosin-10 are also measured in the lamellipodia, invadopodia, and membrane ruffles [14]. Myosin-10 is recruited to the leading edge of the cell and is involved in multiple rounds of filopodial extention and retraction cycles [165]. Myosin-10 motors undergo long-distance motility through the filopodia, likely using their barbed-end directionality to travel away from the lamellipodium [77]. Once at the end of the actin track within the filopodia, myosin-10's journey finishes and the motors and cargo concentrate at the tips of the filopodia [76, 150].

1.2.2 Myosin-10 cargoes are concentrated in filopodia and filopodial tips

Many myosin-10 cargoes are proteins involved in the polymerization of actin bundles in filopodia, such as Ena/VASP and formins [65, 150, 165] The delivery of cargo to the cell periphery and tips of growing filopodia promotes addition filopodial formation and extension [129, 150]. Overexpressing full-length myosin-10 induces the formation of numerous filopodia [176]. However, motor head functionality is critical for the initiation of filopodia. Shortened myosin-10 constructs containing the motor and an FKBP were created to allow chemically inducible dimerization. Once rapamycin derivatives were added, filopodia formed in living cells. However when the same experiment was performed using mutations known to produce

inactive motors, filopodia formation did not occur with the rapamycin derivatives [151].

The best characterized myosin-10 cargo interaction is with netrin receptor DCC (deleted in colorectal cancer) [167]. Myosin-10 was determined to colocalize with DCC in young and differentiating neurons and was determined to be necessary for proper DCC localization in neurites [179]. Two crystal structures of the MyTH4FERM tandem, the minimal cargo binding domain, and a shortened DCC peptide demonstrated that an alpha helix derived from DCC preferentially binds the FERM portion of the MyTH4-FERM tandem [62, 167]. DCC has been suggested to bind and localize ribosomes to provide local protein translation at the neuron growth code and potentially bind secondary cargoes [62, 148]. This insight into myosin-10 DCC binding specificity and the proposed additional secondary functions of DCC provide exciting new possibilities for myosin-10 and its cargoes in filopodial functions.

Additional cargo proteins include integrins, as demonstrated by the colocalization and RNA interference studies of myosin-10 and β-integrins [176]. Knockdown of myosin-10 diminishes the localization of VE-cadherin and N-cadherin proteins to the filopodia, with proetins concentrating in the golgi bodies and center of the cell [3, 87]. Both integrins and cadherin proteins have been implicated in surface and intercellular adhesion, so myosin-10's role in the appropriate localization of these two protein families demonstrates the vital role myosin-10 can play in cell migration and tissue development [52]. Lastly, microtubule orientation during meiotic spindle assembly has been associated with myosin-10 [153, 171]. While this would link the actin and microtubule cytoskeleton, only one example of direct binding to microtubules by myosin-10 has been demonstrated so far [62, 166]. There are still many more studies that could be performed on myosin-10 and cargo interactions, but the current literature strongly demonstrates the vital role cargo-motor interactions play in cellular functions associated with myosin-10.

Another variant of myosin-10 that does not contain the motor domains and is known as the "headless" myosin-10 has been tested with filopodial formation [139]. RNAi-mediated knockdown of wild-type myosin-10 led to a decrease in axon outgrowth, while the knock-

down of the headless domain with endogenous full-length myosin-10 still expressing led to an increase in axon outgrowth. Quantifying the different numbers of filopodia produced by cells overexpressing either the headless or full-length myosin-10 constructs showed that the headless construct likely interferes with the filopodial extension [121]. Migration of chemomigratory cells overexpressing the headless construct migrated shorter distances than control cells, demonstrating a potential role for headless myosin-10 to control cellular migration [164]. These experiments predicted that that the headless domains likely competes for the same filopodia-building cargo. The headless variant demonstrates that myosin-10 plays a central role in filopodia formation and is sensitive to the presence of cargo in the promotion of filopodial growth.

1.2.3 General schemes of motion for myosin-10 within filopodia

Myosin-10 favorable moves towards the barbed-ends of actin, so the directed motility towards filopodial tips is not surprising since filopodia contain the barbed ends of actin in this region [65]. This theory is supported by the localization of myosin-10 with its various cargoes in cells. However, the drawback of many of the overexpression assays with myosin-10 is that measurable myosin-10 spots likely move as puncta of clustered motors. This prediction was confirmed by *in vivo* TIRF microscopy experiments monitoring myosin-10 motion in HeLa filopodia, which measured three different myosin-10 motions (Figure 1.2). The first movement is the slow motion of bright myosin-10 cluster with a velocity of approximately 80 nm/s, which was previously seen in many cellular assays. The second motion, which was also previously reported, is the rearward movement of the bright myosion-10 puncta at 10-20 nm/s. This matches the speed of retrograde actin flow back into the center of the cell. The novel myosin-10 motility measured in this study were faint and moved at high speeds between 340-780 nm/s [77]. The discovery of a new myosin-10 motility behavior demonstrated the need to better understand the motor by performing single molecule *in vitro* studies

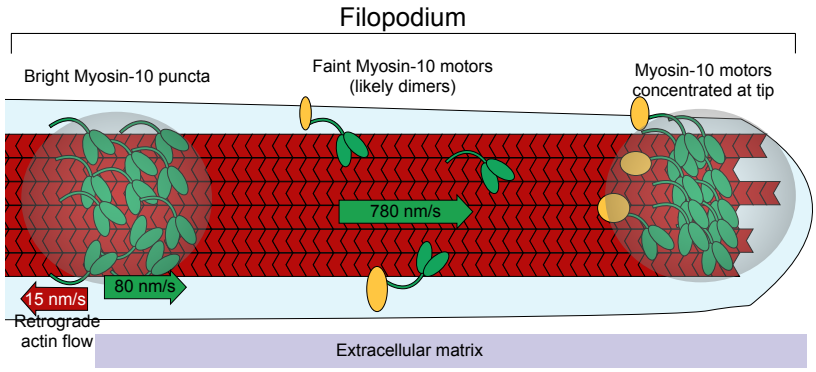

Figure 1.2: Myosin-10 has three forms of cellular intrafilopodial movement on actin bundles. Demonstrative diagram of three different motility behaviors of myosin-10 are resolvable by TIRF micrscopy. Myosin-10 move as a bright group towards the tip of the filopodia through the myosin-10 activity at 80 nm/s. Myosin-10 can also move as a group from the filopodia back to the more central lamellipodia at a speed of 10-20 nm/s, likely as a result of the retrograde actin flow of dead or inactive motor. In the same experimental setup, faint myosin-10 particles were seen moving at higher speeds of 400-800 nm/s as dimers to the filopodial tips. Adapted from Kerber and Cheney [76], 2011.

1.3 Myosin-10 features and structures

1.3.1 Full-length myosin-10 contains motor feet, legs, and cargo-binding domains

Full length myosin-10 has a molecular weight of approximately 240 kDa, per monomer. This motor protein contains three groups of domains: the motor foot, the leg domains, and the regulatory tail domains [76] (Figure 1.3). The motor domain binds to actin filaments and hydrolyzes ATP to produce movement [14] and has a high duty-ratio, allowing the motor to walk processively along actin filaments [66]. This means that each motor foot stays bound to actin more than 50% of the time, so that the collective dimeric motor has at lease one foot bound to the track at all times. Myosin motors need to have at least one foot bound to the actin during a successful processive motility event, so the high duty-ratio is vital for myosin-10's ability to move in filopodia [33, 76].

The next cluster of domains is known as the leg domains, which include the IQ, Single-Alpha-Helix, and coiled-coil domains. The IQ motif is a 20-24 amino acid long calmodulin

binding motif that receives its name from the conserved sequence motif in each core of the domain [24]. Myosin-10 has three IQ domains per monomer, with each IQ domain binding one calmodulin. The binding of calmodulin and calmodulin-like proteins enhances myosin-10 motor activity, demonstrating that myosin-10 motility could potentially be regulated by the expression of calmodulin in cells [12, 13].

Following the IQ domain are the single-alpha helix (SAH) domain and the coiled-coil domains, which are both comprised of alpha-helices favoring motifs [115]. The SAH domain forms an alpha-helical region that does not dimerize [6], while the coiled-coil domain forms a stable dimer [96]. Coiled-coils are often formed from a sequence heptad repeat, where there is a repeating pattern of hydrophobic and hydrophillic residues [25]. SAH domains have a similar heptad repeat to this coiled-coil domain, but the hydrophobic residues present in coiled coils are replaced by polar residues. The presence of a tandem comprised of SAH and coiled-coil domains in myosin-10 made it unique amongst commonly studied unconventional myosins [115]. These two features were the subject of research and discussion in myosin-10 circles, and the coiled-coil is discussed in further detail in Section 1.4 and Chapter 2. The SAH domain is described in more detail in Chapter 3.

Bridging the leg domains and the cargo domains is an approximately 150 residue region known as the PEST domain. This region is enriched in proline, glutamine, serine, and threonine, and this region has increased susceptibility to calpain cleavage [14]. Not much additional information is currently known about the PEST domain. Three pleckstrin homology (PH) domains form the first part of the tail domains. The PH domains are thought to interact with the lipid PIP_3 to help localize myosin-10 to the lamellipodium [156]. The MyTH4-FERM tandem domain is the C-terminal myosin-10 domain that binds myosin-10's protein cargo, many of which localize to filopodia [62, 167]. Currently, the PH and MyTH4-FERM domains are thought to be involved in the regulation and activation of myosin-10 motors, and may even play a part in regulating the dimerization of myosin-10 [156].

Based on sequencing information, myosin-10 has the closest homology with myosin-7.

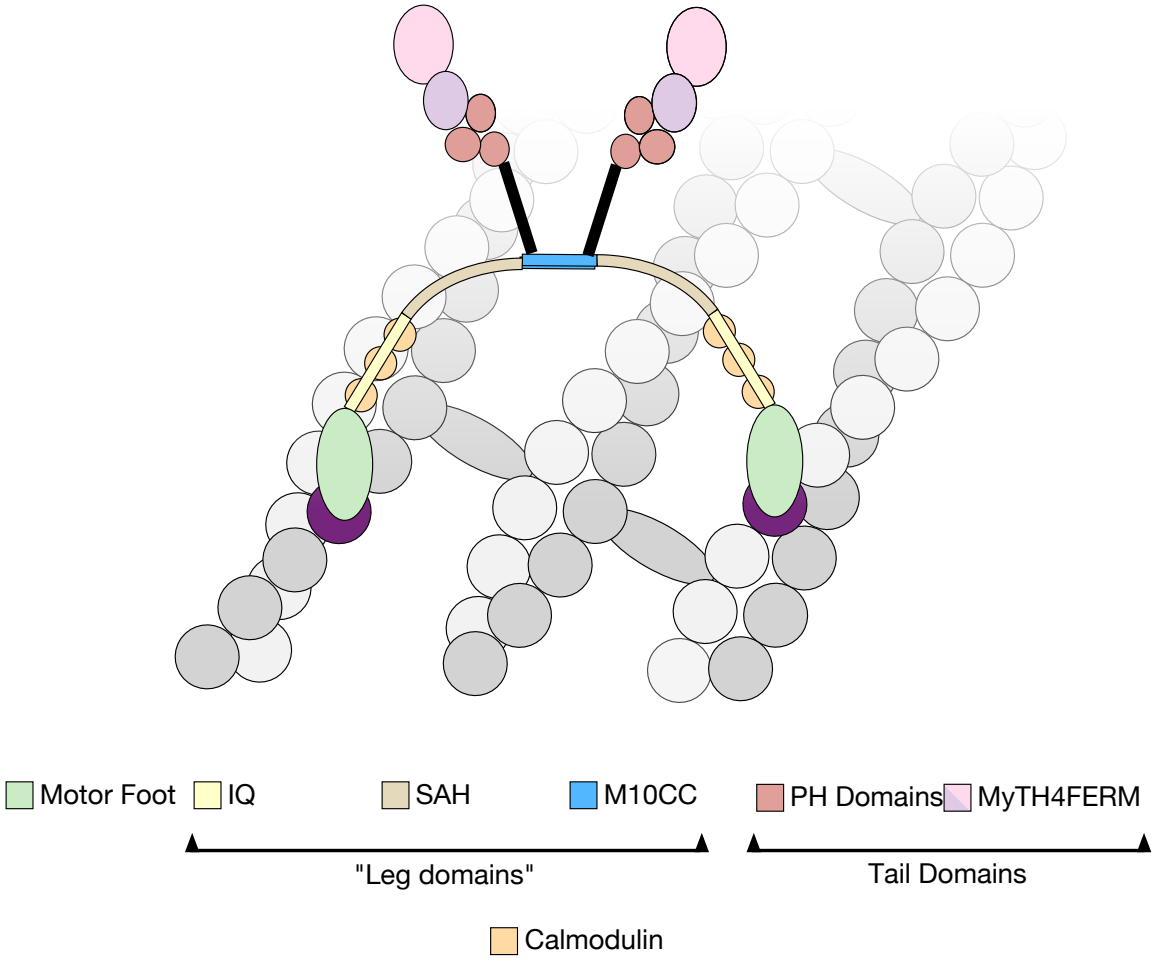

Figure 1.3: Diagram of myosin-10 domains on actin track. Myosin-10, illustrated as a dimer, walks on bundled actin (grey) towards the barbed end (faded region, towards top right). The motor feet domains (green) bind to specific monomers on separate actin filaments (purple) to walk processively along the actin track. The leg domains are composed of the IQ (yellow), SAH (tan) and coiled-coil domains. There are three IQ domains in myosin 10 that bind one calmodulin (orange circle) each. Tail domains comprise of three PH domains (red) and one MyTH4FERM tandem domain per monomer (MyTH4, purple; FERM, pink). Leg and tail domains are connected by a PEST domain (black line), which is a stretch of amino acids that have an unknown function.

The motor domains share a 45% sequence identity, and the MyTH4 domain show a sequence conservation of 20-40% between the myosin-4, myosin-7, myosin-10, and myosin-XV motors [23, 91]. The FERM domains usually have a 20-50% homology between protein families, and FERM domains have been identified in myosin-10, myosin-7, myosin-4, myosin-XV and talin, a component in focal adhesions [14, 76]. The largest differences between myosin-10's tail domains and those of other unconventional myosin motors is the number of insertions of proteins in the tail [14, 23, 91]. For example, myosin-XVa has two MyTH4 and two FERM domains, neither of which form tandem domains [17]. The unique combination of domains in myosin-10 demonstrate the need to understand how this motor moves in cells and the motor activation process.

1.4 *In vitro* characterization of myosin-10

Testing myosin motility *in vitro* provides a rich amount of information related to the motor's mechanical properties. One of the most commonly used methods is the gliding (or sliding) filament assay, where actin is passed over myosin motors affixed to glass coverslips. This assay provides information about the behavior of myosin domains, roles of mutations, and the velocities that a series of myosin motors can move an actin filament [94]. Total internal reflection fluorescent (TIRF) microscopy allows for this assay to be "flipped over" so the actin track is affixed to the glass slide and the myosin passes over the actin. These assays, known as single molecule assays, allow for the experimenter to measure different motility behaviors of individual molecules. This also allows for the control of ion conditions, cargo activation, and actin track control [149]. Optical tweezers can be added to the setup to measure very small displacement and to apply piconewton forces, mimicking resistance motors may experience in the cell [10].

1.4.1 Constructs used to characterize myosin-10 behavior

A combination of these techniques was used to determine how myosin-10 migrates through the cell and localizes to filopodia. However initial studies on the myosin-10 SAH and coiled-coil suggested that myosin-10 did not readily form dimers in the absence of cargoes [82]. Heavy meromysin (HMM) constructs, containing the foot and leg domains with an additional coiled-coil domain attached to force motor dimerization, were created to measure myosin-10 *in vitro*, similar to what was previously performed for myosin-6 [30]. Three constructs were created to test out the motility of myosin-10, and were derived from *Bos taurus* myosin-10 DNA. All constructs contain the same motor domain (742 amino acids, aa), IQ domains (21 aa, 19 aa, and 21 aa for IQ1, IQ2, and IQ3, respectively), and SAH domain (69 residues) (Figure 1.4).

The first construct, $M10^{short}$-GCN4 contains myosin-10 coiled-coil (M10CC) residues 883-920 and GCN4-p1 residues 4-32 [108]. Another construct using GCN4 as a dimerization domain, $M10^{long}$-GCN4, contains M10CC residues 883-936 and the entirety of the GCN4-p1 sequence [146]. $M10^{long+3}$-M5CC, the third construct, uses M10CC residues 883-939 and the myosin-5 coiled-coil (M5CC) as the nucleation domain [143]. Note that there are an extra three M10CC residues in $M10^{long+3}$-M5CC, which is sometimes referred to as $M10^{long}$-M5CC, compared to $M10^{long}$-GCN4. GCN4-p1 and M5CC were chosen to be the dimerization or nucleation domains for these constructs due to the high affinity of either coiled-coil domain [81, 157] and the previous use of GCN4 leucine zipper used before [155].

1.4.2 Motility behaviors of different constructs

Single molecule studies were performed on each of the three constructs demonstrated different motility patterns [108, 109, 123, 143, 151]. $M10^{short}$-GCN4 has a processive walk of 170 nm on single actin filaments, compared to a 630 nm processive walk on actin-fascin bundles. Additionally at identical motor and actin concentrations, $M10^{short}$-GCN4 initiated processive walks four times more often on bundled actin than filamentous actin [108].

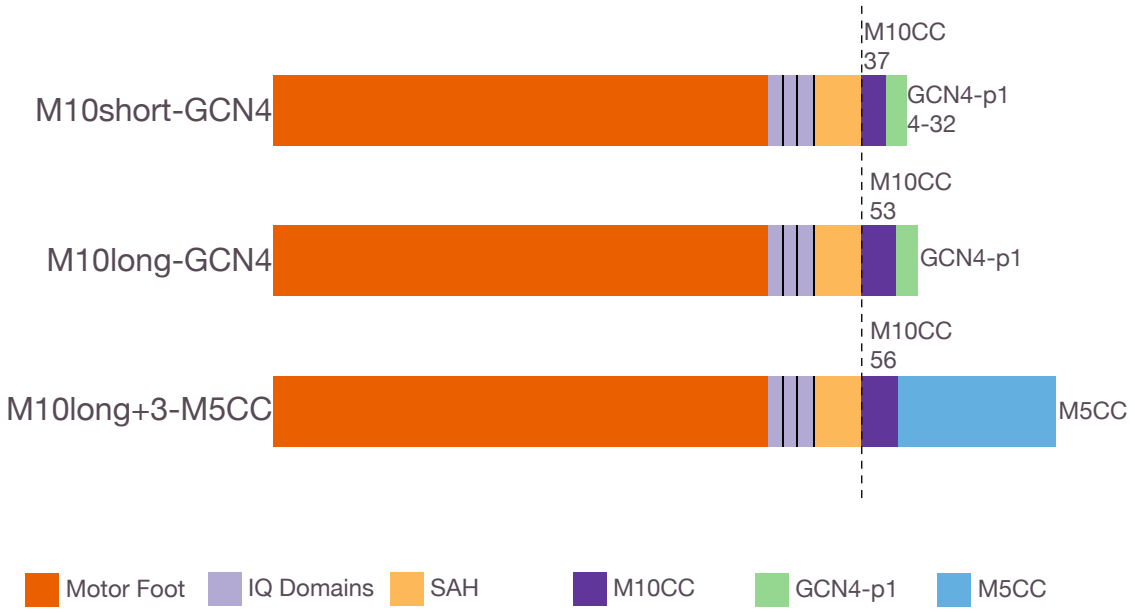

Figure 1.4: Multiple Constructs Were Used to Study Myosin-10 *In Vitro* Construct map for myosin-10 HMM constructs used to study the mechanical properties of myosin-10. All three constructs have the same motor domain (dark orange), IQ domains (light purple), and SAH domains (light orange). The differences between the constructs are in the number of residues in the myosin-10 coiled-coil (M10CC, dark purple) and the assisting dimerization domain. There are 3-4 amino acids between each IQ domain, which are indicated by black lines. GCN4-p1 (green) and myosin-5 coiled-coil (M5CC, blue) are two known parallel coiled-coil domains that dimerize at low concentrations. The number of residues from myosin-10's coiled-coil domain is listed above each M10CC domain. Since all three constructs are the same from residues 1–883, a dashed line has been drawn at the SAH-Coiled-coil boundary to show the similarities to the left of the line and the differences to the right of the line. Purification and labelling tags, e.g. GFP, are omitted from this figure but are available for reference in Figure 2.1.

M10^{long+3}-M5CC was also tested for processivity on single actin filaments and actin-fascin bundles. This construct did not demonstrate any selective behavior for actin-fascin bundles over single actin filaments, with 950 nm walks on filaments and 1160 nm walks on actin-fascin bundles. M10^{long}-GCN4 was tested using optical tweezers to measure the processivity of the construct under load, and the motor initiated a processive walk along single actin filaments [146]. Due to the specific experimental setup, only a few steps could be measured, but a previous study measured longer processive walks of this construct in a traditional single-molecule assay [9].

A majority of M10^{long+3}-M5CC motors walk along suspended single-actin filaments by spiraling around the actin filament. However, only a small proportion of these motors spiraled around actin-fascin bundles. This behavior could support the long run-lengths for M10^{long+3}-M5CC compared to M10^{long}-GCN4. Tied with a slower motor velocity on bundled actin, the authors concluded that myosin-10 motors can side-step and change the filaments they are walking on in a bundle. The findings from this study contrast with the conclusions from studies performed on M10^{short}-GCN4, which measured the x- and y-displacement of motors along an actin-fascin bundle. While other unconventional motors showed a rotational bias during a processive run, M10^{short}-GCN4 did not. M10^{short}-GCN4 initiated a motility on the bundle and continued walking straight with very few sidesteps for the majority of its recorded processive runs. While the motor could change filaments with a bundle, sidesteps from the motor were attributed mostly to adjustments of the motor path to roadblocks on the actin track. As a control, the x- and y-displacement of myosin-5 motor was tested and noted to walk without spiraling on a single-actin filament, likely because the step-size of myosin-5 roughly matches the actin pseudohelical pitch [123].

Experiments on M10^{long}-GCN4 attempted to measure the force generation of myosin-10, and by lowering the trap stiffness, were able to collect information on short processive walks. With this information, the authors were able to measure forward and backward single steps of approximately 35 nm [146]. These are pretty similar step sizes that were collected

using M10^{long+3}-M5CC of 34 nm [143]. However these two step sizes are significantly larger than the step size of M10^{short}-GCN4. M10^{short}-GCN4 has a stepsize of 17-18 nm on actin bundles and a stepsize of 16 nm on single actin filaments [109, 123]. Based on the step sizes and behavior of the different constructs, two models of myosin-10 motility were proposed. The first is a hand-over-hand model, predicted from the behavior of M10^{long+3}-M5CC and M10^{long}-GCN4, is similar to the motion of myosin-5. In this model the motors walk very similar to a tight-rope walker and can easily move along actin filaments.

M10^{short}-GCN4's behavior led to the proposal of the straddle model, which predicts that each head in a myosin-10 dimer will bind and unbind the same actin filament in a bundle. However, the requirement for an actin bundle to initiate motility arises from the fact that the motor heads cannot bind the same filament and will in fact straddle between the two filaments in the bundle (Figure 1.5). This model was mainly derived from studying the source of M10^{short}-GCN4's bundle selection. Chimera constructs of M10^{short}-GCN4 were created by swapping one or more of the following from myosin-5: motor heads, IQ domains (of which myosin-5 has six compared to myosin-10's three), and the SAH-Coiled-coil domain. This study showed that constructs containing the SAH-coiled-coil domain derived from M10CC^{short}-GCN4 maintained their bundle selectivity, while all other constructs either did not demonstrate selectivity or did not produce any events, which occurred when the myosin-10 IQ domains were attached to the myosin-5 coiled-coil. Importantly, swapping the myosin-10 IQ domains with the longer set of myosin-5 IQ domains did not change the selective behavior of the constructs, indicative that spacing of the motor heads is not as important as the effect of the myosin-10 SAH + M10^{short}-GCN4's coiled-coil [109].

Lastly, differences in construct behavior were initially predicted to result from different myosin-10 coiled-coil truncation points in the three construct designs. The same study using the myosin-5 and myosin-10 chimeras attempted to reduce bundle selectivity of M10^{short}-GCN4 using only myosin-10 domains. The researchers added a six residue -GSGGSG- flexible linker region either before the SAH domain at residue 819 or after the SAH domain at residue

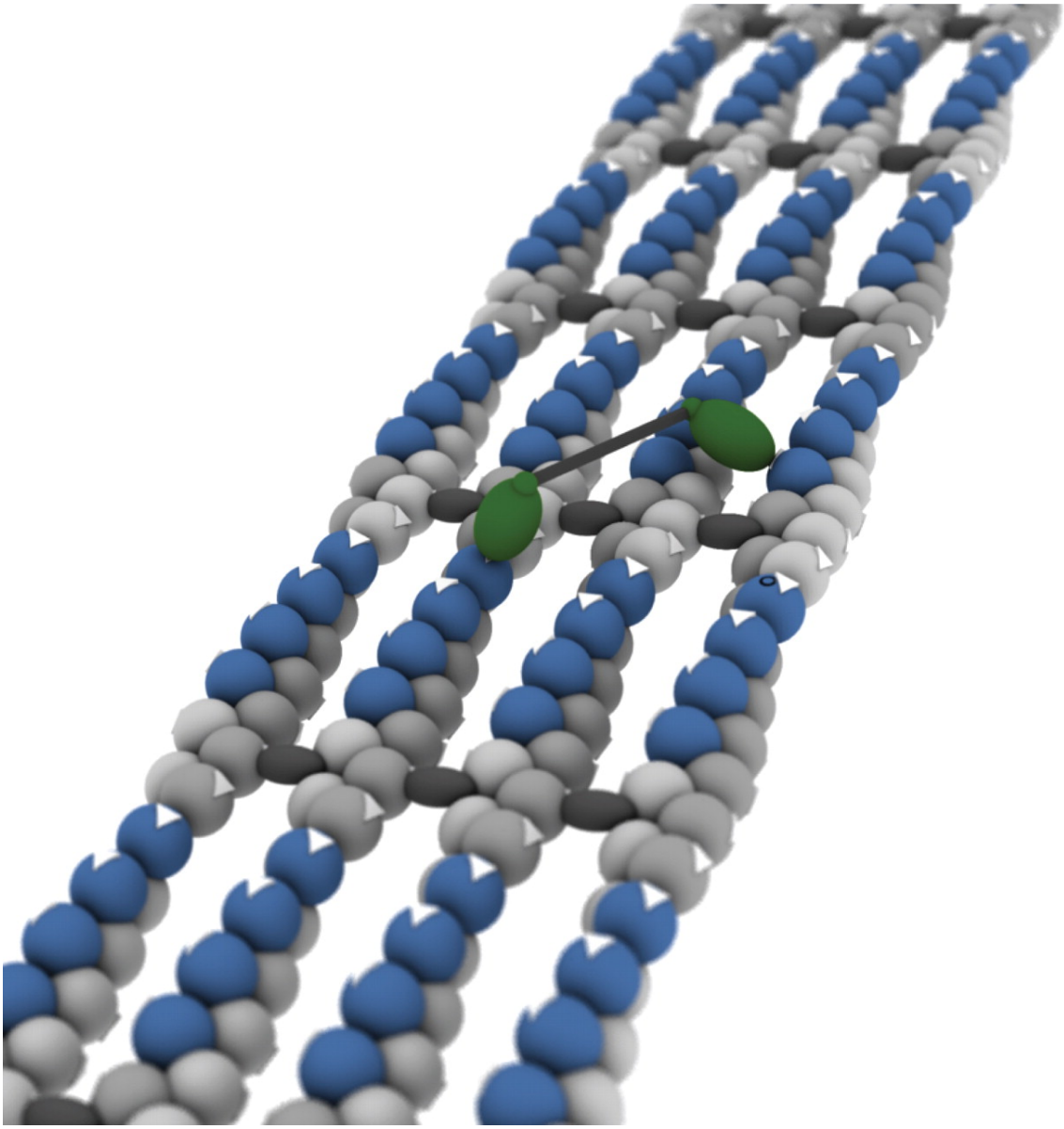

Figure 1.5: Model of myosin-10 walkin along bundled actin imagined by straddle model. Myosin-10 (green motor feet connected by simplified black connection) walking along a four-filament bundle shows how a dimerized motor walks along separate actin filaments within a bundle. In this model, the motor is predicted to straddle over a middle actin filament and bind the two surrounding filaments in alternating steps. The blue actin monomers in this diagram are actin monomers predicted to be available for the myosin to bind, with the grey monomers being sterically blocked and unavailable for binding. Changing filaments within the bundle is possible but unfavorable because the stepsize would have to change from the 18 nm average to increase or decrease based on which filament the motor is changing too. Reprinted from Nagy and Rock, J. Biol. Chem. (2010)**285**, 26608-26617 [109].

position 862 to create two different constructs, known as "swivel" constructs. Both swivel constructs demonstrated disrupted bundled actin selectivity, with longer walks on actin filaments but shorter walks on bundled actin compared to $M10^{short}$-GCN4 [109]. These experiments demonstrated that there was an additional unknown property of myosin-10 causing differing degrees of bundle selectivity to occur between the artificial constructs.

1.4.3 Myosin-10's unique coiled-coil domain

The controversy around myosin-10's predicted motility and the different motility behaviors between the constructs would not be resolved until more information was known about the coiled-coil. A fourth group set out to perform sedementation ultracentrifugation and NMR structural studies on myosin-10's coiled-coil and the neighboring domains in an attempt better understand the differences observed by previous groups. The dimerization affinity of myosin-10's coiled-coil has a K_D of 590 nM, which is a much weaker affinity than what is needed for single molecule studies [96]. This discovery of the lower affinity explains why shortened myosin-10 constructs could be active in the gliding filament assay but would be unable to dimerize for single-molecule motility studies without an additional dimerization domain.

This study also solved the NMR solution structure for the wild-type *Homo sapiens* myosin-10 coiled-coil and revealed a surprising anti-parallel orientation for this coiled-coil (Figure 1.6). Each monomer is composed of two alpha-helices, αA and αB, with the break of these two α-helices occurring between residues 910-914. The αA helices also provide a hydrophobic seam between the two monomers and form the core body of the anti-parallel coiled-coil. The αB helices bend back over the N-termus of opposite monomers' αA helix [96], potentially providing the ability to bury an out-of-frame hydrophobic residue.

Previous HMM constructs were designed under the assumption that myosin-10's coiled-coil was parallel oriented, much like the myosin-5's and myosin-6's coiled-coil. Based on this assumption about the coiled-coil orientation, GCN4 and myosin-5's coiled-coil were selected

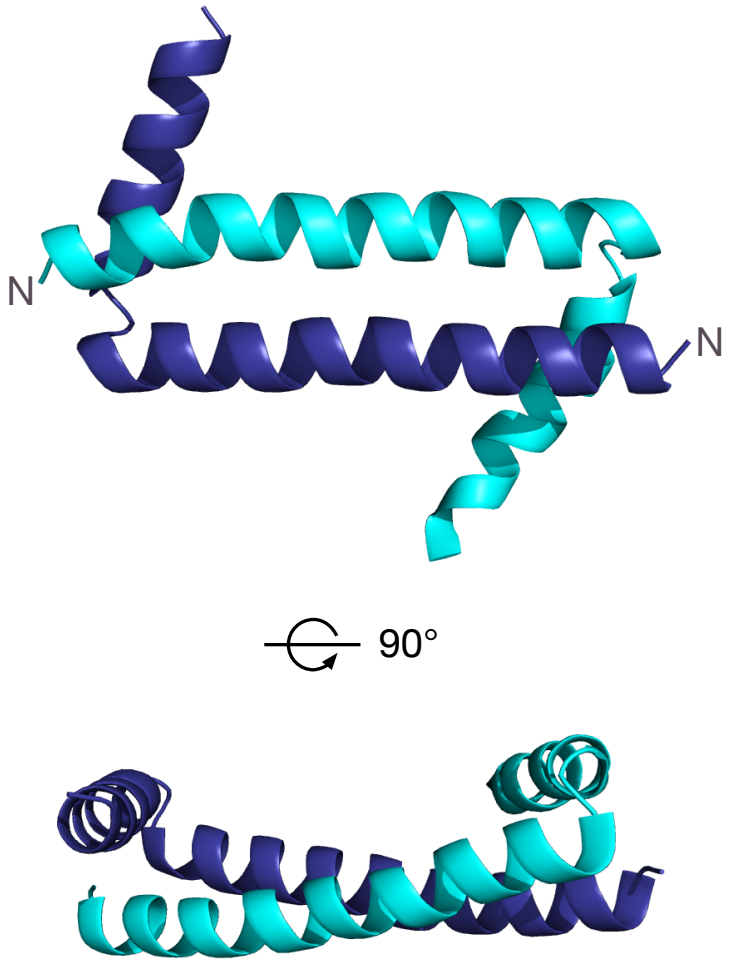

Figure 1.6: Wild-type myosin-10 coiled-coil is anti-parallel NMR solution structure of *Homo sapiens* wild-type myosin-10 coiled-coil from [96]. This structure is shown from two different perspectives with a 90 rotation occurring between the upper and lower panels. The anti-parallel orientation forces the motor feet to point in opposite directions of each other, potentially causing bundle selectivity for active motor. This coiled-coil is formed by two helices per monomer: α-A is the larger helix that starts at the N-terminus (marked by "N" if the upper panel). At residue 910, a bend occurs that leads to the formation of the second helix, α-B, which covers the opposite monomer's N-termal residues. Structures generated in Pymol from PDB entry 2LW9.

as two good choices for these studies [108, 143, 146]. However the anti-parallel coiled-coil structure was novel to the myosin superfamily, and maybe the source of myosin-10's ability to locate and localize to filopodial tips [96]. This anti-parallel orientation likely explains the differences seen between the *in vitro* behaviors of M10$^{\text{short}}$-GCN4, M10$^{\text{long+3}}$-M5CC, and M10$^{\text{long}}$-GCN4, since all three of these designs attach a parallel coiled-coil to the end of the anti-parallel coiled-coil. The potential for additional flexibility is higher in the two constructs, M10$^{\text{long}}$-GCN4 and M10$^{\text{long+3}}$-M5CC, since both have the parallel coiled-coil fused long after the bend at points at the C-terminal of the wild-type structure.

1.5 Research directions and questions addressed in thesis

1.5.1 Dimerization orientations of artificial myosin-10 construct coiled-coils

Prior to the publication of the wild-type myosin-10 coiled-coil, the source of bundle selectivity demonstrated by M10$^{\text{short}}$-GCN4 was unknown. Suspicion fell on the sudden truncation of the myosin-10 CC at residue 920, while the longer constructs contained the entirety of the coiled-coil. The publication of the myosin-10 coiled-coil structure demonstrated a potential for the structures of the various constructs dimerization domains to cause different motility behaviors, with one or more of the construct behaviors being the result of structure artifacts from fusing an anti-parallel and parallel coiled-coil together. Therefore structural comparisons between the coiled-coils of the three constructs with the wild-type structure were performed to better understand the link between the coiled-coil domains and their individual motility behaviors.

Due to the high solubility of each of the three coiled-coil constructs observed during preliminary studies, solution structural biology techniques were used for all three constructs. Due to the small size of GCN4, the coiled-coil domains of M10$^{\text{short}}$-GCN4 and M10$^{\text{long}}$-GCN4 are small enough to have resolvable signal by NMR spectroscopy. In this thesis I

performed a brief HSQC to study the local environment of the amide backbone atoms in M10^{long}-GCN4. I also performed more NMR experiments allowing for the determination of the solution structure of the M10^{short}-GCN4 construct, which I demonstrate is in an antiparallel orientation. The larger size of myosin-5's coiled-coil required a different technique to attempt to obtain a structure for M10^{long+3}-M5CC's coiled-coil. Therefore, in this thesis I performed small-angle X-ray scattering (SAXS) of the coiled-coils on both M10^{long+3}-M5CC and M10^{short}-GCN4. Additional characterization of the constructs was performed by analyzing preparative size exclusion chromatography data and circular dichroism (CD) data. These experiments test and compare the orientations and stabilities of each coiled-coil to the wild-type with the aim of better understanding how M10^{short}-GCN4 remains bundle selective and whether any of the three coiled-coils mimic the anti-parallel orientation of wild-type coiled-coil.

1.5.2 Role of SAH domains in influencing myosin-10 behavior

Previous studies on the SAH domain itself provided insight into how SAH domains can form and differ from coiled-coils, but previous experiments studying the myosin-10 SAH domain did not include the entire domain or provide concrete details about this unique domain and the role it plays in myosin motility [82, 114]. Bundle selectivity of myosin-10/myosin-5 chimeras and the diminished bundle selectivity of M10^{short}-GCN4 when flexible linker regions were introduced before or after the defined SAH both demonstrate the importance of a structured SAH domain in myosin-10 motility [108]. During the NMR structural studies of the wild-type myosin-10 coiled-coil, a comparative HSQC experiment was performed including half of the SAH domain with the wild-type coiled-coil (residues 856-934 for the SAH-coiled-coil, compared with residues 883-934 for the wild-type coiled-coil). These HSQC experiments demonstrated that the presence of this portion of the SAH domain does not significantly change the chemical environment for atoms in the coiled-coil residues, indicating that the presence of the SAH domain does not significantly alter the structure of the

coiled-coil. Peaks associated with the SAH were not assigned, since the authors were testing the stability of the coiled-coil and not enough peaks correlating to the entire SAH domain were resolved [96]. These experiments provide enough valuable information to conclude that even though there is an amount of stability after the SAH domain to point the myosin-10 motor feet in opposite directions. However there there is some flexibility in the SAH domain that likely prevents the HSQC assignment of SAH peaks.

Measuring the stability and flexibility of the full SAH domain and the combination of the SAH-coiled-coil domains will provide more insight into how myosin-10 feet are oriented to walk along actin tracks. SAXS was performed on *Homo sapiens* and *Bos taurus* myosin-10 SAH domains and on SAH-CC tandems derived from $M10^{short}$-GCN4 and *Homo sapiens* myosin-10. To provide a better idea of the secondary stucture and stabilization of these constructs, CD experiments were performed. While this work is currently ongoing, the main goal is to determine the degree of flexibility in the SAH domain and the stability of the SAH-coiled-coil interface. This work, tied together with the determination of the artificial construct coiled-coil stabilities, will provide a better understanding of how the myosin-10 SAH and coiled-coil domains influence the behavior of myosin-10's processive motility. This work also aims to tie the motility and bundle selectivity behaviors of the artificial constructs to the wild-type motor to better predict how myosin-10 can select its tracks once activates.

CHAPTER 2

STRUCTURAL COMPETITION BETWEEN COILED-COILS CLARIFIES ACTIN BUNDLE SELECTION IN MYOSIN-10

The work described in this chapter is available as a journal publication with the following citation:

Vavra, K.C., Xia, Y., Rock, R. S. Competition between Coiled-Coil Structures and the Impact on Myosin-10 Bundle Selection. *Biophys. J,* 110(11): 2517-2527, Jun 2016.

This chapter is reprinted with permission from Elsevier under license number 3900101163599.

2.1 Summary

Coiled-coil fusions are a useful approach to enforce dimerization in protein engineering. However, the final structures of coiled-coil fusion proteins have received relatively little attention. Here, we determine the structural outcome of adjacent parallel and antiparallel coiled coils. The targets are coiled coils that stabilize myosin-10 in single-molecule biophysical studies. We reveal the solution structure of a short, antiparallel, myosin-10 coiled coil fused to the parallel GCN4-p1 coiled coil. Surprisingly, this structure is a continuous, antiparallel coiled coil where GCN4-p1 pairs with myosin-10 rather than itself. We also show that longer myosin-10 segments in these parallel/antiparallel fusions are dynamic and do not fold cooperatively. Our data resolve conflicting results on myosin-10 selection of actin filament bundles, demonstrating the importance of understanding coiled-coil orientation and stability.

2.2 Introduction

Myosin-10 transports several cell-surface receptors to filopodial tips in vertebrate cells [26, 76, 140]. These filopodia are actin-based protrusions at the plasma membrane with a central

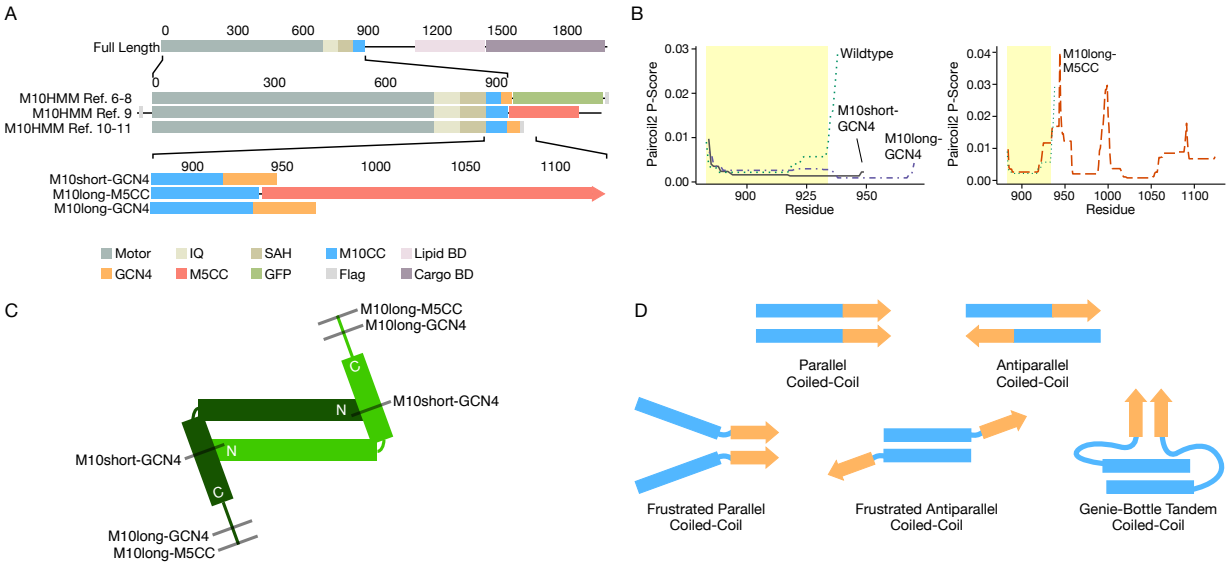

Figure 2.1: Prior myosin-10 work fused parallel and antiparallel coiled coils. (A) Construct map of full-length myosin-10 (top), the three full-length constructs used in prior single-molecule work (middle), and the three coiled-coil constructs used in this study (bottom; M5: myosin-5, M10: myosin-10, SAH: single -helix [82], BD: binding-domain). Note the differences in the length of the native myosin-10 coiled coil and the type of stabilizing *C*-terminal coiled coil (GCN4 vs. M10CC) between all three constructs.
(B) Paircoil2 [102] scores for the wildtype myosin-10 and the three coiled-coil constructs. P-scores below a threshold of 0.02 indicate a predicted coiled coil. The yellow zone indicates the defined bounds of the wildtype coiled coil. M10$^{\text{short}}$-GCN4 and M10$^{\text{long}}$-GCN4 have a continuous heptad repeat across the boundary, while M10$^{\text{long}}$-M5CC (right, note the larger residue range) has a break at the boundary.
(C) Illustration of the myosin-10 coiled-coil solution NMR structure determined by the Zhang group [96]. The *N*-terminal helices (αA) are antiparallel, while the *C*-terminal helices (αB) bend over the ends. The SAH domains [82], IQ domains, and motor domains extend from the *N*-terminal ends. Locations of the last myosin-10 coiled-coil residue for the M10$^{\text{short}}$-GCN4, M10$^{\text{long}}$-M5CC, and M10$^{\text{long}}$-GCN4 constructs are shown. The stabilizing coiled coils immediately follow the C-terminal end of each construct. Note that the myosin-10 portion of M10$^{\text{short}}$-GCN4 terminates early in the αB helix, while M10$^{\text{long}}$-M5CC and M10$^{\text{long}}$-GCN4 both include the entire B helix.
(D) Five proposed structural outcomes when a myosin-10 coiled coil (blue) is fused to a *C*-terminal GCN4-p1 / myosin-5 coiled coil (orange).

core of a fascin-actin bundle [16, 18]. In earlier work we defined a bundle selection mechanism for myosin-10 that explains how it navigates to filopodia and functions as an intrafilopodial transporter [76]. Specifically, myosin-10 is maximally processive when it straddles two filaments within the fascin-actin bundle, and walks poorly along single filaments [108, 109, 123]. This bundle selectivity is specific to myosin-10, as myosin-5 walks equally well along both bundles and single filaments [108].

However, the concept of myosin-10 as a bundle selective motor has been controversial. Two other groups [9, 143, 146] found that myosin-10 is a processive transporter on both single filaments and bundles. All three groups made truncated myosin-10 heavy meromyosin (HMM) fragments using different coiled-coil lengths and design patterns (Figure 2.1A, Figure 2.2). Specifically, all three designs include a *C*-terminal stabilizing coiled coil [155]. Two designs use GCN4-p1, a 34-amino acid leucine-zipper derived from the GCN4 yeast transcription activator [113]. The third design uses the myosin-5 coiled coil for stabilization. Such stabilization is required in low-concentration single-molecule studies. Because we identified the coiled coil as the critical element that governs bundle selection [109], here we investigate the structures of the three excised coiled coils (M10$^{\text{short}}$-GCN4, M10$^{\text{long}}$-GCN4, and M10$^{\text{long}}$-M5CC, Figure 2.1A, 2.1B, 2.3).

The myosin-10 coiled coil is of particular interest because an NMR structure shows that it is antiparallel with a *C*-terminal bend [96] (Figure 2.1C). This antiparallel orientation is currently unique in dimeric myosins. M10$^{\text{short}}$-GCN4, M10$^{\text{long}}$-M5CC, and M10$^{\text{long}}$-GCN4 HMM constructs all fuse their stabilizing coiled coil at the *C*-terminus of the myosin-10 coiled coil. However, all three designs had inadvertently fused a parallel coiled coil to an antiparallel coiled coil.

The final structure of fused parallel and antiparallel coiled coils is uncertain. The possibilities include: overall parallel, overall antiparallel, partially folded or frustrated states, or both parallel and antiparallel segments with intervening extended linkers (which we call the "genie bottle" configuration in reference to its shape; Figure 2.1D). Due to the incompati-

> Bt Myosin-10 Full Length
MDNFFPEGTRVWLRENGQHFPSTVNSCAEGVVVFQTDYGQVFTYKQSTITHQKVMPMQPTDEEGVDDMATLTELHGGAIM
HNLYQRYKRNQIYTYIGSIIASVNPYKTITGLYSRDAVDRYSRCHLGELPPHVFAIANECYRCLWKRHDNQCVLISGESG
AGKTESTKLILKFLSAISQQSVDLSSKEKTSSVEQAILESSPIMEAFGNAKTVYNNNSSRFGKFVQLNIGQKGNIQGGRI
VDYLLEKNRVVRQNPGERNYHIFYALLAGLGHEEREEFYLSVPENYHYLNQSGCVTDRTISDQESFREVIMAMEVMQFSK
EEVREVLRLLAGILHLGNIEFITAGGAQVSFKTALGRSAELLGLDPAQLTDALTQRSMFLRGEEILTPLNVQQAADSRDS
LAMALYARCFEWVIKKINSRIKGKDDFKSIGILDIFGFENFEVNHFEQFNINYANEKLQEYFNKHIFSLEQLEYSREGLV
WEDIDWIDNGECLDLIEKKLGLLALINEESHFPQATDSTLLEKLHNQHANNHFYVKPRVAVNNFGVKHYAGEVQYDVRGI
LEKNRDTFRDDLLNLLRESRFDFIYDLFEHVSSRNNQDTLKCGSKHRRPTVSSQFKDSLHSLMATLSASNPFFVRCIKPN
MQKMPDQFDQAVVVNQLRYSGMLETVRIRKAGYAVRRPFQDFYKRYKVLMRNVALPEDIRGKCTALLQLYDASNSEWQLG
KTKVFLRESLEQKLEKRQEEEVTRAAMVIRAHVLGYLARKQYKKVLDCVVIIQKNYRAFLLRRRFLHLKKAAVVFQKQLR
GQIARRVYRQLLAEKRAEEEKRKREEEEKRKREEEERERERRERAELRAQQEEAARKQRELEALQQESQRAAELSRELE
KQKENKQVEEILRLEKEIEDLQRMKERQELSLTEASLQKLQQLRDEELRRLEDEACRAAQEFLESLNFDEIDECVRNIER
SLSVGSGCTGEQGAGAEKPSFNFSQPYPEEEEVDEGFEADDDAFKDSPNPSEHGHSDQRTSGIRTSDESSEEDPYMNDTV
VPTSPSADSTVLLAPSEHDSSAGEPTYCLPQTPGALPAPEGDYDYDQDDYEDGAITSGSSVTFSNSCSSQWSPDYRCSVG
TYNSSGAYRFSSEGAQSSFEDSEEDFDSRFDTDDELSYRRDSVYSCVTLPYFHSFLYMKGGLMNSWKRRWCVLKDETFLW
FRSKQEALKQGWLHKKGGGSSTLSRRNWKKRWFVLRQAKLMYFENDSEEKLKGTVEVRAAKEIIDNTSKENGIDIIMADR
TFHLIAESPEDASQWFSVLSQVHASTDQEIREMHDEQANPQNAVGTLDVGLIDSVCASDSPDRPNSFVIITANRVLHCNA
DTPEEMHHWITLLQRSKGDTRVEGQEFIVRGWLHKEVKNSPKMSSLKLKKRWFVLTHNSLDYYKSSEKNALKLGTLVLNS
LCSVVPPDEKIFKETGYWNVTVYGRKHCYRLYTKLLNEATRWSSAIQNVTDTKAPIDTPTQQLIQDIKENCLNSDVVEQI
YKRNPILRHTHHPLHSPLLPLPYGDINLNLLKDKGYTTLQDEAIKIFNSLQQLESMSDPIPIIQGILQTGHDLRPLRDEL
YCQLIKQTNKVPHPGSVGNLCSWQILTCLSCTFLPSRGILKYLKFHLRRIREQFPGTEMEKYALFIYESLKKTKCREFVP
SRDEIEALIHRQEMTSTVHCHGGGSCKITVNSHTTAGEVVEKLIRGLAMEDSRNMFALFEYNGHVDKAIESRTIVADVLA
KFEKLAATSEVGEQPWKFYFKLYCFLDTDNVPKDSVEFAFMFEQAHEAVIHGHYPAPEENLQVLAALRLQYLQGDYAPHA
PVPPLEEVYSLQRLKARISQSTKSFTPGERLEKRRTSFLEGTLRRSFRTGSAIRQKAEEEQMVDMWVKEEVCSARASILD
KWKKFQGMSQEQAMAKYMALIKEWPGYGSTLFDVECKEGGFPQDLWLGVSADAVSVYKRGEGRPLEVFQYEHILSFGAPL
ANTYKIVVDERELLFETSEVVDVAKLMKAYISMIVKKRYSTSRSVSSQGSSR
> Myosin-10 HMM Construct with M10short-GCN4
MDNFFPEGTRVWLRENGQHFPSTVNSCAEGVVVFQTDYGQVFTYKQSTITHQKVMPMQPTDEEGVDDMATLTELHGGAIM
HNLYQRYKRNQIYTYTGSIIASVNPYKTITGLYSRDAVDRYSRCHLGELPPHVFAIANECYRCLWKRHDNQCVLISGESG
AGKTESTKLILKFLSAISQQSVDLSSKEKTSSVEQAILESSPIMEAFGNAKTVYNNNSSRFGKFVQLNIGQKGNIQGGRI
VDYLLEKNRVVRQNPGERNYHIFYALLAGLGHEEREEFYLSVPENYHYLNQSGCVTDRTISDQESFREVIMAMEVMQFSK
EEVREVLRLLAGILHLGNIEFITAGGAQVSFKTALGRSAELLGLDPAQLTDALTQRSMFLRGEEILTPLNVQQAADSRDS
LAMALYARCFEWVIKKINSRIKGKDDFKSIGILDIFGFENFEVNHFEQFNINYANEKLQEYFNKHIFSLEQLEYSREGLV
WEDIDWIDNGECLDLIEKKLGLLALINEESHFPQATDSTLLEKLHNQHANNHFYVKPRVAVNNFGVKHYAGEVQYDVRGI
LEKNRDTFRDDLLNLLRESRFDFIYDLFEHVSSRNNQDTLKCGSKHRRPTVSSQFKDSLHSLMATLSASNPFFVRCIKPN
MQKMPDQFDQAVVVNQLRYSGMLETVRIRKAGYAVRRPFQDFYKRYKVLMRNVALPEDIRGKCTALLQLYDASNSEWQLG
KTKVFLRESLEQKLEKRQEEEVTRAAMVIRAHVLGYLARKQYKKVLDCVVIIQKNYRAFLLRRRFLHLKKAAVVFQKQLR
GQIARRVYRQLLAEKRAEEEKRKREEEEKRKREEEERERERRERAELRAQQEEAARKQRELEALQQESQRAAELSRELE
KQKENKQVEEILRLEKEIEDLQRMKERQELSLTEASLQKLQQLEDKVEELLSKNYHLENEVARLKKLVGEMVSKGEELFTG
VVPILVELDGDVNGHKFSVSGEGEGDATYGKLTLKFICTTGKLPVPWPTLVTTLTYGVQCFSRYPDHMKQHDFFKSAMPE
GYVQERTIFFKDDGNYKTRAEVKFEGDTLVNRIELKGIDFKEDGNILGHKLEYNYNSHNVYIMADKQKNGIKVNFKIRHN
IEDGSVQLADHYQQNTPIGDGPVLLPDNHYLSTQSALSKDPNEKRDHMVLLEFVTAAGITLGMDELYKSGRTQISDYKDD
DDK
> Myosin-10 HMM Construct with M10long-M5CC
MSYYHHHHHHDYKDDDDKNIPTTENLYFQGAMGIRNSKAYVDMDNFFPEGTRVWLRENGQHFPSTVNSCAEGVVVFQTDY
GQVFTYKQSTITHQKVMPMQPTDEEGVDDMATLTELHGGAIMHNLYQRYKRNQIYTYIGSIIASVNPYKTITGLYSRDAV
DRYSRCHLGELPPHVFAIANECYRCLWKRHDNQCVLISGESGAGKTESTKLILKFLSAISQQSVDLSSKEKTSSVEQAIL
ESSPIMEAFGNAKTVYNNNSSRFGKFVQLNIGQKGNIQGGRIVDYLLEKNRVVRQNPGERNYHIFYALLAGLGHEEREEF
YLSVPENYHYLNQSGCVTDRTISDQESFREVIMAMEVMQFSKEEVREVLRLLAGILHLGNIEFITAGGAQVSFKTALGRS
AELLGLDPAQLTDALTQRSMFLRGEEILTPLNVQQAADSRDSLAMALYARCFEWVIKKINSRIKGKDDFKSIGILDIFGF
ENFEVNHFEQFNINYANEKLQEYFNKHIFSLEQLEYSREGLVWEDIDWIDNGECLDLIEKKLGLLALINEESHFPQATDS
TLLEKLHNQHANNHFYVKPRVAVNNFGVKHYAGEVQYDVRGILEKNRDTFRDDLLNLLRESRFDFIYDLFEHVSSRNNQD
TLKCGSKHRRPTVSSQFKDSLHSLMATLSASNPFFVRCIKPNMQKMPDQFDQAVVVNQLRYSGMLETVRIRKAGYAVRRP
FQDFYKRYKVLMRNVALPEDIRGKCTALLQLYDASNSEWQLGKTKVFLRESLEQKLEKRQEEEVTRAAMVIRAHVLGYLA
RKQYKKVLDCVVIIQKNYRAFLLRRRFLHLKKAAVVFQKQLRGQIARRVYRQLLAEKRAEEEKRKREEEEKRKREEEERE
RERERREAELRAQQEEAARKQRELEALQQESQRAAELSRELEKQKENKQVEEILRLEKEIEDLQRMKERQELSLTEASLQ
KLQQLRDEELRRLEDEACRAAKLLKIEARSVERYKKLHIGMENKIMQLQRKVDEQNKDYKCLMEKLTNLEGVYNSETEKL
RNDVERLQLSEEEAKVATGRVLSLQEEIAKLRKDLEQTRSEKKSIEERADKYKQETDQLVSNLKEENTLLKQEKETLNHR
IVEQAKEMTETMERKLVEETKQLELDLNDERLRYQNLLNEFSRLEEHMGGGLNDIFEAQKIEWHE
> Myosin-10 HMM Construct with M10long-GCN4
MDNFFPEGTRVWLRENGQHFPSTVNSCAEGVVVFQTDYGQVFTYKQSTITHQKVMPMQPTDEEGVDDMATLTELHGGAIM
HNLYQRYKRNQIYTYIGSIIASVNPYKTITGLYSRDAVDRYSRCHLGELPPHVFAIANECYRCLWKRHDNQCVLISGESG
AGKTESTKLILKFLSAISQQSVDLSSKEKTSSVEQAILESSPIMEAFGNAKTVYNNNSSRFGKFVQLNIGQKGNIQGGRI
VDYLLEKNRVVRQNPGERNYHIFYALLAGLGHEEREEFYLSVPENYHYLNQSGCVTDRTISDQESFREVIMAMEVMQFSK
EEVREVLRLLAGILHLGNIEFITAGGAQVSFKTALGRSAELLGLDPAQLTDALTQRSMFLRGEEILTPLNVQQAADSRDS
LAMALYARCFEWVIKKINSRIKGKDDFKSIGILDIFGFENFEVNHFEQFNINYANEKLQEYFNKHIFSLEQLEYSREGLV
WEDIDWIDNGECLDLIEKKLGLLALINEESHFPQATDSTLLEKLHNQHANNHFYVKPRVAVNNFGVKHYAGEVQYDVRGI
LEKNRDTFRDDLLNLLRESRFDFIYDLFEHVSSRNNQDTLKCGSKHRRPTVSSQFKDSLHSLMATLSASNPFFVRCIKPN
MQKMPDQFDQAVVVNQLRYSGMLETVRIRKAGYAVRRPFQDFYKRYKVLMRNVALPEDIRGKCTALLQLYDASNSEWQLG
KTKVFLRESLEQKLEKRQEEEVTRAAMVIRAHVLGYLARKQYKKVLDCVVIIQKNYRAFLLRRRFLHLKKAAVVFQKQLR
GQIARRVYRQLLAEKRAEEEKRKREEEEKRKREEEERERERRERAELRAQQEEAARKQRELEALQQESQRAAELSRELE
KQKENKQVEEILRLEKEIEDLQRMKERQELSLTEASLQKLQQLRDEELRRLEDEACRMKQLEDKVEELLSKNYHLENEVA
RLKKLVGERAAEDYKDDDDK

Figure 2.2: Protein Sequences for Full-Length and Artificial Constructs Protein sequences for the full length wildtype *Bos taurus* myosin-10 and the three constructs used in prior single-molecule motility studies, $M10^{short}$-GCN4 (6–8, 63)[19, 108, 109, 123], $M10^{long}$-M5CC [143], and $M10^{long}$-GCN4 [9, 146] constructs.

```
> Full Length
ENKQVEEILRLEKEIEDLQRMKERQELSLTEASLQKLQQLRDEELRRLEDEAC

> M10CCshort-GCN4
GSHENKQVEEILRLEKEIEDLQRMKERQELSLTEASLQKLQLEDKVEELLSKNYHLENEVARLKKLVGE

> M10CClong-M5CC
GSHENKQVEEILRLEKEIEDLQRMKERQELSLTEASLQKLQQLRDEELRRLEDEACRAAKLLKIEARSVERYKKLHIGME
NKIMQLQRKVDEQNKDYKCLMEKLTNLEGVYNSETEKLRNDVERLQLSEEEAKVATGRVLSLQEEIAKLRKDLEQTRSEK
KSIEERADKYKQETDQLVSNLKEENTLLKQEKETLNHRIVEQAKEMTETMERKLVEETKQLELDLNDERLRYQNLLNEFS
RLEE

> M10CClong-GCN4
GSHKENKQVEEILRLEKEIEDLQRMKERQELSLTEASLQKLQQLRDEELRRLEDEACRMKQLEDKVEELLSKNYHLENEV
ARLKKLVGER
```

Figure 2.3: Protein Sequences of Coiled-Coil Constructs Studied. Protein sequences of the constructs used in this study, compared to the full length *Bos taurus* myosin-10 coiled-coil sequence. Sequences include the *N*-terminal residues from the cleavage of the His_6-purification tag. The expected molecular weight of a dimer calculated from the peptide sequence for $M10^{short}$-GCN4, $M10^{long}$-GCN4 and $M10^{long}$-M5CC are 16.32 kDa, 21.4 kDa and 58.32 kDa, respectively.

bility of parallel and antiparallel coiled coils, we envision a structural competition between states, where the ultimate outcome is determined by the balance of favorable and unfavorable interactions. In this structural competition, maximal burial of hydrophobic surface area will be a key consideration.

Here we solve the solution NMR structure of $M10^{short}$-GCN4, and show that it forms an antiparallel coiled coil. This polarity is surprising because $M10^{short}$-GCN4 contains GCN4-p1, a coiled-coil sequence that is parallel on its own. Moreover, the somewhat longer $M10^{long}$-GCN4 has conformational dynamics on the NMR timescale and does not fold with an all-or-none transition, while the much longer $M10^{long}$-M5CC has *structural defects that lead to oligomerization as determined by SAXS*. These structural differences help to explain the conflicting functional studies of the three groups.

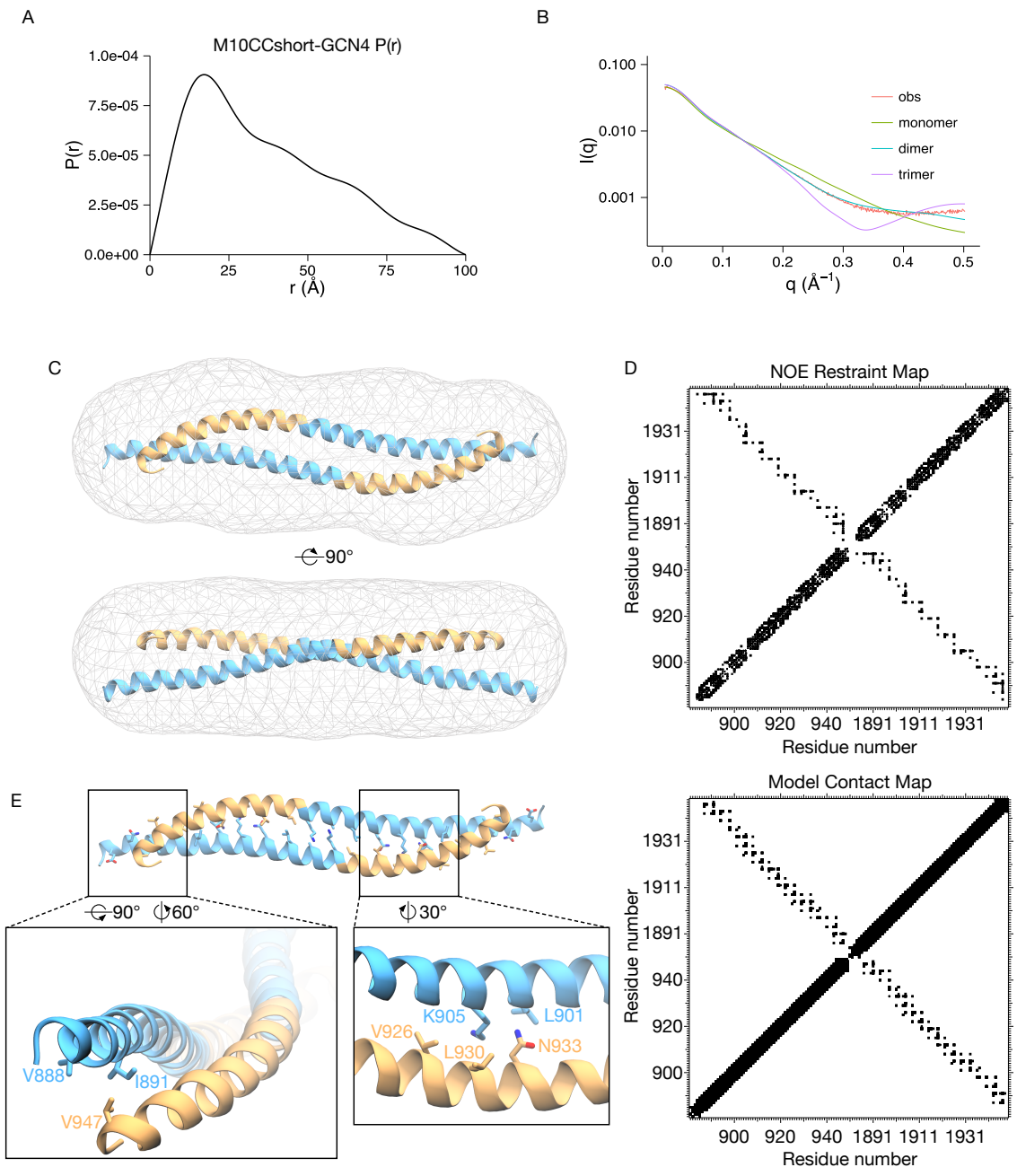

Figure 2.4: M10$^{\text{short}}$-GCN4 is a continuous antiparallel coiled coil. (Continued on the following page.)

Figure 2.4, continued. (A) SAXS radial distance distribution, P(r), with a specified D_{max} of 100 Å. The shape of this curve indicates that a high percentage of atoms in M10^{short}-GCN4 are 15–30 Å apart with the percentage of atoms decreasing as the spacing increases after the maximum. The approximately linear decay after an early peak indicates a rod-like shape, such as a coiled coil [83].
(B) M10^{short}-GCN4 is a dimer. We show the experimental scattering data along with CRYSOL [144] calculated curves for model monomers, dimers, and trimers. The dimer is the final structural model shown in Figures 2.4C, 2.4E (the first out of the ten structures). For the monomer, we deleted one of the chains of the dimer model. For the trimer model, we used the first 69 residues of a long, trimeric coiled coil (PDB ID 2WPQ) [59]. The dimer yields the best fit (reduced ^{2} of 14, 0.73, and 7, respectively).
(C) NMR structure of M10^{short}-GCN4, enclosed by the SAXS envelope generated using DAMMIF (gray mesh). Note that the myosin-10 segment (blue) is paired with GCN4 (orange). This structure corresponds to the antiparallel coiled-coil arrangement in Figure 2.1D. The lowest energy structural model from a pool of 100 calculated structures is shown.
(D) Comparison of the observed NOE restraints grouped by residue (top) with the residue contacts observed in the coordinates (bottom) in (A). Residues in the first chain follow the *Bos taurus* myosin-10 numbering, while residues in the second chain are offset by +1000. The main diagonal shows local NOEs and contacts found in helical structures, while the continuity of the minor diagonal shows restraints and contacts caused by the antiparallel coiled coil. The "X" pattern is indicative of an antiparallel coiled coil.
(E) Selected residue interactions in M10^{short}-GCN4. The bottom-left panel highlights the "hook" at the C-terminus of the coiled coil where V947 interacts with V888 and I891. Although I891 is in an "a" position of the heptad, V888 is in an "e" position, resulting in overwinding of the coiled-coil superhelix at this site. The bottom-right panel illustrates N933, which is a buried "a" position asparagine in GCN4-p1 (N16). In M10^{short}-GCN4 this asparagine is also buried, but without a buried hydrogen bonding partner. A buried "a"-position lysine residue, K905, is also shown to illustrate that its aliphatic chain supports hydrophobic interactions.

2.3 Results

2.3.1 M10^{short}-GCN4 is an Antiparallel Coiled Coil

To resolve the myosin-10 controversy we sought structural information on the three coiled coils (M10$^{\text{short}}$-GCN4, M10$^{\text{long}}$-GCN4, and M10$^{\text{long}}$-M5CC, Figure 2.1A, 2.3). Using a combination of SAXS and NMR, we first solved the solution structure of M10$^{\text{short}}$-GCN4. SAXS reveals that M10$^{\text{short}}$-GCN4 is shaped like a rod (Figure 2.4A, 2.4C). The rod is 100 Å long (D_{max}), which is expected from the length of a 69-residue helical protein. We used DAMMIF [41] to calculate a molecular envelope, shown in Fig. 2C. Importantly, the envelope lacks the dramatic bends seen in the *C*-terminal third of the wildtype myosin-10 coiled-coil structure [96] (Figure 2.1C). The DAMMIF envelope encloses a volume with an expected molecular mass of 15 kDa, consistent with a dimer. Moreover, we calculated scattering curves for model monomers, dimers, and trimers using CRYSOL [144], and find that the dimer yields the best fit to the experimental data (Figure 2.4B, reduced $\Xi 2$ of 14, 0.73, and 7, respectively).

We continued with the full NMR solution structure of M10$^{\text{short}}$-GCN4. The amide region ^{1}H-^{15}N HSQC of M10$^{\text{short}}$-GCN4 contains a single set of well-dispersed peaks, indicating that M10$^{\text{short}}$-GCN4 forms a symmetric homodimer. We found no sign of additional sets of amide peaks over several months, and conclude that no alternative structures form over this time. We were able to assign backbone and sidechain resonances for all but the first three residues of M10$^{\text{short}}$-GCN4 (the thrombin cleavage tag), and proceeded with a solution structure derived from ^{13}C- and ^{15}N-separated NOESY distance restraints.

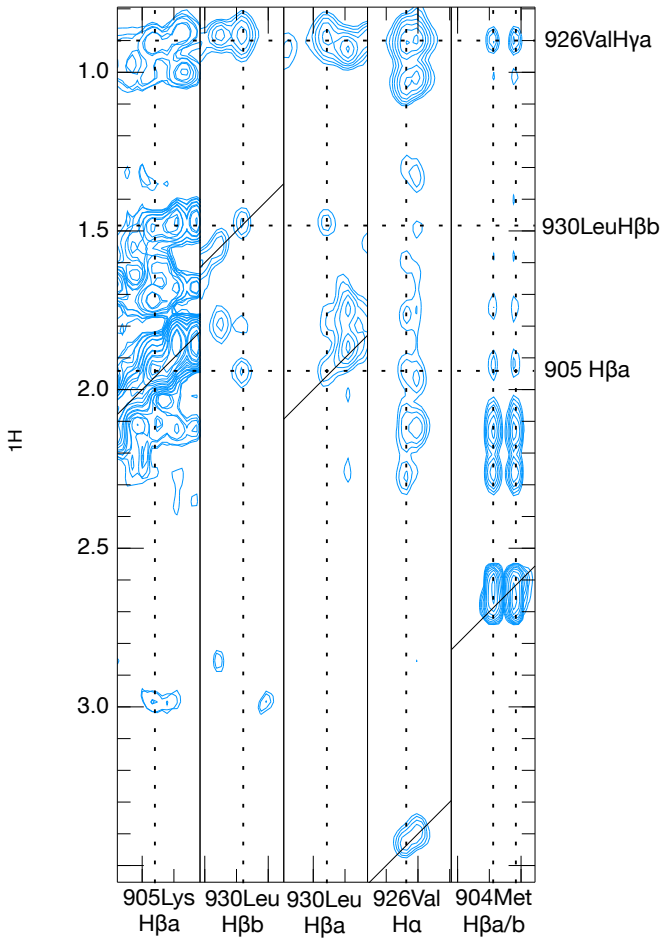

Figure 2.5: Selected aliphatic ^{13}C-NOESY strips illustrating intermolecular NOEs in the vicinity of M904 and K905.

Table 2.1: NMR Structure Statistics.

	M10^{short}-GCN4[a]
Completeness of resonance assignments[b]	
Backbone	96.6%[c]
Side chain	86.4%[d]
Conformationally restricting restraints[e]	
Total distance	1561
Intraresidue [i = j]	332
Sequential [|i - j| = 1]	470
Medium range [1 < |i - j| < 5]	610
Long range [|i - j| >= 5]	153
Intra-chain restraints	1416
Inter-chain restraints	149
Dihedral angle restraints	258
Hydrogen bond restraints	228
Disulfide restraints	0
No. of restraints per residue	15.2
(of those, long-range)	1.1
Residual restraint violations[e]	
Average no. of distance violations per conformer	
0.2 – 0.5 Å	54.0
> 0.5 Å	0.4 (0.526 max)
Average no. of dihedral angle violations per conformer	
1–10°	25.1 (3.9 max)
> 10°	0

Continued on next page

Table 2.1 – continued from previous page

	M10^{short}-GCN4[a]
Model quality[e]	
RMSD backbone atoms for ordered residues	1.3 Å
(all residues)	1.4 Å
RMSD all heavy atoms for ordered residues	1.6 Å
(all residues)	1.7 Å
RMSD bond lengths	0.011 Å
RMSD bond angles	1.6°
MolProbity Ramachandran statistics[e,f]	
Most favored regions	100.0%
Allowed regions	0.0%
Disallowed regions	0.0%
Global Quality Score (Raw / Z-score)[e]	
Verify3D	-0.01 / -7.54
Prosall	0.84 / 0.79
Procheck (-)[e]	1.01 / 4.29
Procheck (all)[e]	0.71 / 4.20
Molprobity clash score	11.87 / -0.51
Model contents	
Ordered residue ranges[f]	883–949
Total no. of residues	138
BMRB acession number	25899
PDB ID code	2n9b

Continued on next page

[a]Structural statistics computed for the ensemble of 10 deposited structures.

[b]Computed using CCPN Quality Reports (21) from the expected number of resonances, excluding highly exchangeable protons (N-terminal, Lys, amino and Arg guanido groups, hydroxyls of Ser, Thr, and Tyr), carboxyls of Asp and Glu, and nonprotonated aromatic carbons.

[c]Unassigned backbone atoms are from the cleavage tag (881-883).

[d]Sidechain assignment statistics for all sidechain atoms (C - C), including residues from the cleavage tag[c]. Considering only C, C, H, and H sidechain atoms (including cleavage tag residues), the assignment percentage is 96.4%.

[e]Calculated using PSVS version 1.5 (22). Average distance violations were calculated using the sum over r^{-6}.

[f]Based on ordered residue ranges [S() + S() > 1.8]. Chain A and chain B follow same numbering scheme.

In general, NOESY distance restraints are challenging to assign in homodimeric systems, because any given NOE may report either an intramonomer or an intermonomer distance. Here, the SAXS envelope provides crucial information to resolve this ambiguity. Because the structure has no significant bends, any long-range NOEs (i - j > 5) must come from intermonomer NOEs in an antiparallel geometry. We find a total of 149 of these long-range, intermolecular restraints out of 1561 total NOE distance restraints (Figure 2.5, Table 2.1).

We combined these distance restraints with dihedral restraints, backbone hydrogen bonding restraints, non-crystallographic symmetry restraints, and distance symmetry restraints to obtain the solution structure shown in Figures 2.4C, 2.4E and 2.6. The remarkable feature of this structure is that the two helices are arranged in a homodimeric, antiparallel coile -coil, despite the fact that $M10^{short}$-GCN4 contains the GCN4-p1 leucine zipper sequence (Figure 2.6, 2.7A–B). Here, the GCN4-p1 sequence pairs with myosin-10 sequence, but surprisingly not with itself. The crossed and uniform pattern of NOE restraints directly supports the

A

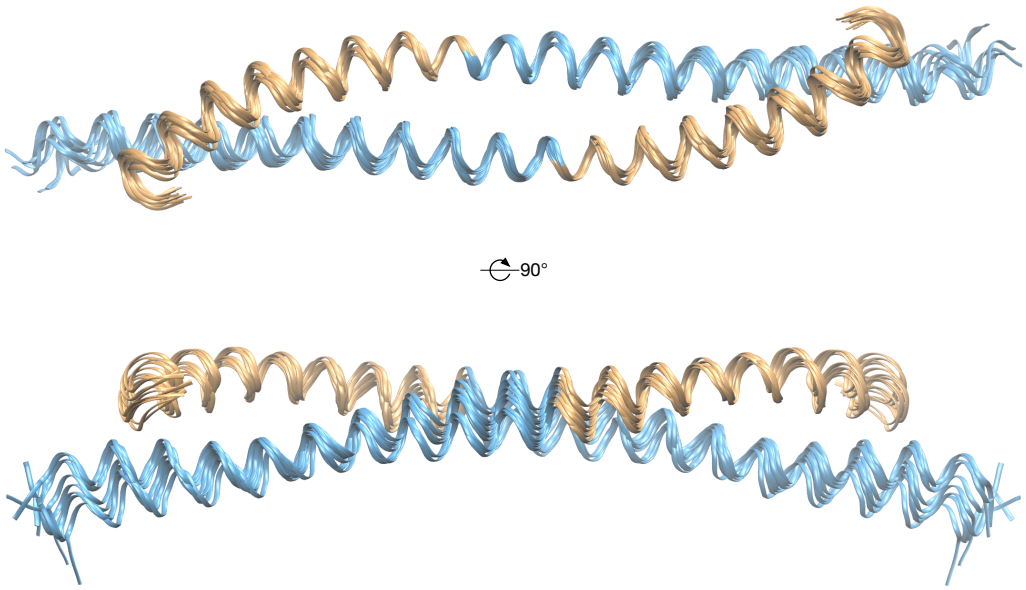

B

```
    890        900        910        920        930        940
QVE EILRLEKEIE DLQRMKERQE LSLTEASLQK LQLEDKVEEL LSKNYHLENE VARLKKLVGE
def gabcdefgab cdefgabcde fgabcdefga bcdefgabcd efgabcdefg abcdefgabc
```

Figure 2.6: (A) Convergence of the M10$^{\text{short}}$-GCN4 NMR structure calculation. Backbones of the ten lowest energy structural models out of 100 calculated models are shown. Blue indicates myosin-10 sequence, yellow indicates GCN4-p1 sequence. The RMSD for the ordered backbone atoms, which include residues 884 to 949, is 1.3 Å. (B) Heptad repeat positions of M10$^{\text{short}}$-GCN4, as determined from the NMR structure using the program TWISTER [142].

antiparallel coiled coil (Figure 2.4D). Thus, certain sequence contexts flip GCN4-p1, directly challenging the assumption that GCN4-p1 enforces a parallel structure.

The structure shows the typical coiled-coil interface with a hydrophobic stripe. Residues at the interface are interdigitated, as is common for antiparallel coiled coils [50]. The angle between the *N*-terminal ends of M10$^{\text{short}}$-GCN4 is 166 8°(SD, over 10 structures), which would tend to splay apart the two myosin-10 motor domains. The *C*-terminal, CGN4 half of M10$^{\text{short}}$-GCN4 has a prominent J-shaped bend (Figure 2.4E). This bend allows V947 to sit in a hydrophobic patch between V888 and I891 (Figure 2.4E, 2.7C). This hydrophobic patch spans "a" and "e" positions in the heptad repeat, and is rotated away from the normal hydrophobic seam. In the Zhang structure [96], the αB helix overlays the αA helix at this exact location (Figure 2.1C). The J-bend leads to an increase in both the coiled-coil radius and pitch near residues 896 and 937 (Figure 2.7D–E).

In GCN4-p1 structures, residue N16 is a well-known example of a buried polar residue [48, 113]. In our structure, this asparagine (N933) also appears in a buried "a" position. However, in our antiparallel structure, N933 sits in a hydrophobic environment near L901 and K905 without a clear hydrogen bonding partner (Figure 2.4E). Consistent with this buried position, the side-chain amide nitrogen, N2, is a upfield chemical shift outlier (105.004 ppm).

Several factors contribute to coiled-coil orientation [50, 55, 56, 111]. Charged side-chains at "e" and "g" positions can form interhelical salt bridges, but M10$^{\text{short}}$-GCN4 would have similar salt bridge patterns in both parallel and antiparallel forms (Figure 2.7A–B). The presence of -branched residues within the hydrophobic seam also favors antiparallel orientations, especially when paired with a -unbranched residues from the partner strand [54]. There are ten of these -branched residues in the "a" positions of M10$^{\text{short}}$-GCN4 (Fig. 2.7A). Six out of ten of these interactions are among the most favorable for antiparallel orientations (four IL pairs, and two VL pairs) [55]. Although GCN4-p1 can be mutated to form antiparallel tetramers [35, 173], M10$^{\text{short}}$-GCN4 is the only known antiparallel and dimeric structure with wildtype GCN4-p1 sequence.

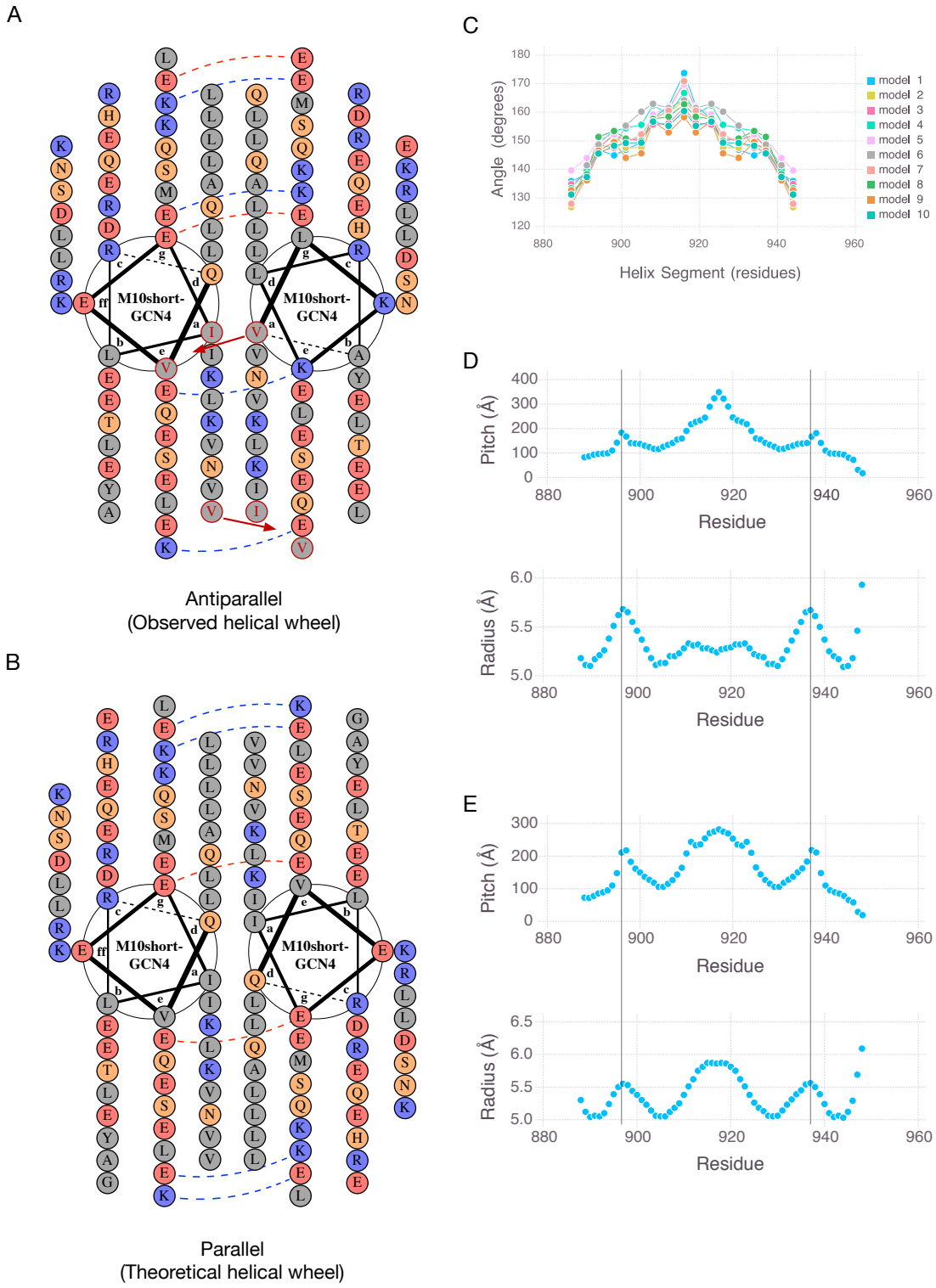

Figure 2.7: Structural features of M10$^{\text{short}}$-GCN4 (Continued on following page.)

Figure 2.7, continued. (A) Helical wheel plot of M10$^{\text{short}}$-GCN4. Note the four favorable and two unfavorable e–g ionic interactions (blue and red dashed lines, respectively). The shifted hydrophobic patches at the J-bends are indicated (red outlines, red arrows). Helical wheels were made using DrawCoil 1.0.
(B) Hypothetical helical wheel plot of M10$^{\text{short}}$-GCN4 in the parallel orientation. The in-register alignment is shown. Note the four favorable and two unfavorable e–g ionic interactions (blue and red dashed lines, respectively), the same as for the antiparallel configuration. Helical wheels were made using DrawCoil 1.0.
(C) M10$^{\text{short}}$-GCN4 bends toward the ends. Helix crossing angles plotted as a function of position along the helix, for all ten models. Crossing angles are measured for 3–4 residue segments starting at the indicated residue on strand A, versus a corresponding segment directly across on strand B. Note the drop in crossing angles towards the end of the structure. The 10 models are the lowest energy structural models from the total pool of 100 calculated structures.
(D, E) A coiled-coil distortion on the proximal side of the J-hook. The coiled-coil pitch and radius are shown for M10$^{\text{short}}$-GCN4 NMR model 1 (D) and model 2 (E), the two lowest energy structural models. Note the peaks indicating increased coiled-coil pitch and radius in the vicinity of residues 896 and 937. Pitch and radius were calculated using the program TWISTER [142].

2.3.2 The Longer Coiled-coil Designs Are Partially Folded

Even though M10$^{\text{short}}$-GCN4 forms antiparallel dimers, the longer M10$^{\text{long}}$-M5CC and M10$^{\text{long}}$-GCN4 have different sequence contexts and might form entirely different structures. We find that both M10$^{\text{long}}$-GCN4 and M10$^{\text{long}}$-M5CC have unusually large hydrodynamic radii, suggesting that they may form larger complexes at high concentration (Figure 2.8A). We compared amide-region ^{15}N-HSQC spectra of M10$^{\text{short}}$-GCN4 (Fig. 2.8B) and M10$^{\text{long}}$-GCN4 (Fig. 2.8C), and observe fewer amide peaks than expected. The poor spectral dispersion and considerable peak overlap for M10$^{\text{long}}$-GCN4 prevents the assignment of backbone amide peaks and is a direct indicator of conformational dynamics on the NMR timescale. Moreover, M10$^{\text{long}}$-GCN4 HSQC spectra are strongly temperature dependent from 25–45 °C and show signs of additional flexibility at the higher temperatures (Fig. 2.9A–C). A comparison of M10$^{\text{long}}$-GCN4 peak locations with those of the wild type myosin-10 coiled coil, GCN4-p1 [127], and M10$^{\text{short}}$-GCN4 shows no overlapping peaks, suggesting that M10$^{\text{long}}$-GCN4 is structurally dissimilar to all three.

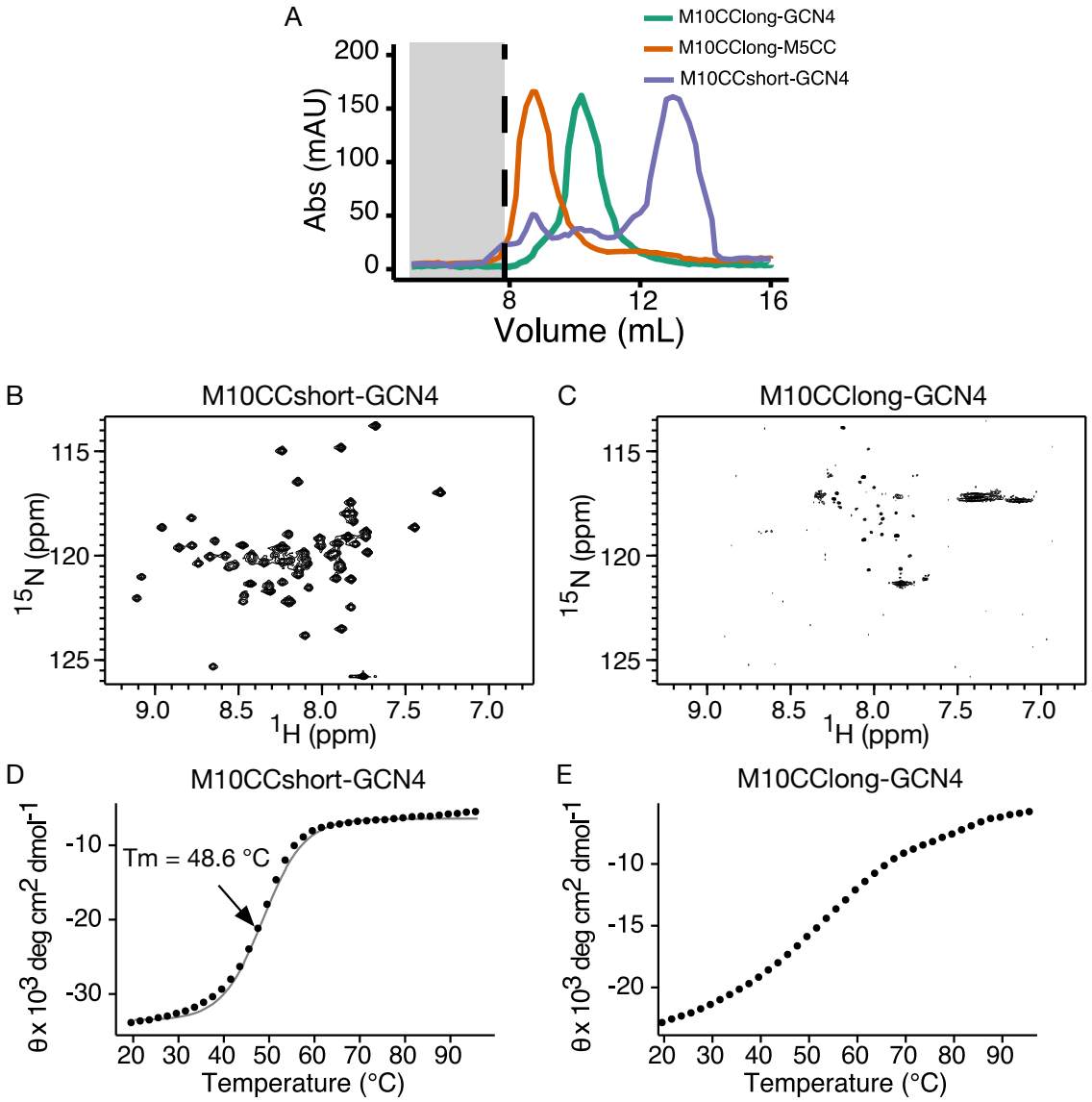

Figure 2.8: M10$^{\text{long}}$-GCN4 is dynamic and lacks an all-or-none folding transition.
(A) Preparative gel filtration chromatograms from the final stage of purification of M10$^{\text{short}}$-GCN4, M10$^{\text{long}}$-GCN4, and M10$^{\text{long}}$-M5CC. These three proteins elute at 23, 71, and 130 kD, respectively. All three elute at larger masses than predicted from globular standards, as expected for rodlike molecules. However, M10$^{\text{long}}$-GCN4 elutes at a much greater MW than M10$^{\text{short}}$-GCN4, even though these two constructs are of similar length.
(B) The amide-region ^{1}H-^{15}N HSQC spectrum of M10$^{\text{short}}$-GCN4 illustrates good peak dispersion.
(C) The corresponding M10$^{\text{long}}$-GCN4 HSQC has poor dispersion and has fewer peaks than backbone amides, indicative of conformational dynamics.
(D) The M10$^{\text{short}}$-GCN4 circular dichroism (CD) melting curve at 222 nm shows a cooperative unfolding transition.
(E) The corresponding M10$^{\text{long}}$-GCN4 CD shows gradual helical fraying without evidence of a cooperative transition.

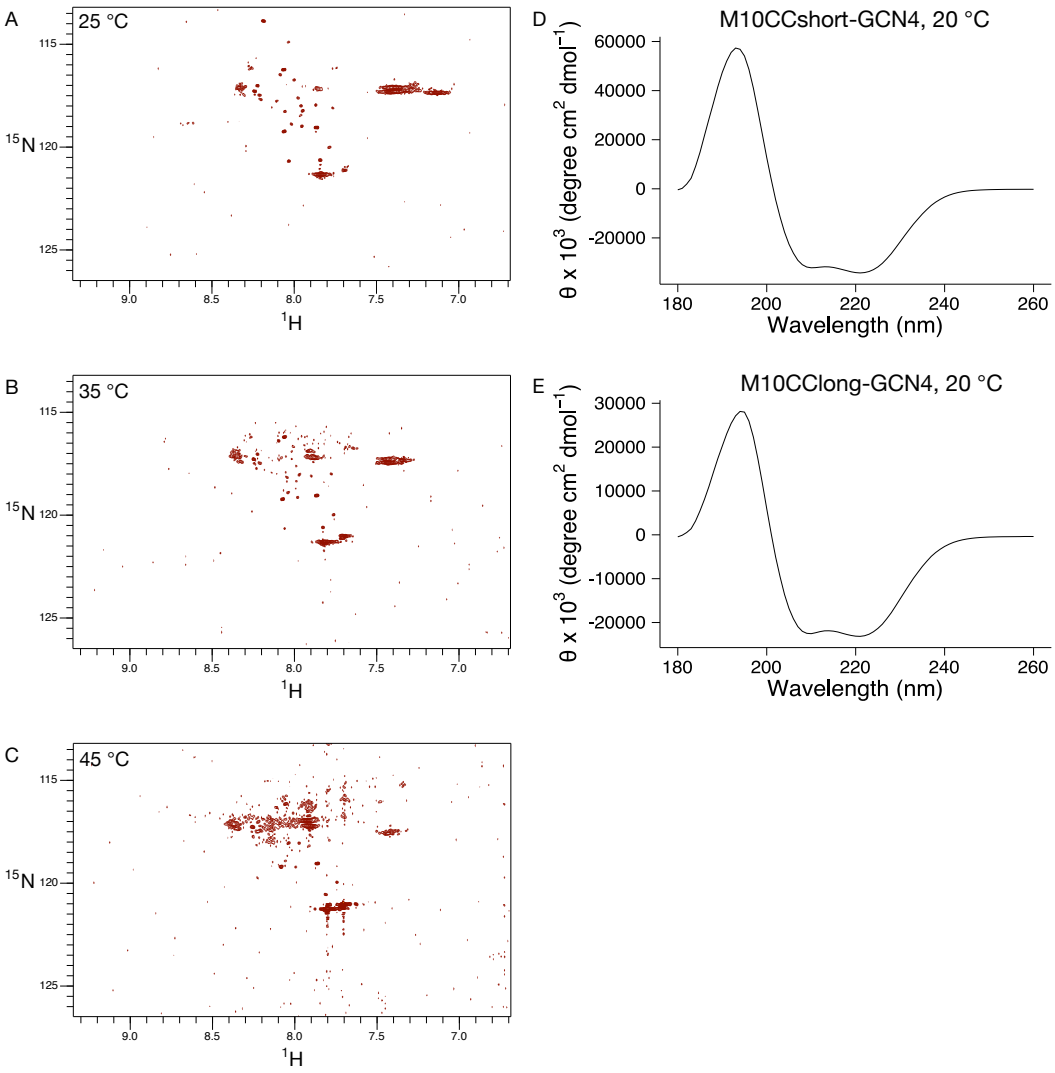

Figure 2.9: A series of ^{1}H-^{15}N HSQC spectra of M10$^{\text{long}}$-GCN4 taken at (A) 25 °C, (B) 35 °C, and (C) 45 °C and visualized at the same NMR signal levels. Note the absence of clearly defined peaks at all temperatures compared to the HSQC for M10$^{\text{short}}$-GCN4 (Figure 2.8A) and the gradual disappearance and smearing of signal as the temperature increases.
(D,E) Circular dichroism spectra of M10$^{\text{short}}$-GCN4 (D) and M10$^{\text{long}}$-GCN4 (E) at 20 °C, at the start of the thermal denaturation in Figure 2.8B, 2.8E. The concentration of both proteins is 40 M. Both constructs are largely -helical, as indicated by their shape and the large ellipticity at 222 nm. Assuming a peptide with 100% -helical structure has a mean residue ellipticity given by $[\Theta]_{222\ pred} = 4.0 \times 10^4(1 - 4.6/n)$, where n = number of residues in a peptide, we can estimate the -helical percentage as $([\Theta]_{222\ obs}/[\Theta]_{222\ pred}) \times 100$, where $[\Theta]_{222\ obs}$ is the measured mean residue ellipticity (64). Based on these calculations, M10$^{\text{short}}$-GCN4 is 91% helical and M10$^{\text{long}}$-GCN4 is 61% helical.

To compare the secondary structure stability of M10^{short}-GCN4 and M10^{long}-GCN4, we used circular dichroism (CD) thermal denaturation. M10^{short}-GCN4 unfolds cooperatively at increasing temperature, with a sigmoidal response in mean residue ellipticity at 222 nm and a T_m of 48.6 °C (Fig. 2.8D, 2.9D). However, M10^{long}-GCN4 gradually melts without cooperativity, an additional indicator of a frustrated, flexible structure (Fig. 2.8E, 2.9E).

Interestingly, the M10^{long}-GCN4 must still self-assemble, as assembly is a prerequisite for processive myosin motility. We note that M10^{long}-GCN4 is 61% helical (Figure 2.9E) and contains a heptad repeat that would tend to form a continuous hydrophobic seam, even though it lacks folding cooperativity. Note that certain molten globule protein states can form specific intra- or intermolecular interactions, despite their considerable flexibility [7]. Takagi *et al.* observed HMM dimers containing M10^{long}-GCN4 in their electron microscopy (EM) images [146]. However, these Takagi EM images also suggest flexibility in their construct. The two motor domains sample a wide range of angles, similar to myosin-5, and are not splayed apart at 180°[146]. Note that interactions with the carbon grid might affect the orientation distribution, so some caution is needed when inferring flexibility from EM images.

At 243 residues per monomer, M10^{long}-M5CC is too large for NMR, so we instead used SAXS to characterize its structure. Comparing the M10^{short}-GCN4 and M10^{long}-M5CC Guinier plots (Figure 2.10A, 5B), M10^{long}-M5CC is either aggregated or quite large with an R_g of 126 Å. The radial distribution function shows that the maximum dimension of M10^{long}-M5CC is at least 500 Å. This distance is much longer than expected from a single, parallel coiled coil with the length of the M10^{long}-M5CC sequence (Figure 2.10C–D). To explain this observation, we propose that the long, stable myosin-5 sequence forms a parallel coiled coil, which prevents the *N*-terminal myosin-10 segment from folding. Thus, M10^{long}-M5CC is in a parallel, frustrated state (Figure 2.1D). At the high concentrations used in SAXS, we suspect that antiparallel segments from different dimers can pair to generate oligomers with a longer end-to-end distance. At the low concentrations used in single-molecule experiments

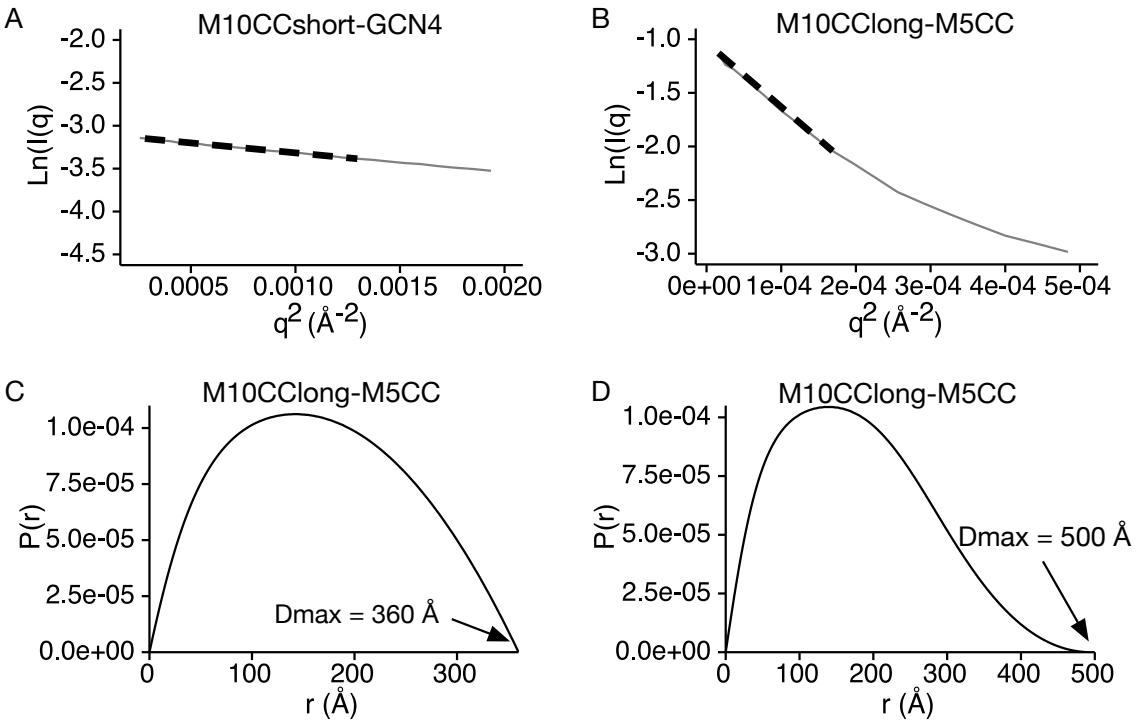

Figure 2.10: $M10^{long}$-M5CC aggregates or assembles. (A) The SAXS Guinier region of $M10^{short}$-GCN4 is linear, and yields a R_g of 27 Å, consistent with the 30 Å R_g expected for a rod with a length of 100 Å. (B) The Guinier region of $M10^{long}$-M5CC is unusually narrow, yielding an R_g of 126 Å. (C) The $M10^{long}$-M5CC radial distribution function, P(r), calculated using using a maximum distance, D_{max}, of 360 Å. This length corresponds to a rod model where the entire $M10^{long}$-M5CC sequence is a parallel coiled coil. Note the abrupt decay at high r, indicative of an underestimated D_{max}. (D) The best D_{max} of $M10^{long}$-M5CC is 500 Å, with a real-space R_g of 138 Å. Thus, $M10^{long}$-M5CC likely forms an oligomeric structure that is longer than a single dimer under these conditions.

[143], the myosin-10 segments are likely frustrated and have conformational dynamics much like M10^{long}-GCN4.

2.4 Discussion

We have found that fused parallel and antiparallel coiled coils can adopt surprising and unpredictable structures, depending on their exact sequences. To determine the prevalence of orientation switching in sequences that contain GCN4-p1, we performed a BLAST search against the PDB using GCN4-p1 as the query sequence. We found three reports of antiparallel forms of GCN4 [35, 64, 174]. However, these examples differ because all are mutants of GCN4-p1 and all are trimers or tetramers. The M10^{short}-GCN4 is the first reported structure of orientation switching in a dimer with a wildtype GCN4-p1 sequence. For this fused parallel and antiparallel coiled coil, it is energetically favorable to force the GCN4 sequence to be antiparallel, rather than to force the myosin-10 sequence to be parallel.

Why does M10^{short}-GCN4 fold, while M10^{long}-GCN4 and M10^{long}-M5CC each have structural issues? The problem may be that M10^{long}-GCN4 and M10^{long}-M5CC designs include the full myosin-10 bend (Figure 2.1A, 2.1C), with the skips in the heptad repeat. Although Zhang proposed that the longer M10^{long}-M5CC could fold in the genie-bottle form with an intact, antiparallel myosin-10 coiled coil [96], the linkers between the parallel and antiparallel segments are likely too short. Such extended linkers can be challenging to design [80]. In contrast, the M10^{short}-GCN4 design has a continuous heptad repeat that accommodates a straight coiled coil, albeit an antiparallel one. Although the dimerization affinity of GCN4-p1 is much higher than the myosin-10 coiled coil (K_D of 26 nM vs. 590 nM) [81, 96], affinity alone does not determine the orientation. Indeed, coiled-coil orientation and oligomerization state are difficult to predict due to a combinatorial explosion of possible interactions [51].

The M10CC^{short}-GCN4 forms an antiparallel coiled coil through a structural competition where the myosin-10 segment overrules the GCN4-p1 segment. Certain natural and

engineered protein functions exploit such structural competition. For example, the dramatic rearrangements in the core HA_2 domain of hemagglutinin harness structural competition to drive membrane fusion [21, 93] . Moreover, a Zn^{2+} transporter called the "Rocker" uses structural competition to allow only one of two metal-binding sites to be occupied simultaneously as part of its design [72].

How might an antiparallel coiled coil affect the stepping of myosin-10? Zhang proposed that the antiparallel coiled coil extends the reach of myosin-10, allowing both motor domains to contact a single actin filament. In this model, the coiled coil acts as a "shoulder" that spaces two "arms" [96]. However, our earlier work refutes this proposal. We can disrupt selectivity of myosin-10 by inserting a swivel (a flexible glycine-serine linker) at the *N*-terminus of the coiled coil [109]. In the Zhang model, the ends of the coiled coil are intrinsically flexible, analogous to the rotator cuff of the shoulder. If the Zhang model were correct, additional flexibility from our linker insertion should have had no effect on myosin-10 stepping.

We propose an alternative model, extending our original proposal that myosin-10 walks by straddling two actin filaments in a bundle. The key feature is that the two SAH domain helices project from the coiled coil without breaks in the helical structure, on average. In an actin filament bundle, myosin-10 can reach adjacent actin filaments with a gradual SAH domain bend (Figure 2.11A) [6, 137]. However, myosin-10 cannot place both motor domains on a single filament without considerable strain (Fig ure 2.11B). Such strain would increase the likelihood of detaching before successfully completing a step on a single filament. Antiparallel coiled coils and oriented SAH domains would therefore favor walking on bundles. Likewise, a dynamic dimerization region breaks this bundle selection mechanism (Figure 2.11C).

Single molecule TIRF motility assays can select for populations of walking myosins. Therefore, the prior studies on myosin-10s with $M10^{long}$-GCN4 or $M10^{long}$-M5CC may have detected populations that were structured and oriented to allow motility on single filaments. However, for these populations to remain processive for 40-60 steps, the structural states

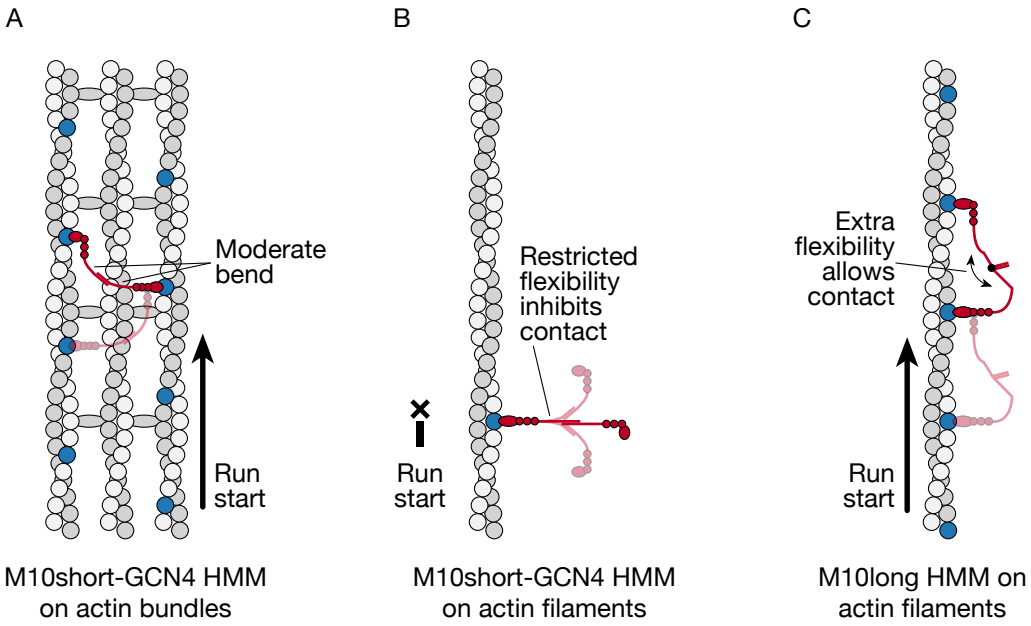

Figure 2.11: A model for bundle selection using antiparallel coiled coils.
(A) Myosin-10 straddles two different actin filaments in a fascin-actin bundle. Starting and ending myosin-10 configurations for one step are shown, with the starting state in transparent red and the ending state in solid red. The most common target actin-binding sites are highlighted in blue. The moderate bend of the SAH:coiled coil:SAH elements (thin curved line) allows both motor domains to engage separate actin filaments.
(B) Myosin 10 on a single actin filament, with one bound motor domain. The antiparallel coiled coil forces the free motor domain to project away from the only available actin filament. Moderate flexibility, illustrated using transparent motors, inhibits rebinding to actin. Processivity is greatly reduced with significantly shorter runs.
(C) Additional flexibility at the coiled coil allows the free motor domain to reach the actin, and enables processive stepping. Flexible HMM constructs include those containing $M10^{long}$-GCN4, $M10^{long}$-M5CC, or the swivel [109]. Although the dimerization domain is likely dynamic, for simplicity it is illustrated here with a short parallel segment. Note that all myosin motor domains are shown with arbitrary lever arm orientations as these are currently unknown.

would have to exchange slowly, on timescales longer than several seconds. If this slow exchange were happening, we would expect to see multiple full sets of amide peaks in the NMR of M10$^{\text{long}}$-GCN4, one set for each structural state. Instead, we see a spectrum that is typical for a dynamic protein with little tertiary structure.

A comparison of the wildtype myosin-10 coiled-coil structure with our M10$^{\text{short}}$-GCN4 structure finds that both orientations are similar. The *N*-terminal ends of both structures project at nearly the same large angle (Zhang: 161 7†, M10$^{\text{short}}$-GCN4: 166 8°, SD over top ten structures, Fig. 2.12). Thus, we expect that this bundle selection mechanism would operate in wildtype myosin-10 as well. The main structural difference is that the M10$^{\text{short}}$-GCN4 is about twice as long as the wildtype myosin-10 coiled coil (100 Å vs. 45 Å, respectively, Fig. 2.12). Although we cannot rule out that a particular coiled-coil length is critical for actin bundle selection, we suspect that orientation is much more important. For example, when we replace the myosin-5 coiled coil with the myosin-10 SAH + M10$^{\text{short}}$-GCN4 sequences, we make a bundle-selective myosin-5 [109]. This selective myosin-5 has six additional IQ domains compared to myosin-10, and is over 200 Å longer.

The approach of fusing GCN4-p1 and its mutants to assemble proteins is common (45–49)[20, 61, 90, 125, 168]. In many of these applications, dimerization is the primary consideration and the final orientation of the dimer is only of secondary importance. However, in certain proteins the orientation will strongly affect function. With motor proteins in particular, dimerization domains can profoundly affect activity. Our results provide cautionary evidence that coiled-coil sequences containing GCN4-p1 may be either parallel or antiparallel, and that orientation must be established through independent structural work.

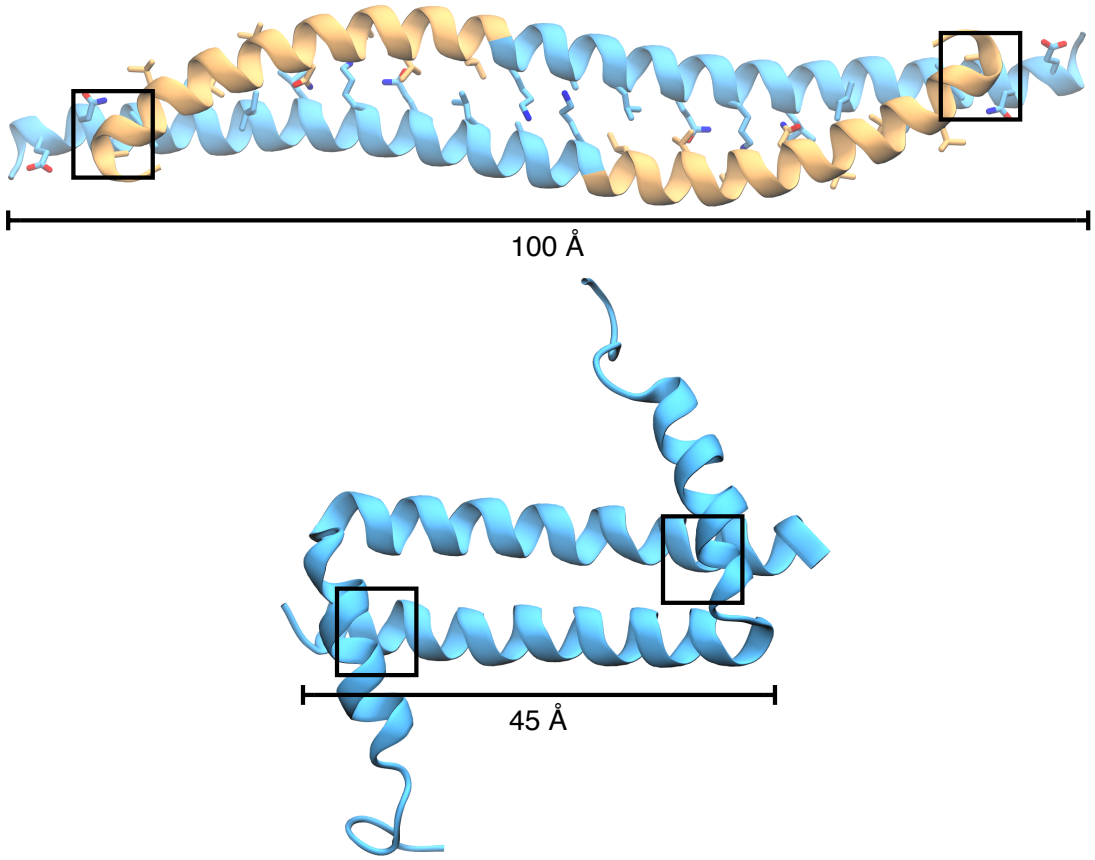

Figure 2.12: Structural comparison of M10$^{\text{short}}$-GCN4 (top) and the wildtype myosin-10 coiled coil (bottom) [96]. The *N*-terminal ends (back helices) of the M10$^{\text{short}}$-GCN4 span 166 8°, while the corresponding *N*-terminal ends (back helices) of the Zhang structure span 161 7°(SD over top ten structures). Thus, the orientation of the important upstream SAH, IQ, and motor domains should be nearly identical. However, M10$^{\text{short}}$-GCN4 is about twice as long as the Zhang coiled coil. Boxes indicate the hydrophobic patches on the back helices that are illustrated on the helical wheel plot in Fig. 2.4A and in Fig. 2.7E. These patches are covered by the J-hooks in M10$^{\text{short}}$-GCN4, and the B helices in the Zhang structure.

2.5 Materials and Methods

2.5.1 Vector Design and Cloning

Myosin-10 (*Myo10*), myosin-5, and GCN4 DNA sequences were PCR amplified with homologous ends to create the M10$^{\text{short}}$-GCN4 and M10$^{\text{long}}$-M5CC constructs [108, 143] (Fig. 1). Sequences were designed with the coiled coil immediately following the *N*-terminal thrombin cleavage tag, with no extra *C*-terminal residues. PCR reactions were performed using Pfu Turbo polymerase (Agilent). M10$^{\text{long}}$-GCN4 was made from a gBlock (Integrated DNA Technologies) containing myosin-10 coiled coil and GCN4-p1 DNA fragments [146]. These constructs were cloned into pET-15b (Novagen) linearized by NdeI (New England Biolabs) following the Gibson Assembly [45] (for M10$^{\text{short}}$-GCN4) and SLiCE cloning [177] protocols (for M10$^{\text{long}}$-M5CC and M10$^{\text{long}}$-GCN4) with homemade cloning mixes.

2.5.2 Protein Expression

Coiled coils were expressed in BL21(DE3) pLysS *E. coli* cells (EMD Millipore) grown in either terrific broth or M9 minimal media (for NMR studies). After overnight expression, cells were lysed in high-salt lysis buffer (50 mM HEPES, 500 mM NaCl, 10 mM imidazole, 5% v/v glycerol, 5 mM BME, pH = 7.5) using microfluidization. The lysate was clarified by centrifugation and applied to a 30 mL Ni-NTA Superflow (Clonetech) column. The column was washed with 5 CV wash buffer (lysis buffer with 20 mM imidazole), 5 CV second wash buffer (lysis buffer with 50 mM imidazole), and 6 CV elution buffer (lysis buffer with 250 mM imidazole). The fractions with protein were pooled, concentrated and desalted into thrombin cleavage buffer (20 mM Tris-HCl and 100 mM NaCl, pH 7.5) using an Amicon Ultra Ultracel-3 (EMD Millipore). The His-tag was removed by cleavage with human -thrombin (Haematological Technologies, Inc.) at room temperature for 4.5 hours with nutation. The thrombin reaction was quenched with PMSF, and cleaved protein was separated from uncleaved protein and the $(\text{His})_6$ tag by another pass over Ni-NTA, retaining

the flowthrough. Protein was pooled and concentrated using an Amicon Ultra Ultracel-3 and was further purified by gel-filtration on a Superdex 75 30/100 GL column. Buffer conditions for gel filtration and further dialysis steps are detailed below for each experiment. The gel filtration column was calibrated with a reference set of protein markers (Sigma MWFGF70).

2.5.3 NMR Measurements

Proteins were prepared in in 100 mM potassium phosphate, 1 mM EDTA, pH 6.5. Pooled and concentrated fractions were dialyzed in gel filtration buffer plus 0.03% w/v sodium azide. Chemical shift assignments were made using standard protein NMR methodology. Preliminary HSQC-TROSY experiments were conducted on a 600 MHz Bruker spectrometer at the Biomolecular NMR Core at the University of Chicago. Final NMR experiments were executed at the University of Minnesota NMR Center on a Bruker Ascend 850 MHz spectrometer equipped with a TCl CryoProbe, with the sample temperature held constant at 308 K. The HN(CA)CO experiment was performed on a Varian 600 MHz spectrometer equipped with a ^{13}C enhanced cold HCN Z-gradient probe. HNCA, HN(CO)CA, HNCO, HN(CA)CO CBCA(CO)NH, and CBCANH experiments were used to assign the backbone atom resonances for residues 883 through 949. Likewise, HCCCONH, HBCBCGCDHD, HCCH-TOCSY and HCCH-COSY spectra were used to assign the sidechain ^{1}H and ^{13}C resonances for residues 884 through 949, all the M10$^{\text{short}}$-GCN4 residues. Distance restraints were obtained from 3D ^{15}N-NOESY (200 ms mixing time) and 3D ^{13}C-NOESY (200 ms mixing time) experiments. Data were processed using NMRPipe [34] and analyzed using the CCPNMR software suite [163].

NOE peak volumes were calibrated using the the average NOE volume from geminal H atoms and classified into the following distance bins: short (1.8 – 3.7), medium (1.8 – 5.0) and long (1.8 – 6.0). Dihedral constraints were calculated using TALOS+ software [134]. NOE distance constraints were imported into XPLOR-NIH and used for NMR structure calculation [131]. We generated a composite containing 10 lowest-energy structures from 100

calculated structures. We used The Protein Structure Validation Suite (PSVS), version 1.5 [15] to validate structures, and VMD and VMD-Xplor to generate molecular representations [67]. The SBGrid Consortium provided software binaries [106].

2.5.4 Small-Angle X-ray Scattering

Samples were purified as described above, using 50 mM Tris-HCl and100 mM KCl at pH 7.5 for the gel filtration step. The samples were concentrated and dialyzed into gel filtration buffer containing 5% v/v glycerol. $M10^{long}$-M5CC samples contained 5 mM 2-mercaptoethanol as a reducing agent during the purification steps and 5 mM DTT during the dialysis and data collection steps. X-ray scattering data as a function of the momentum transfer were collected on beamline 12-ID-B at the Advanced Photon Source, Argonne National Laboratory. Samples were purified as described above and syringe filtered before being loading into a capillary tube. A Hamilton syringe pump agitated the samples in the capillary during X-ray exposure to minimize sample damage. $M10^{short}$-GCN4 was exposed at 15 mg/mL, 7.5 mg/mL, and 3.8 mg/mL, and $M10^{long}$-M5CC was exposed at 12 mg/mL, 6 mg/mL, and 3 mg/mL to create a dilution series. SAXS data were collected continuously over a range of Q from 0.004 to 1.00 $Å^{-1}$. Buffer blanks (50 mM Tris-HCl, 100 mM KCl and 5% v/v glycerol at pH 7.5) matched to each sample were recorded and subtracted from the sample data before data averaging. The final experimental scattering curve was calculated using ALMERGE [42] to scale the averaged datasets for each concentration to the highest concentrations (15 mg/mL for $M10^{short}$-GCN4 and 12 mg/mL for $M10^{long}$-M5CC), merge the data sets, and extrapolate to zero concentration (Figure 2.13). The data were analyzed using the ATSAS software suite [118] to determine radii of gyration with AUTORG and distance distributions with DATGNOM [119]. The $M10^{short}$-GCN4 dummy atom model was generated using DAMMIF [41] and DAMAVER [162] and subsequently processed using the Situs software suite to generate a wireframe envelope representation and align the envelope to the $M10^{short}$-GCN4 NMR structure [172]. The SBGrid Consortium provided software

binaries [106].

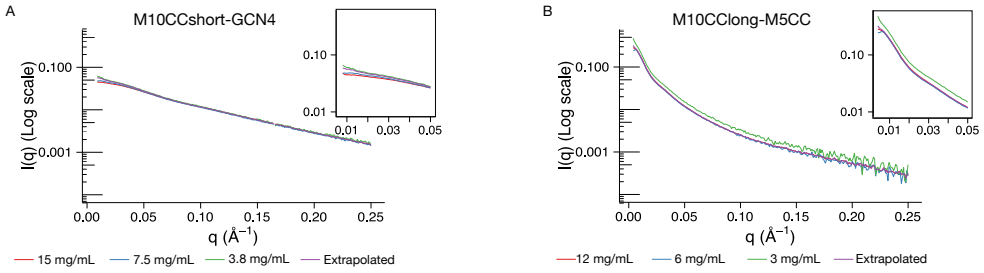

Figure 2.13: Averaged and buffer subtracted small-angle X-ray scattering data for (A) M10$^{\text{short}}$-GCN4 and (B) M10$^{\text{long}}$-M5CC at high, medium, and low concentrations (indicated in the key below each plot). Extrapolated curves are derived using ALMERGE. The inset shows the low-Q plots for comparison.

2.5.5 Circular Dichroism

A Jasco J-1500 spectropolarimeter (Jasco) was used for all CD spectra and melting curves. CD spectra were collected from 20 °C to 98 °C with 2 °C increments, 3 spectra per temperature, 1 nm bandwidth. Samples equilibrated for 2 minutes at each temperature point. Each spectrum was measured from 260 nm to 180 nm, and the melting temperature was analyzed at 222 nm using SigmaPlot 12.0 (Sigmaplot) to produce a sigmoidal fit that was replotted using ggplot2 [169].

2.6 Author Contributions

KCV, YX, and RSR designed research; KCV and YX performed research; KCV, YX, and RSR contributed analytic tools; KCV and RSR analyzed data and wrote the manuscript.

2.7 Acknowledgments

The authors thank Gianluigi Veglia and Shohei Koide for critical evaluation of the NMR work and manuscript, Ed Taylor for comments on the manuscript, Elena Solomaha for assistance with the circular dichroism studies, Eduardo Perozo and Francisco Bezanilla for

instrumentation, and members of the Rock lab for support. SAXS data collection was aided by Xiaobing Zuo and the staff at beamline 12-ID-B at the Advanced Photon Source, Argonne National Laboratory (GUP38797), supported by the U.S. Department of Energy under contract number DE-AC02-06CH11357. This work was supported by NIH R01s GM078450 and GM109863 (to R.S.R.) and NIH T32 GM007183 (to K.C.V). Funding for NMR instrumentation was provided by the Office of the Vice President for Research, the Medical School, the College of Biological Science, NIH, NSF, and the Minnesota Medical Foundation. We acknowledge the University of Chicago Research Computing Center for support of this work.

The Protein Data Bank accession code for M10$^{\text{short}}$-GCN4 is 2N9B. NMR data are archived in the BMRB under accession code 25899.

CHAPTER 3

SINGLE-ALPHA HELIX DOMAINS ENHANCE MYOSIN-10 COILED-COIL BUNDLE SELECTION PROPERTIES

3.1 Introduction

Recently, much attention has been given to the coiled-coil domain of myosin-10, the site where dimerization occurs. While the most surprising feature of this domain has been its antiparallel orientation [96], individuals who study the motility of myosin-10 are agreeing that this unique orientation leads to bundle selectivity and could assist myosin-10 in localizing to cellular filopodia [22, 159]. However additional leg domains connect the motor foot, the most N-termal myosin-10 domain, to the coiled coil, so other features must also contribute to myosin-10 cellular motility. The single alpha helix (SAH) is directly next to the coiled-coil domain, and is a composed of a sequence that favors the formation of a non-oligomerizing alpha helix (Figure 3.1, upper).

A traditional coiled coil contains a protein sequence forming a heptad repeat, with positions labelled as "a-g", based on the positions of residues within the helices. The hydrophobic residues in a coiled coil, which are located at positions "a" and "d", form a hydrophobic seam that favors the formation of dimers [35, 51]. In contrast, SAH domains have charged residues located at positions "a" and "d", which lead to the formation of stable, helical monomers that do not favor dimers or oligomers [115]. SAH domains are stabilized by oppositely charged residues spanning between individual turns in the alpha-helix, which helps increase the stability of the SAH in solution [114].

Initially the predicted coiled-coil region for myosin-10 was defined to be residues 813-962. A previous study demonstrated that a peptide derived from murine residues 808-843 form a stable, single-alpha helix [82]. This is not surprising due to the fact that both SAH domains and coiled coils have a heptad repeat, which is one of the methods used to search for coiled coils in sequence-based prediction tools [115]. Residues in the "a" and "d" positions of coiled-

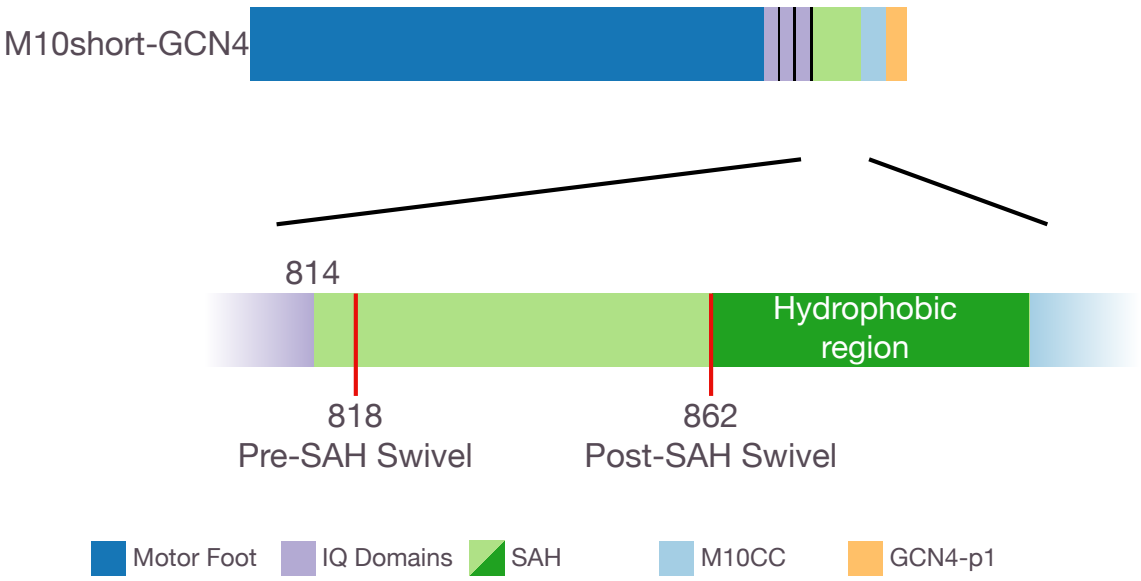

Figure 3.1: Sequence diagram of M10short-GCN4 highlighting addition of flexible linkers to make swivel constructs. Upper: Diagram of shortened myosin-10 fragment used to characterize myosin-10 motility in single molecule studies (will cite when citation available) [108, 109, 123]. The SAH domain (light green) connects to the N-terminus of the coiled-coil domain(light blue), the minimal myosin-10 dimerization domain [96, 159]. Lower: Residues 814–883 are defined as the SAH domain, with residues 814-862 being the charged portion of the SAH domain (light green) and hydrophobic residues interspersed with charged residues 862–883 (dark green). Previous research was performed on the charged region of the SAH domain, which led to the motivation to insert flexible linker regions (-GSGGSG-) at either residue 818 or residue 862 to produce the Pre-SAH Swivel and Post-SAH swivel domains, respectively. These insertion points are marked by red lines.

coil heptad repeats are hydrophobic, and these residues are involved in the intermolecular interactions between the proteins that form the hydrophobic seam that forms an interface allowing hydrophobic sidechains to be buried from solution [25, 51]. SAHs can also have a similar hydrophobic repeat, with charged residues more likely to occupy the "a" and "d" positions of the heptad repeat [25, 115].

Due to the similarities in sequence motifs, the location of the boundary between myosin-10's SAH and coiled-coil domains was under debate, leading some to believe that myosin-10 even is monomeric [109, 114, 143]. Previous work introduced flexibility before the SAH domain, and also after the SAH domain These domains must also play roles for assisting the coiled coil in forcing bundle selectivity. The myosin-10 dimerization study showed that the minimal coiled-coil domain comprised of *Homo sapiens* residues 883-934. NMR experiments demonstrated that the expressing different lengths of SAH domain before the coiled coil did not alter the dimerization stability or resolvable chemical shifts from the coiled-coil domain [97]. Sedimentation ultracentrifugation determined that the minimal coiled coil forms a dimer, and the addition of residues either N-terminal or C-terminal to the coiled coil do not affect the dimerization ability of myosin-10 [96]. Even though this domain does not directly interact with the coiled coil, the role of the SAH domain in myosin-10's behavior and the relation between the SAH domain and the coiled-coil domain have not been previously tested. Additionally the entirety of the SAH domain, inclusive of *Bos taurus* residues 814–883, has not been tested for its secondary structure and flexibility. Therefore a better understanding of the SAH domain and the SAH–coiled coil tandem domain will provide complementary information to how the coiled-coil orientation can affect myosin-10 behavior and bundle selection previously noted in cells [97, 96, 114, 159].

We used a combination of small-angle X-ray scattering and molecular modelling to test the flexibility of the SAH domain, and the SAH domain attached to coiled coils. SAH–CC tandems were created from wild-type *Homo sapiens* and M10$^{\text{short}}$-GCN4 and were also studied using the same methods as SAH domains to measure the degree of flexibility between

```
                    : 1---------11--------21--------31--------41--------51--------61-------- :
OrigSeq             : EKRAEEEKRKREEEEKRKREEEERERERERREAELRAQQEEAARKQRELEALQQESQRAAELSRELEKQK : OrigSeq

Jnet                : --HHHHHHHHHHHHHHHHHHHHHHHHHHHHHHHHHHHHHHHHHHHHHHHHHHHHHHHHHHHHHHHHH-- : Jnet
jhmm                : --HHHHHHHHHHHHHHHHHHHHHHHHHHHHHHHHHHHHHHHHHHHHHHHHHHHHHHHHHHHHHHHHH-- : jhmm
jpssm               : --HHHHHHHHHHHHHHHHHHHHHHHHHHHHHHHHHHHHHHHHHHHHHHHHHHHHHHHHHHHHHHHHH-- : jpssm

Lupas 14            : ----------------------------------------CCCCCCCCCCCCCcccccccccc----- : Lupas 14
Lupas 21            : --ccccccccccccccccccccc----------CCCCCCCCCCCCCCCCCCCCCCCCCCCCCCCCCC- : Lupas 21
Lupas 28            : --CCCCCCCCCCCCCCCCCCCCCCCCCCCCCCCCCCCCCCCCCCCCCCCCCCCCCCCCCCCCCCCCC- : Lupas 28

Jnet_25             : ----------------------------------B--B--B-------B-BB---------B---B---- : Jnet_25
Jnet_5              : ------------------------------------------------------------------------ : Jnet_5
Jnet_0              : ------------------------------------------------------------------------ : Jnet_0
Jnet Rel            : 9758999999999999999999999999999999999999999999999999999999999987449 : Jnet Rel
```

Figure 3.2: *Homo sapiens* myosin-10 SAH is predicted to form a continuous alpha-helix. Raw output from Jpred4 [37] server suggests that the myosin-10 SAH domain forms a stable helical domain throughout the majority of the peptide. This is predicted by the high helical prediction scores with the combination of the low scores for coiled-coil formation. All three jnet prediction methods strongly predict the formation of an alpha helix in this protein sequence. Prediction of a coiled coil diminishes when the scan window size decreases, demonstrating how the heptad repeat of SAH domains can interfere with the detection of single-alpha helix structures in structural prediction tools. The higher amino acid burial prediction scores result from the presence of hydrophobic residues in the second half of the SAH domain.
The following abbreviations are used by the software:
Jnet = Final secondary structure prediction for query
jhmm = Jnet hidden Markov model profile prediction
jpssm = Jnet PSIBLAST position-specific scoring matrix
Lupas = Lupas coiled-coil prediction (with window sizes 14, 21, and 28 aa)
c = 50 – 90% probability to form coiled coil
C = greater than 90% probability of coiled-coil formation
Jnet_# = Jnet prediction of burial, less than #% solve exposure
Jney Rel = Jnet reliability of prediction accuracy. Bigger number correlates to more accurate predictions.

the two domains. CD was also performed to measure the alpha-helical content of these protein constructs to determine the helical percentage and predict any potential disruption locations in the alpha helix of the SAH domain. These experiments concluded that the entirety of the SAH domain and SAH coiled coil tandem constructs have regions of flexibility, likely introduced by the SAH region with non-charged residues present.

3.2 Results

3.2.1 The SAH domain forms a partial alpha-helix

Initial secondary structure performed by Jpred, version 4, was used to estimate the helical content of the SAH domains (Figure 3.2) [37]. This structural prediction tool estimates that the majority of the SAH domain contains an alpha-helix, but not a coiled coil. The regions not predicted to form a stable alpha-helix are the terminal regions, namely the N- and C-termini. Jpred also predicts the formation of a relatively stable helix throughout the tandem of the SAH and coiled-coil (SAH–CC) protein sequence, with very few potential interruptions in the helix (Figure 3.3). Interestingly, the algorithms used by Jpred detect a coiled coil in at least part of the M10CC sequence in all three tested sequence windows, with the 21 amino acid window confidently predicting the formation of a coiled coil in the entirety of the coiled-coil sequence. This suggests that the myosin-10 SAH and coiled-coil domains could have different dimerization abilities, but the SAH could assist in orienting myosin-10's motor feet to point in opposite directions and enhance proposed bundle-selectivity motility models [109, 123]. Therefore, more information regarding the SAH domain structure in the context of the myosin-10 is needed to better predict structures for this domain.

Circular dichroism melting experiments were performed on *Bos taurus* and *Homo sapiens* SAH domains to observe the helical content of the SAH domain as function of temperature. The helical percentage for n number of residues can be calculated using equations 3.1 and 3.2 [80].

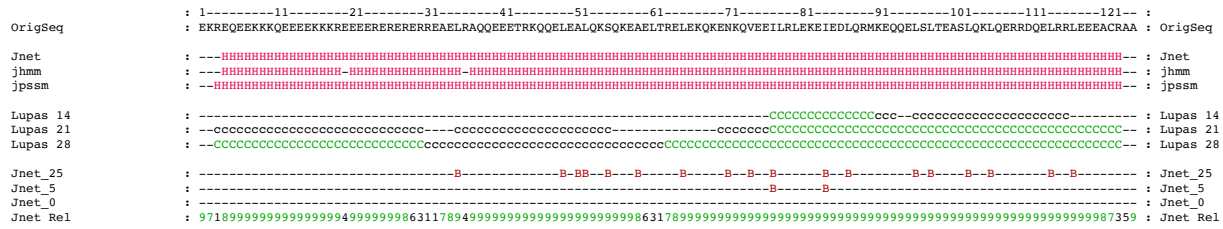

```
            : 1---------11--------21--------31--------41--------51--------61--------71--------81--------91--------101-------111-------121-- :
OrigSeq     : EKREQEEKKKQEEEEKKKREEEERERERERREAELRAQQEEETRKQQELEALQKSQKEAELTRELEKQKENKQVEEILRLEKEIEDLQRMKEQQELSLTEASLQKLQERRDQELRRLEEEACRAA : OrigSeq

Jnet        : ---HHHHHHHHHHHHHHHHHHHHHHHHHHHHHHHHHHHHHHHHHHHHHHHHHHHHHHHHHHHHHHHHHHHHHHHHHHHHHHHHHHHHHHHHHHHHHHHHHHHHHHHHHHHHHHHHHHHHH-- : Jnet
jhmm        : ---HHHHHHHHHHHHHHHH-HHHHHHHHHHHHHHH-HHHHHHHHHHHHHHHHHHHHHHHHHHHHHHHHHHHHHHHHHHHHHHHHHHHHHHHHHHHHHHHHHHHHHHHHHHHHHHHHHHHHHHH-- : jhmm
jpssm       : --HHHHHHHHHHHHHHHHHHHHHHHHHHHHHHHHHHHHHHHHHHHHHHHHHHHHHHHHHHHHHHHHHHHHHHHHHHHHHHHHHHHHHHHHHHHHHHHHHHHHHHHHHHHHHHHHHHHHHHHHH-- : jpssm

Lupas 14    : ----------------------------------------------------------------------------CCCCCCCCCCCCCCccc--ccccccccccccccccccccc--------- : Lupas 14
Lupas 21    : --cccccccccccccccccccccccccccc----ccccccccccccccccccccc--------------cccccccCCCCCCCCCCCCCCCCCCCCCCCCCCCCCCCCCCCCCCCCCCCCCC-- : Lupas 21
Lupas 28    : --CCCCCCCCCCCCCCCCCCCCCCCCCCCCccccccccccccccccccccccccccccccccCCCCCCCCCCCCCCCCCCCCCCCCCCCCCCCCCCCCCCCCCCCCCCCCCCCCCCCCCCCCC-- : Lupas 28

Jnet_25     : ----------------------------------B-------------B-BB--B---B-----B-----B--B--B------B--B--------B-B----B--B-------B--B-------- : Jnet_25
Jnet_5      : ----------------------------------------------------------------------------B------B----------------------------------------- : Jnet_5
Jnet_0      : ----------------------------------------------------------------------------------------------------------------------------- : Jnet_0
Jnet Rel    : 97189999999999999994999999986311789499999999999999999999999986317899999999999999999999999999999999999999999999999999999999987359 : Jnet Rel
```

Figure 3.3: *Homo sapiens* myosin-10 SAH–CC is predicted to be a relatively uninterrupted alpha helix. Raw output from Jpred4 [37] server for the SAH–CC tandem suggests that these domains form a relatively stable continuous helix, despite the propensity for one portion of the helix to form a single alpha-helix and the other portion to dimerize as a coiled coil. The coiled-coil prediction scores vary based on the sequence window used, with all windows confidently predicting coiled-coil formation in at least part of the M10CC sequence.
The following abbreviations are used by the software:
Jnet = Final secondary structure prediction for query
jhmm = Jnet hidden Markov model profile prediction
jpssm = Jnet PSIBLAST position-specific scoring matrix
Lupas = Lupas coiled-coil prediction (with window sizes 14, 21, and 28 aa)
  c = 50 – 90% probability to form coiled coil
  C = greater than 90% probability of coiled-coil formation
Jnet_# = Jnet prediction of burial, less than #% solve exposure
Jney Rel = Jnet reliability of prediction accuracy. Bigger number correlates to more accurate predictions.

$$\text{Helical Percentage} = \left(\frac{[\theta_{obs}]}{[\theta_{pred}]}\right) \times 100 \tag{3.1}$$

$$[\theta_{pred}] = 4.0 \times 10^4 \times \left(1 - \frac{4.6}{n}\right) \tag{3.2}$$

The helical percentage for *Bos taurus* SAH at 20 °C is calculated to be 34 % helical, and that of *Homo sapiens* SAH is 35 % helical. However, the shape of CD data collected at 20 °C strongly suggests that alpha-helices are the major secondary structure present for these constructs (Figure 3.4). Thermal melts were performed on both of the full-length SAH domains to confirm the absence of cooperative folding in the protein (Figure 3.5). Both constructs demonstrated non-coperative folding more closely associated with helical fraying. The non-cooperative folding and surprisingly low helical content both match information collected previously on the charged portion of the SAH domain [82].

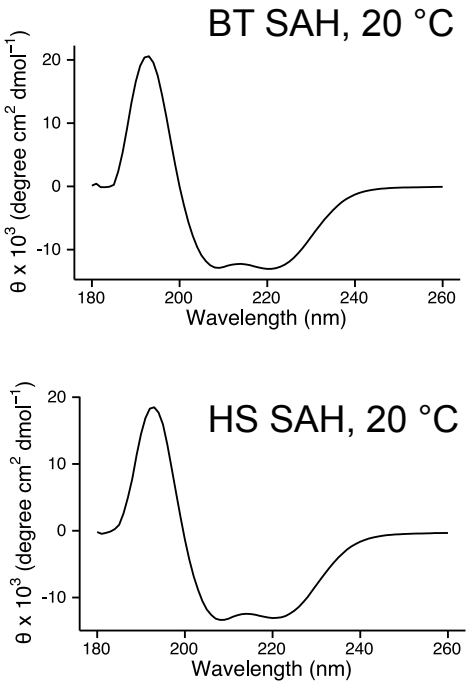

Figure 3.4: SAH domains have an overall alpha-helical structure at 20 °C. CD data at 20 °C for *Bos taurus* (upper) and *Homo sapiens* SAH domains have two CD minima at 222 nm and 210 nm. These peaks and the overall shape of the CD spectra support the conclusion that both of these domains are alpha-helical overall, even if the helical percentages for both constructs are 34–35 %.

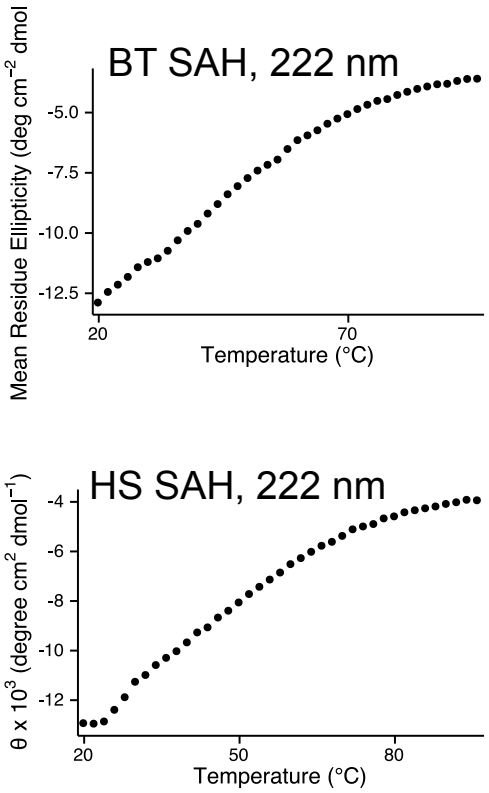

Figure 3.5: SAH domains unfold noncooperatively with increasing temperatures. CD data at 222 nm for *Bos taurus* (upper) and *Homo sapiens* SAH domains have a non-sigmoidal melting curve with increasing temperature. The sigmoidal shape is associated with cooperative protein unfolding typical of single, stably folded protein domains. The non sigmoidal shape for both SAH domains is suggestive of helical fraying in the portions of the domains that do form alpha-helices. Contrast this shape with M10CC$^{\text{short}}$-GCN4, which is a single coiled-coil domain that cooperatively melts.

However since CD is highly sensitive to concentration issues, the calculation was adjusted to assume 100 % helical content of the SAH. Our predicted helical content is off by a factor of 2.93 from 100 %. If our concentration is incorrect in these measurements, we predict that the concentration of the measured sample is approximately 13.7 μM. While significant, this concentration error is possible in explaining the surprisingly low helical content for the SAH domains measured in this study and could be addressed by repeating the protein sample preparation and CD measurements.

To get a better idea of the dynamic flexibility observed in this system, solution small-angle X-ray scattering (SAXS) was performed on the SAH domains. For a comparison,

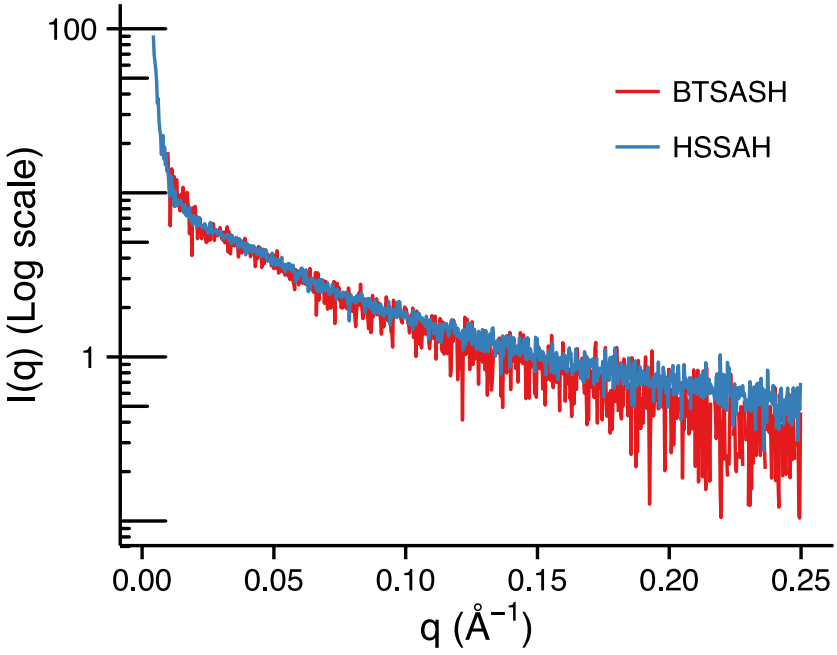

Figure 3.6: SAXS data on two SAH domains show structural similarity. Averaged, buffer subtracted, and scaled SAXS data for the *Bos taurus* SAH (red) and *Homo sapiens* SAH domains. Both datasets collected on the SAH domains overlap very well between the two curves, especially at low scattering angles. Low scattering angles in reciprocal space provide an easy comparison of shapes between different protein samples [83].

data were collected on SAH domains from *Homo sapiens* and *Bos taurus* myosin-10. The SAXS curve for these two constructs overlap very closely with each other (Figure 3.6). This overlap indicates that both of the SAH constructs are in similar conformations or contain similar degrees of flexibility. Structural similarity between the two species' SAH domains is unsurprising, since these two sequences share a 92 % similarity.

DAMMIF calculations performed on both constructs estimate the molecular weight of both SAH domains to be in the average range of 8–9 kDa, which is within estimable range of 9.02 kDa and 9.07 kDa for *Homo sapiens* and *Bos taurus* SAH, respectively. DAMAVER envelopes for both constructs were generated using Autognom to generate an automatic P(r) curve at the BioCAT beamline (Figures 3.7–3.8). Both dummy atom model calculations produced an extended rod conformation with an end-to-end distance measurement of 101

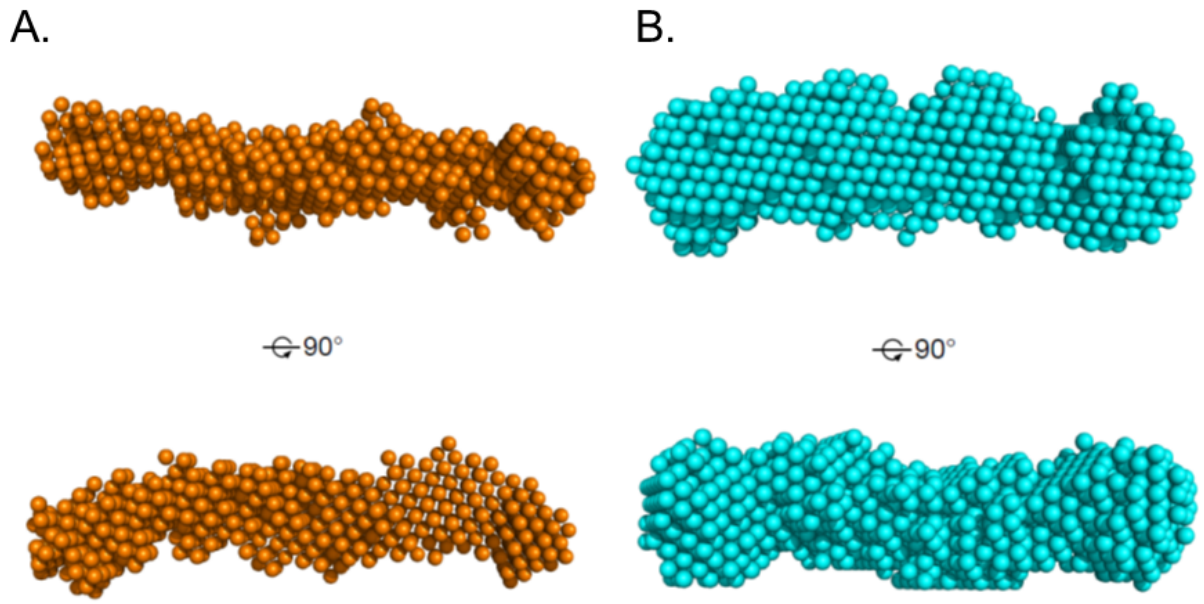

Figure 3.7: Dummy atom models of SAH domains form extended rods A. Two views of the dummy atom model of *Homo sapiens* SAH suggest some flexibility or motion within the SAH domain, also supported by the maximum end-to-end distance measurement of 111.7 Å for this 74 residue peptide. B. Two views of the dummy atom model of *Bos taurus* SAH suggest some flexibility or motion within the SAH domain, also supported by the maximum end-to-end distance measurement of 101 Å for this 75 amino acid peptide. These models were generated using DAMMIF and DAMAVER dummy atom calculation tools with input data output from Autognom at BioCAT beamline [41, 42]. This calculated D_{max} of 103.53 Å.

Å for *Bos taurus* SAH and 117.8 Å for *Homo sapiens* SAH. This distance roughly matches the predicted length of these alpha helices, although the structure distance is a little longer for the *Homo sapiens* SAH than the approximately 105–110 Å expected for this single alpha helix.

3.2.2 Myosin-10's SAH domain enhances the antiparallel orientation of the coiled coil

Now that the orientation of the bundle selective M10short-GCN4 has been determined to also be anti-parallel, the role of the SAH domain can be determined. Constructs containing the SAH and coiled-coil domains of M10short-GCN4, the post-SAH swivel motor (Figure

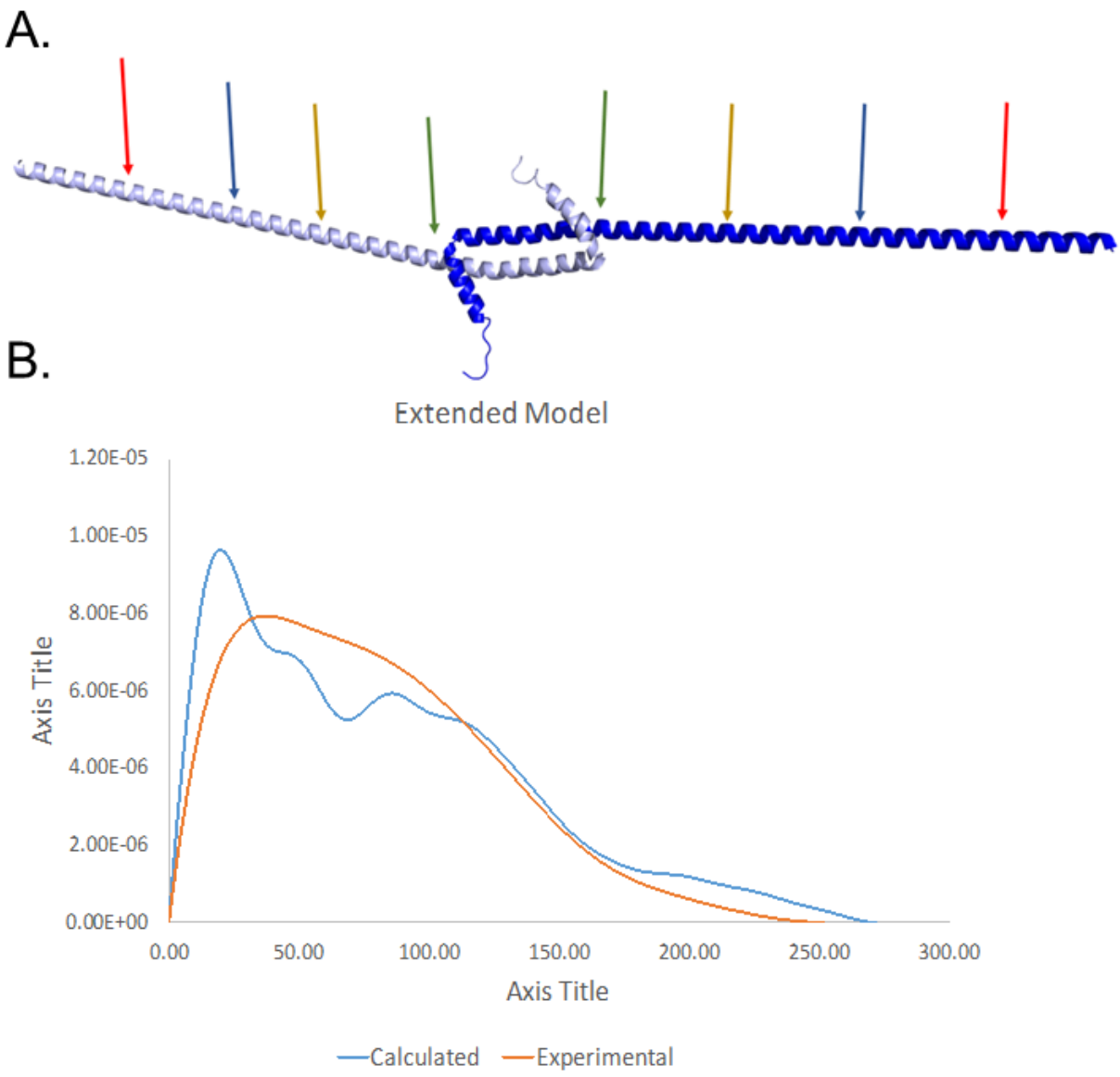

Figure 3.8: Model of extended SAH–CC tandem. (A) The model of *Homo sapiens* extended SAH–CC structure used in SAXS analaysis. Colored arrows indicate locations where flexiblity was introduced in different models at approximately residue 20, 40, 60 or 80 on both chains of the tandem. (B) Pairwise distance distribution comparison between experimental data (red) and data calculated from the extended structure in (A). Data prediction was performed using Crysol and Gnom, and the P(r) fit with the best quality score with a Dmax close to the measured maximal distance from the structure was selected.

3.1), and wild-type *Homo sapiens* myosin-10 were created. These constructs are referred to as SAH–CC tandems, since all three constructs start at the SAH domain and end at the terminus of the defined coiled coil. Small-angle X-ray scattering was performed on all three constructs to measure potential flexibility of the SAH domain and distances that the SAH domain spans from the coiled coil.

Analysis of this data was more difficult than initially expected due to the extended conformation of these residues and possible flexibility of the SAH–CC construct. A starting structure with the SAH domain extending from the myosin-10 coiled coil was created (Figure 3.8A). This model assumed that the SAH domain forms a rigid and complete alpha-helix over the 75 residues leading into the coiled coil. Using this model, predicted SAXS data was generated using Crysol [144], which predicts scattering patterns from high-resolution PDB files. Distance distributions generated from the experimental data and predicted data were generated using gnom [119]. A comparison between these two curves suggests that the SAH–CC construct is likely not in a fully extended conformation, suggesting that some flexibility along the SAH domain could exist.

To explore this possibility, flexibility was introduced along the SAH region of the SAH–CC tandem. Flexibility at specific residue locations in our construct were introduced around residue 20, 40, 60, or 80, considering that our specific construct also has residues present from the thrombin cleavage tag. The location of these sites are indicated by the sets of colored arrows in Figure 3.8A. Flexibility was controlled by altering the psi and phi backbone angle values at the specific residue. For each residue, a set of eight structures were generated for comparison. A sample structure with the flexibility introduced at residue 20 is illustrated in Figure 3.9A.

Pairwise distance distributions were generated for each of the models as described above. While none of the models produced a predicted distance distribution matching the experimental distance distribution, there were significant differences between the sets of distance distributions. Figure 3.9B–E contain the predicted distance distributions for the different

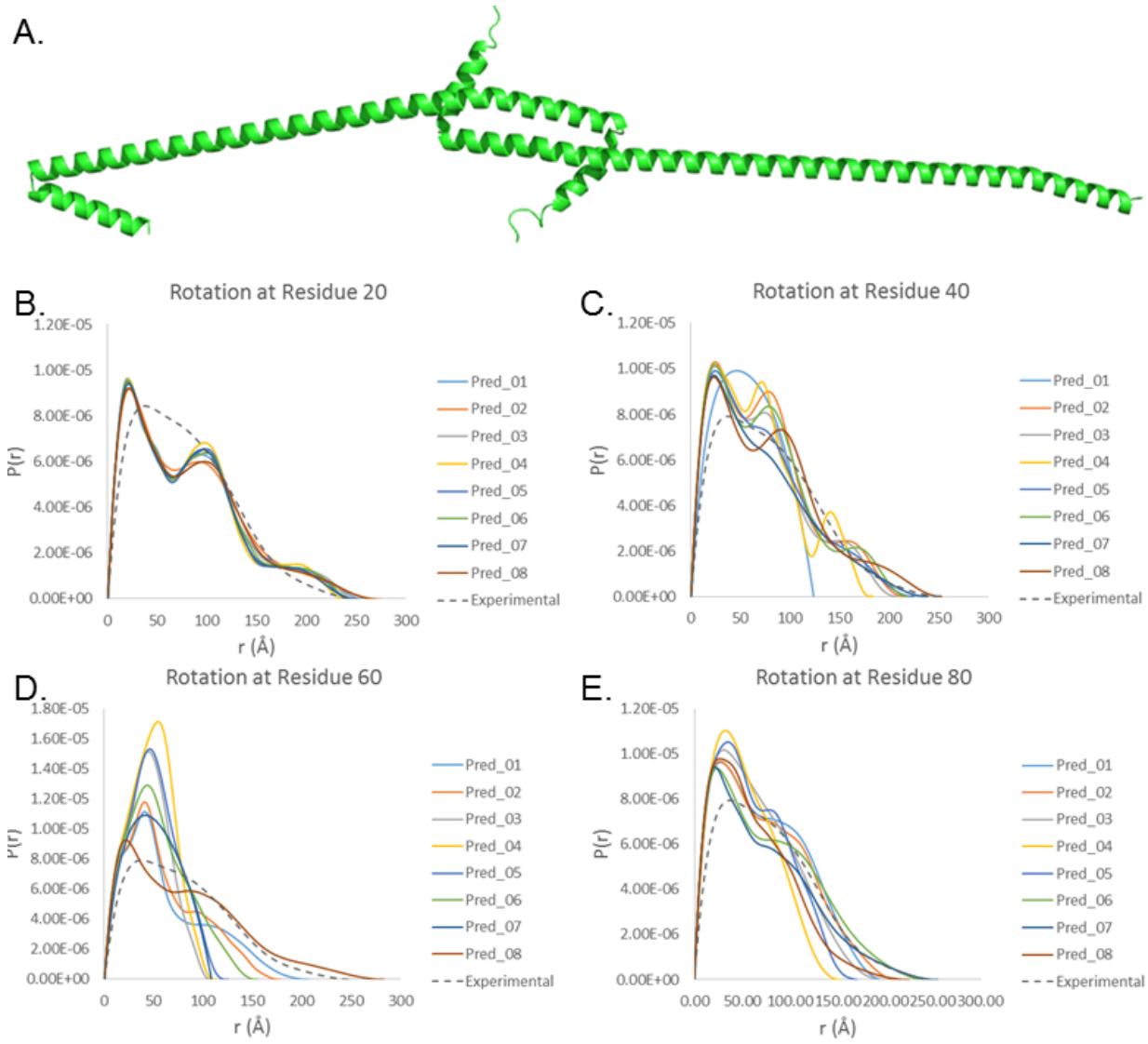

Figure 3.9: Rotation introduced at specific SAH–CC residues provides different distance distributions. (A) Sample SAH–CC input structure with flexibility introduced at residue 20 of the construct. Compare to the starting structure in figure 3.8A. (B–E) Distance distributions generated for structures with flexibility introduced at specific residue positions. From the starting structure (Figure 3.8A), flexibility was introduced at residue position (B) 20, (C) 40, (D) 60, and (E) 80 for calculations. For each position, eight structures were randomly generated and distance distributions were generated as described in Figure 3.8B.

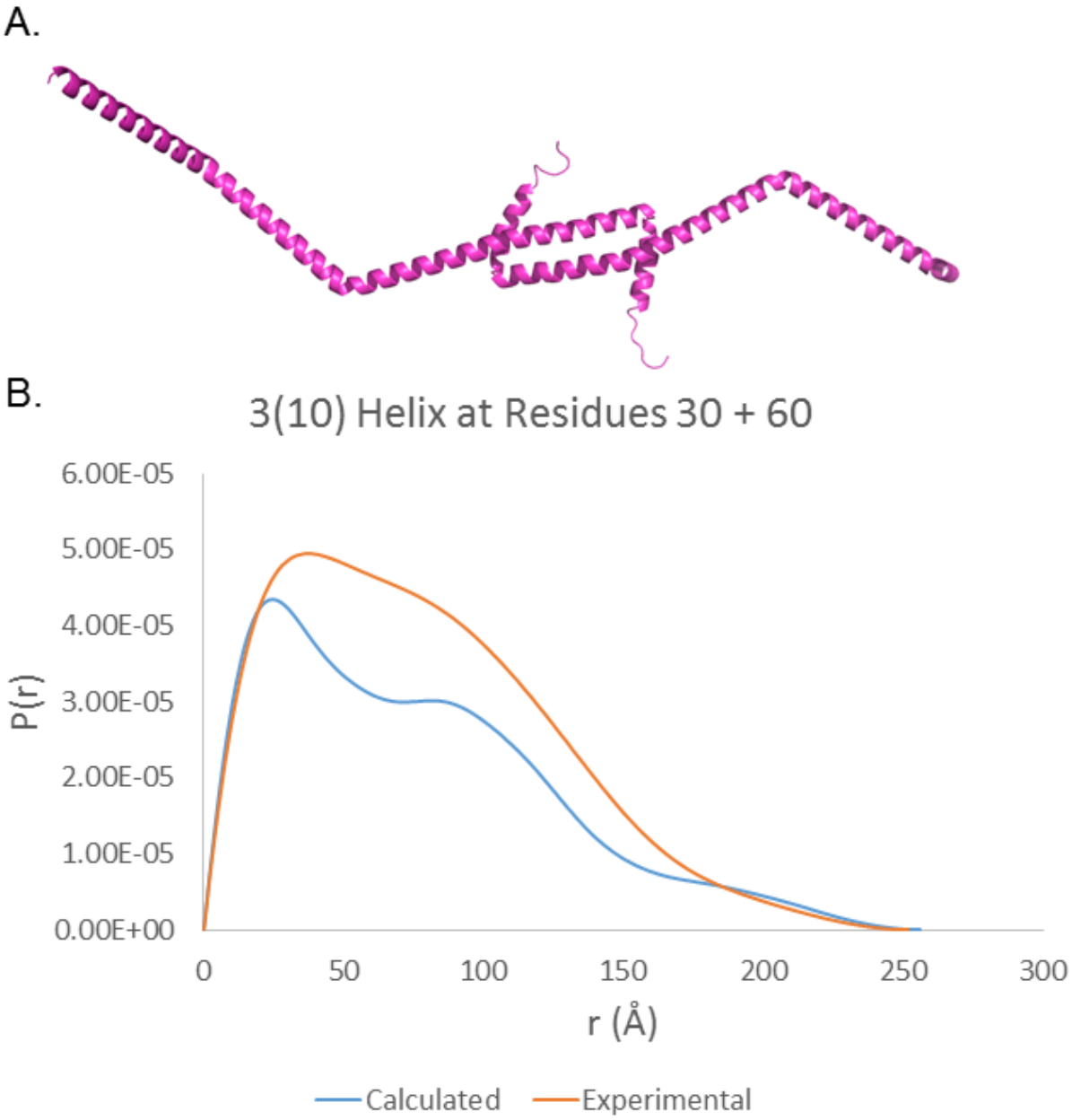

Figure 3.10: SAH–CC tandem could contain 3_{10} helix. (A) SAH–CC tandem using residues with 3_{10} helix backbone angles at residue positions 30 and 60 from the starting structure. This depiction suggests that the some of the unstructured residues could be in this conformation. (B) Distance distribution comparing experimental data with predicted data from the structure in A. The distance distributions were calculated as described in Figure 3.8B. This comparison suggests that the flexible regions of the SAH–CC tandem could be in a 3_{10} conformation, rather than forming a completely unfolded structure.

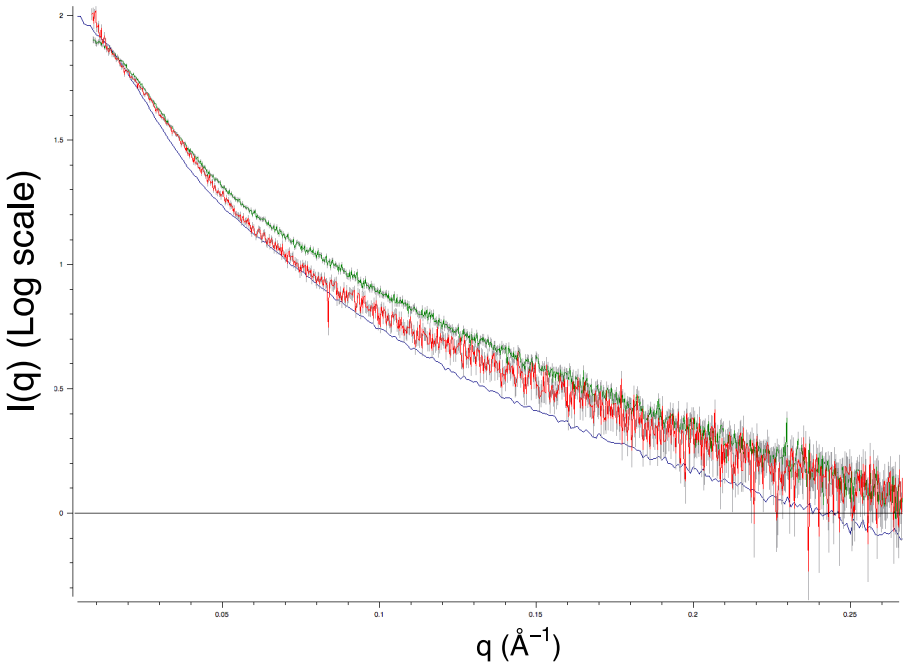

Figure 3.11: SAXS data between three SAH–CC domains differs. Averaged, buffer subtracted, and scaled SAXS data for the SAH–CC domains from *Homo sapiens* wild-type (blue), M10short-GCN4 (green), and the swivel (red) constructs. The observed signal differences between the three constructs could be attributed to differences in flexibility or coiled-coil distances, the latter of which is likely when comparing the SAH–CC from wild-type myosin-10 and M10short-GCN4. Figure currently prepared from primus from the ATSAS suite [119].

sets of models and compare to the distance distribution from the experimental data. Rotation of the psi and phi angles at residue 20 in our construct produced models that had P(r) distributions that diverged the greatest from the experimental data, while rotation of the psi and phi angles at residue 80 produced distributions that matched the best to the experimental data out of this set of models. However, none of the models generated by direct rotation of backbone angles associated at these specific resiudes produced a distance distribution matching the experimental data.

We attempted to address this issue by directing the backbone angles to match specific phi and psi angles associated with various peptide conformations, rather than randomizing the backbone angle values. One such conformation that we introduced by directing the backbone angles is known as the 3_{10} helix. This secondary structure is an intermediate structure between a structured and unstructured alpha helix [152]. 3_{10} backbone angles were introduced at two points from the starting structure to produce a model illustrated in Figure 3.10A. Comparing the distance distribution calculated from this model to the experimental distance distribution show a similar spread of the population of atoms, but there are still differences. However, this result suggests that future analyses described below could provide a better understanding of the structure of the SAH–CC measured in our system.

3.3 Discussion

Typical observations of a CD melting experiment would show a sigmoidal curve with a single inflection point, which would be the T_m, or the melting point of the protein where 50% of the protein would be structured while the other 50% would be unstructured. This behavior is known as a cooperative melting atypical to helical domains. During an unfolding experiment with a helix, the structure unfrays at the ends like a rope. The helical unfraying produces a linear curve of CD signal vs. temperature, which supporting the predicted alpha-helical SAH structure previously reported for part of this domain [82] and predicted by structure prediction tools. Previous CD measurements on the region of the SAH domain enriched

with charged residues estimated an alpha-helical percentage of 75 %, which is higher than the full length measurements performed [82]. Our low amount of predicted helical content is surprising, based on the structural prediction software and an unpublished crystal structure of the myosin-10 SAH–CC tandem, which showed the SAH containing a high percentage of alpha-helical secondary structure throughout the protein. Since the charged region is about half of the SAH domain, this suggests that the rest of the myosin-10 SAH domain does not have a measurable secondary structure.

However CD alone does not address the ability of previous experiments to measure a diminished bundle selectivity with the introduction of flexibility before and after the SAH [109]. In fact, the CD data is somewhat inconsistent with the SAXS data and structural calculation performed on the preliminary DAMMIF structures (Figures 3.7). These two structures are rod-like, which is suggestive that the alpha-helical content may be higher than predicted from the CD data. A potential cause of the low helical content could be due to the high protein concentration sensitivity associated with the calculations currently used above. We are assessing options and techniques to more accurately determine the protein concentrations used in our CD experiments, since these constructs do not contain any aromatic rings [49].

The DAMMIF dummy atom models for these structures additionally support our belief that there is some flexibility in the myosin-10 SAH domains, since the rods of these proteins contain a few bulkier and thinner areas. This could also be artifacts from the data modeling, so we will address these concerns by first creating more DAMMIF models and changing the D_{max} input values for the calculations to see how significantly the shapes of these molecules change. We also propose using a different SAXS analysis suite, called SASSIE, to assess the flexibility of the SAH domain and the SAH–CC tandem domains. SASSIE allows for simple and complex Monte Carlo simulations to create numerous structural models that then produce theoretically SAXS curves that can be compared to the experimental data. The advantage of this software is that the flexible regions are easier to assign in the Monte

Carlo simulations, and the cut off for the experimental fit can be controlled at each step in the process [29]. Right now we are experimenting with different starting structures and trying to find the most optimal ones that would help sample a broad variety of potential structures for both the SAH and SAH–CC domains.

Above we introduced two different methods to generate sets of structure models that could be used to predict the conformation or set of conformations of the SAH–CC tandem. To direct our initial analysis, we introduced flexibility at specific residues of the starting structure in Figure 3.7A by rotating the phi and psi backbone angles. The first attempt introduced flexibility by rotating the angles of only one residue per subunit to random values. This produced the results seen in Figure 3.9. None of the 32 generated structures produced a distance distribution that matched the distance distribution associated with the experimental data.

This led us to perform a second type of analysis that also altered the backbone phi and psi angles from the starting structure in Figure 3.8A, but backbone angles were altered to match values associated with 3_{10} helices. One such model, represented in Figure 3.10, was used to calculate a distance distribution. A comparison of the distance distribution plots in Figure 3.10B indicates that this fit still is not perfect, but the maximum distance and shape of the plots could indicate that adding in additional points of flexibility and biasing the backbone towards certain dynamic and unstructured values could be an appropriate next step.

Therefore we are currently utilizing two methods to produce a library of structures based on modifications performed on the starting structure (Figure 3.8A). The first method will use SASSIE, a SAXS program utilizing a Monte Carlo algorithm to introduce flexibility at user selection regions of the protein and generate scattering curves [29]. We are using SASSIE to create a library of 20,000+ structures to have different structures to determine how varying the flexible region in the SAH–CC can change the distance distribution. One drawback to this method is that complete flexibility is introduced in these regions, so there is no chance

to bias the structure for a more flexible alpha helix, such as the 3_{10} helix or other structures.

To address this specific issue, we are also developing a method to alter the backbone angles to values that match other secondary structures that could be associated with varying degrees of flexibility. This is based on the preliminary experiment using the 3_{10} helix, shown in Figure 3.9. While we wish to increase the number of residues in the 3_{10} conformation, we also hope to introduce values associated with unstructured proteins such as Polyproline-II (PPII) helix. This is one secondary structure that is associated with disordered proteins [1], so introducing this secondary structure in specific locations of the SAH–CC construct could provide us with models that closely match the structure of the molecule measured by SAXS.

While computational methods are still being developed to successfully analyze the SAH–CC tandem, we also could propose that our specific experiment could have measured a structure that is not present in myosin-10 while in motion. When myosin-10 is walking along actin bundles, the motor feet are experiencing and creating small forces thought to help gate the individual motor feet to successfully control a processive walk [76]. In our experiments, we did not have any force present at the N-terminal ends of the SAH domains, which could have allowed the SAH to find conformations not present during a successful processive myosin-10 walk. The goal of this study is to determine how myosin-10's SAH and coiled-coil domains form a continuous structure to help connect the motor feet to the coiled coil, since the coiled-coil orientation and stability is important for myosin-10's bundle selectivity [96, 108, 109, 123, 159]. We are hoping to address some of the potential flexibility of these constructs by SAXS, although the extended rod-like shape has made this more difficult than initially thought.

3.4 Material and methods

3.4.1 Vector design and cloning

SAH–CC domains for structural studies were cloned using *Homo sapiens* and *Bos taurus* constructs in pBiEx3BS vectors as the PCR template to create inserts [108, 97]. PCR amplification was peformed using Pfu Turbo polymerase (Agilent). pET-15b (Novagen) was linearized using BamHI-HF (New England Biolabs), and a standard SLiCE cloning reaction was performed [177].

3.4.2 Protein expression

SAH–CC constructs were purified as previously defined [159]. Briefly, transformed BL21(DE3) pLysS were grown in terrific broth and induced for overnight expression. Cells were lysed in a high-salt buffer (50 mM HEPES, 500mM NaCl, 10 mM imidazole, 5% w/v glycerol, 5 mM BME, pH = 7.5) using microfluidization. The lysate was centrifuged and filtered before application to a 30 mL Ni-NTA Superflow (Clonetech) column. The column was washed with 5 column volumes of wash buffer (lysis buffer with 20 mM imidazole), followed by 5 column volumes of second wash buffer (lysis buffer with 50 mM imidazole). The protein was eluted with 6 column volumes of elution buffer (lysis buffer with 250 mM imidazole), and protein fractions were pooled and concentrated using Amicon Ultra Ultracel-3 filtration devices (EMD Millipore). Humanα-thrombin was used to cleave the 6xHis-tag by incabating at room temperature for 4.5 hours before the reaction was quenched with PMSF. Cleaved protein was separated from uncleaved protein and the 6xHis tag by passing over Ni-NTA and collecting the flowthrough. The samples were pooled and concentrated with an Amicon Ultra Ultracel-3 filtration device and subsequently purified by gel-filtration chromatography on a Superdex 75 30/100 GL column previously calibrated with a reference set of protein markers (Sigma MWGF70).

Motor constructs were purified from SF9 cells 48 hours after baculovirus transfection.

Cells were lysed in a FLAG lysis buffer (200 mM NaCl, 4 mM $MgCl_2$, 20 mM Imidazole, 0.5 mM EDTA, 1 mM EGTA, 0.5% v/v Igepal, 7% w/v sucrose, 1 mM PMSF, 10 µg/mL aprotinin, 10 µg/mL leupeptin, 0.5 mM DTT, and 2 mM ATP at pH 7.5) using douncing followed by a freeze-thaw cycle. The lysate was clarified using centrifugation and then batch bound to anti-FLAG M2 affinity resin (Sigma A2220). The protein bound to the resin was settled using gravity, and resuspended using gentle nutation during the batch binding, washes, and elution steps. Wash buffer (150 mM KCl, 20 mM Imidazole, 5 mM $MgCl_2$, 0.5 mM DTT, 1 mM EDTA, 1 mM EGTA, and 3 mM ATP, pH = 7.5) was used in three washes before elution (wash buffer with 0.2 mg/mL FLAG peptide).

3.4.3 Circular Dichroism

A Jasco J-1500 spectropolarimeter (Jasco) was used for all CD spectra and melting curves. CD spectra were collected from 20 °C to 98 °C back to 20 °C with 2 °C increments, 3 spectra per temperature point, 1 nm bandwidth. Samples equilibrated for 2 minutes after temperature equilibration for each temperature point. Each spectrum was measured from 260 nm to 180 nm, and the melting temperature was analyzed at 222 nm using SigmaPlot 12.0 (Sigmaplot) to produce a sigmoidal fit replotted using ggplot2 [169].

3.4.4 Small-angle X-ray scattering

Samples were purified using a 50 mM Tris-HCl and 100 mM KCl, pH 7.5, buffer for the size exclusion step. The samples were then dialyzed into a buffer containing 5% v/v glycerol. X-ray scattering data as a function of momemtum transfer were collected on beamline 18ID at the Advanced Photon Source, Argonne National Laboratory in an Size-Exclusion Chromatography-SAXS (SEC-SAXS) setup [88]. The gel filtration column used to purify proteins was equilibrated to room temperature and the sample buffer before samples were loaded and passed through the column. Due to the low UV-Vis absorption of these samples, the X-ray data was collected in a 4-5 mL window around where the protein was expected to

come off based on the chromatograms collected during purification.

SEC-SAXS data were buffer subtracted, scaled to match I(0), and averaged using the ATSAS software suite [119]. Initial dummy atom models were generated using DAMMIF [41]. Further SAXS analysis are structure generation are being performed on the SASSIE-web server, which is an online version of SASSIE previously described [29]. These generated structures are then used as input into Crysol to calculate a predicted experimental scattering curve [144]. This information can then be analyzed using tools present in the ATSAS suite [119]. Additional analysis methods are being developed using Python to generate structures favoring backbone angles from specific secondary structures.

CHAPTER 4

DISCUSSION AND FUTURE DIRECTIONS

4.1 Introduction

Myosins are actin cytoskeleton-based motor proteins grouped into numerous classes based on the amino sequence of the protein to make up a superfamily [107, 112].

4.2 Overview of myosin-10 domains

4.2.1 Motor feet are the site of ATP hydrolysis and actin binding

Each myosin-10 monomer is comprised of a motor foot, leg domains, and tail domains (Figure 4.1) [76]. Like many myosin motors, myosin-10 has calmodulin-binding domains and cargo binding domains [24]. However, there are minor differences in the structures and sequences for the myosin-10 domains that help influence its motility to favor motility in filopodia and cargo targeting behavior. Some details of these domains are described below to better explain the roles these domains play in myosin-10's cellular navigation.

Myosin motor feet, also known as motor heads, contain highly conserved ATP catalytic and actin-binding sites. All members of the myosin superfamily have the motor domain located close to the N-terminus [105, 122]. This domain in the source of the motility and mechanosensing properties of myosins. As a mechanoenzyme, the motor domain converts chemical energy from ATP into directed and regulated movement that allows for cellular contraction or myosin motility inside the cell [122]. The coordination between ATP hydrolysis and myosin motility is similar across all superfamily members [33]. The binding of ATP to the motor foot lowers the motor affinity for actin [39, 98], and causes the motor foot to lift up from the actin. Hydrolysis of ATP reorients the motor head and prepares the motor head to rebind the actin. However, the motor remains in a weakly associated state with the actin track until phosphate release. At this point, the motor head switches to a strongly-

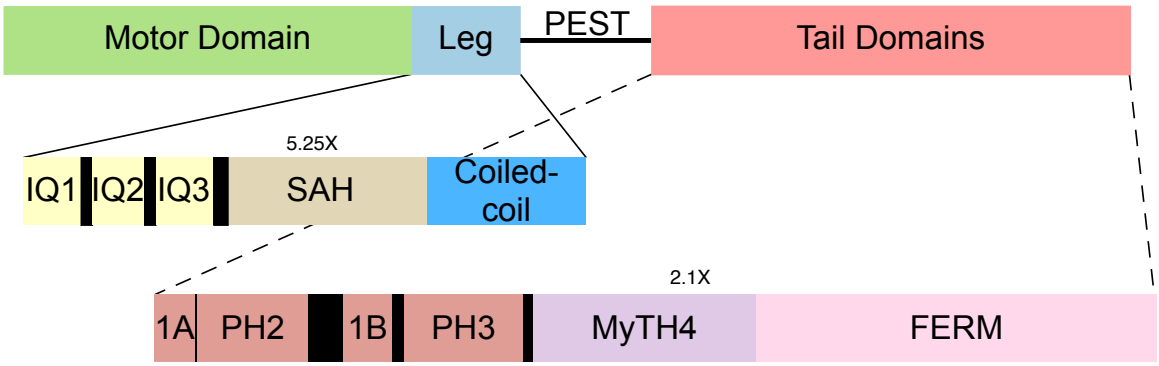

Figure 4.1: Myosin-10 construct map shows that the motor feet and the tail domains are large domains. To-ratio *Homo sapiens* myosin-10 domain map illustrating the relative sizes of the domains in the myosin superfamily motor. The motor domain is 742 amino acids, the leg domains are 176 amino acids, the PEST region is 238 amino acids, and the tail domains are 871 amino acids long. The leg and tail domains are enlarged below the full-length construct map, with the scaling factors listed above the middle of each domain. Black vertical lines indicate short linker regions between domains. Note that the PH1 domain is split by PH2, but in the structure of the two PH domains, PH1 and PH2 both form two Pleckstrin homology domains [97].

associating actin state through ADP release and ATP rebinding before repeating the cycle again. Two-headed myosin motors with high processivities have high duty ratios, which is defined as the time the myosin heads remain in the strongly-bound actin site [32, 31].

The duty ratio of the myosin-10 motor was measured to be greater than 50 % of the ATPase cycle of the motor, which indicates that myosin-10 is a high duty-ratio motor. Since a high duty ratio is a requirement for myosin processivity, the minimal unit for myosin-10 processive motion can be a functional dimer [66]. Myosin-10's motor domain holds a 35% and 45% sequence similarity to the motor domains of conventional skeletal muscle myosin (myosin-II) and myosin-VIIa, respectively [14]. A single myosin head, S1, is capable of generating force independently in the presence of an actin filament and ATP [104, 154].

4.2.2 The leg domains: IQs, Single-alpha helices (SAH), and the Coiled-coil

Bridging the motor domain with the cargo-binding domains are the leg domains, which consist of three IQ domains, a single-alpha helix (SAH) and an anti-parallel coiled-coil. The IQ domains are the sites of calmodulin binding, which allows for potential calcium regulation of myosin-10. Each IQ domain is approximately 19-24 amino acids long and binds one calmodulin, leading a dimer of myosin-10 to bind 6 calmodulins total. Following the IQ domains is a single-alpha helix domain. This is a specialized alpha helix domain that contains positively- and negatively-charged residues in a pattern favoring an alpha helix that does not form a coiled-coil or fold with other protein domains. The first 35 residues of the SAH domain contain a higher proportion of charged residues to hydrophobic residues compared to the next 40 residues. Despite this different amino acid composition between the two regions of the SAH domain, the entirety of the SAH domain is predicted to form a stable alpha helix.

Directly following the SAH domain is myosin-10's coiled-coil. Myosin-10 processively walks along actin tracks as a dimer, and the coiled-coil has been identified as the dimerization sequence in the protein [14]. An NMR structure for the minimal myosin-10 coiled-coil, determined to be *Homo sapiens* residues 883-934, was solved and showed that myosin-10's coiled-coil domain forms a surprising anti-parallel coiled-coil [96]. Most myosin motors have a parallel coiled-coil for the minimal oligomerization unit, so myosin-10's anti-parallel-oriented coiled-coil was surprising. Previous single molecule studies designed myosin-10 constructs under the assumption that the coiled-coil orientation was parallel, and all studies added an additional oligomerization domain to force the constructs to dimerize.

4.2.3 Tail Domains: Lipid- and cargo-binding and motor regulation

Near the C-terminus are the PH domains and the MyTH4-FERM domain, which are involved in lipid and cargo binding in the cell. Both domains have been recently implicated in the activation pathway for myosin-10, leading to many different proposals on how myosin-10 is regulated and activated when starting a processive walk [156]. The PH domains are the site of lipid binding especially PIP_3, which is associated with filopodial growth and activity [74, 78]. Inhibition of PIP_3 binding by PH domain mutation or chemical inhibition causes filopodial growth and downregulates filopodia-associated behaviors, potentially through deactivation of myosin-10 [28, 120]. The PH1 domain is split into two sections by PH2 in the protein sequence (Figure 4.1) [14]. However the structure of these two domains concluded that the PH1 and PH2 domains both form fully functional domains when properly folded [97].

C-terminal to the PH domains is the MyTH4-FERM domain. The MyTH4-FERM domain is present in myosin-7 and myosin-XVa [14, 164], and is known to be the binding location for many cargo proteins [26, 76]. Analyses of the MyTH4-FERM domain by crystallography revealed that the MyTH4-FERM domain binds DCC (deleted in colorectal cancer), one myosin-10 cargo, by an interactin in the DCC-p3 protein fragment and the FERM domain [62, 167]. The presence of one cargo may inhibit the ability for the MyTH4-FERM to bind to another cargo protein [62]. In addition to binding cargo proteins, the MyTH4-FERM domain binds to the motor foot and leads to inhibition. The addition of PIP_3 reduces the tail-based motor inhibition and allows inactive monomers to start unfolding and initiate processive walks [156]. While the PH and MyTH4-FERM domains may help activate myosin-10 and create a local concentration of motors that can form dimers, the tail domain is not required to form dimers [82, 156].

4.3 *In vitro* characterization of Myosin-10

4.3.1 Motility properties of myosin-10

Initial studies of myosin-10 used *in vivo* microscopy to measure the ability of the motor to localize in filopodial tips. Multiple studies measured myosin-10 and its cargo walking as bright spots to filopodial tips, and some dead motors moving back towards the cell with retrograde actin flow [77, 140]. Applying total internal reflection fluorescence (TIRF) microscopy to myosin-10 in cells allowed for a third, faint and faster state of myosin-10 to be visualized. This fainter state was predicted to be minimal dimers of myosin-10, with the brighter spots containing multiple clusters of myosin-10 [77]. There are currently three models of myosin-10 motion within filopodia (Figure 1.2) [77].

All models of myosin-10 motility are based on measeurements within cellular filopodia, which contain bundled actin [79]. To better understand the ability of motors to walk along tracks, the bundled actin in filopodia can be simplified to two components: actin and fascin. Fascin is required for filopodia formation to occur [71, 160]. The knocking down of fascin causes a significant decrease in filopodia extending from the cell [108]. The protein itself crosslinks actin filaments in a parallel orientation needed to form the actin structures required by filopodia [38, 147]. This is the justification for creating assays using actin-fascin bundles to act as the minimal bundle requirement for myosin-10 *in vitro* microscopy assays [108, 109, 143, 146].

4.3.2 Dimerization strategies for myosin-10 characterization

Single molecule studies were performed to better understand how myosin-10 motors can walk along the actin path and whether a single dimer or a cluster of motors is necessary for a successful processive walk [108, 109, 123, 140, 143, 151]. However myosin-10 requires the creation of truncated constructs with the cargo- and lipid-binding domains removed. Shortened myosin-10 remains monomeric at most concentrations due to the low dimerization

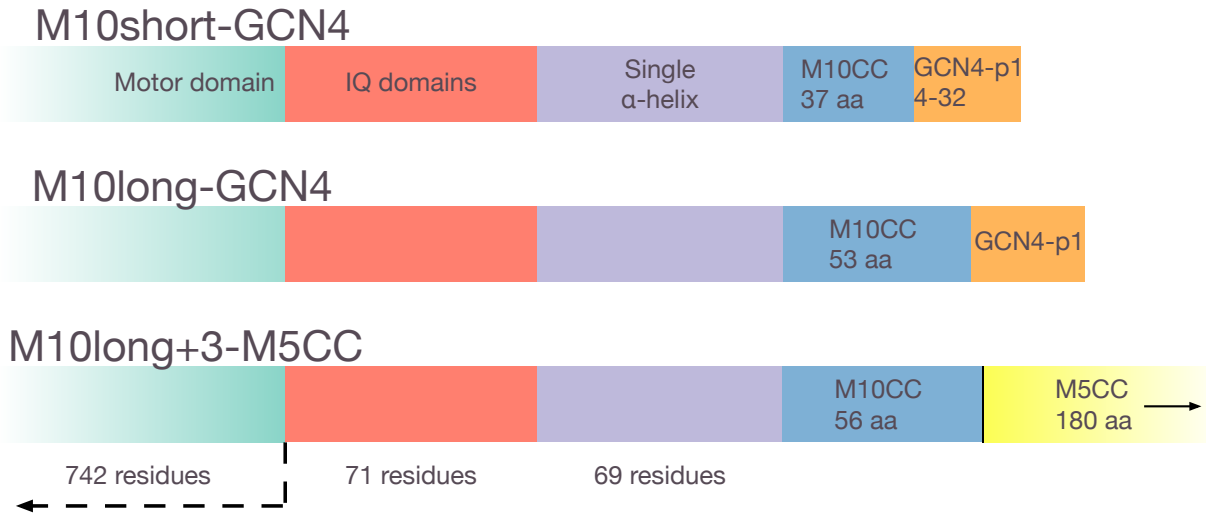

Figure 4.2: Artificial constructs were used for studying myosin-10 stepping behavior. Zoomed-in and scaled construct diagram focusing on IQ, SAH, and coiled-coil domains of each artificial construct used to characterize myosin-10 stepping behavior. Part of the motor domain (green) is shown for illustrative purposes. Differences in the constructs result from the truncation point of the myosin-10 coiled-coil (blue) and the dimerization domain used after the myosin-10 coiled-coil. GCN4-p1 [113] (orange) and myosin-5 coiled-coil (yellow) were used to force the constructs to form dimers, since myosin-10's coiled-coil has a low native dimerization affinity. Myosin-5 coiled-coil used in $M10^{long+3}$-M5CC is 180 amino acids long, most of which were omitted from this diagram for illustrative purposes.

affininity for myosin-10's coiled-coil [82, 96]. Three groups tested myosin-10 motility using artificial constructs consisting of the motor and leg domains (Figure 4.1) and either GCN4-p1, a parallel coiled-coil [113], or the coiled-coil from myosin-5, which forms a long parallel coiled-coil [155]. The three constructs used are known as M10short-GCN4, M10long0GCN4, and M10long+3-M5CC, with M10short consisting of *Bos taurus* residues 1–920 and M10long consisting of residues 1–936. Details about the different myosin-10 dimerization schemes are in the following section, and diagrammed in figure 1.4.

M10short-GCN4 showed a strong preference to initiate processive runs on bundled actin over single actin filaments [108]. Additionally this construct showed a preference to walk straight and not rotate around bundles, using sidesteps to avoid obstacles rather than as a requirement to continue walking along its track [123]. M10long+3-M5CC did not demonstrate any track selectivity between filamentous and bundled actin. This motor was able to walk along actin filaments by spiraling around the filament, potentially allowing for the selection of favorable motor head binding sites. This construct also spiraled around bundled actin during approximately 30 % of the run lengths, so this construct used sidesteps to change actin filaments often during processive runs [143]. The third construct, M10long-GCN4 demonstrated no significant bundle selectivity, and the motor was tested to produce steps on filamentous actin and bundles [146].

4.3.3 Analysis of dimerization domains

The source of the different behaviors between these motor constructs was thought to be the truncation point of the myosin-10 coiled-coil [143]. M10short-GCN4 inserted GCN4 at residue 920, or 14 amino acids short of the full coiled-coil. This is because there was a potential break in the heptad repeat after residue 920 that the insertion of GCN4-p1 prevented. M10long+3-M5CC also sought to preserve the traditional heptad repeat between the myosin-10 coiled-coil C-terminus and myosin-5's coiled-coil [143], which is why there are three extra residues. As a contrast, the heptad repeat in M10long-GCN4 restarts between

myosin-10's coiled-coil and GCN4 [146]. All three of these constructs were designed before the structure of the wild-type myosin-10 coiled-coil, which turned out to have an anti-parallel orientation. Therefore all three constructs had inadvertently fused a parallel and anti-parallel coiled-coil together.

The result of such fusions could result in numerous structural possibilities, which could explain the different motility behaviors between each construct (Figure 2.1D). We used solution structural biology techniques to determine potential structures for the coiled-coil fusions used to test all three constructs. Surprisingly, only the coiled-coil in M10short-GCN4 forms a stable and resolvable coiled-coil. The coiled-coils from M10long-GCN4 and M10long+3-M5CC were detected to have flexibility or form higher order oligomers. All these structural techniques require significantly higher concentrations than concentrations allowed for single-molecule studies, so the higher order oligomers could have been a result from this study but still strongly support a dynamic feature of the M10long-GCN4 and M10long+3-M5CC coiled-coils.

Table 4.1: Summary of artificial myosin-10 constructs and behavior noted between $M10^{short}$-GCN4, $M10^{long}$-GCN4, and M10long+3-M5CC. Information related to construct design, behavior, and relevant studies are listed under each row.

Construct Name	Myosin-10 coiled-coil residues	Dimerization Domain	Bundle Selective	Relevant Publications
$M10^{short}$-GCN4	883–920	GCN4-p1	Yes	Nagy *et al.* (2008) [108] Nagy & Rock (2010) [109] Ricca & Rock (2010) [123]
$M10^{long+3}$-M5CC	883–937	Myosin-5 coiled-coil	No	Sun *et al.* (2010) [143] Umeki *et al.* (2011) [156]
$M10^{long}$-GCN4	883–934	GCN4-p1	No	Takagi *et al.* (2014) [146]

4.4 In-depth analysis of myosin-10 stepping behavior on actin tracks

4.4.1 Bundled actin binding sites are favorable for myosin-10 processivity

Previously, myosin-10 research concluded that bundles provide accessible sets of actin binding sites, known as actin rafts for myosins at each step location (Figure 1.5) [109]. These accessible rafts occur every half-turn of the actin helix, providing a series of sites for myosin-10 to bind approximately every 18 nm, which is the step size previously measured for bundle selective myosin-10 constructs [108, 109, 123]. In contrast to the longer step size of myosin-5 and myosin-6, which at approximately 36 nm matches the pseudohelical pitch of actin, the shorter stepsize requires myosin-10 to straddle between two separate filaments in the bundle [123]. Straddling would allow myosin-10 to processively walk on actin bundles in the filopodia for large distances because the bundle requirement would allow myosin-10 to walk around any actin-bound proteins that would get in the way of active motors [97, 123]. This model proposes multiple methods that enhance myosin-10's ability to robustly move through cellular filopodia.

Additionally the chimera studies noted that myosin-5/myosin-10 based chimeras always initiated more processive runs on bundled actin when myosin-10 motor feet were present. This was attributed to the fact that myosin-10 may be evolved to better orient its foot to initiate a processive run within the actin islands to favor the straddling of myosin-10 in the bundles [109]. While this is difficult to directly measure, comparing the ATPase activity rate for myosin-10 feet between filamentous and bundled actin could provide more support for this theory, since the motor feet would continuously be initiating walks along the bundles.

4.4.2 Actin filaments do not provide favorable geometries for myosin-10 motion

Single actin filaments provide a very different processive behavior for myosin-10. Both myosin constructs that are processive on single actin filaments, M10long-GCN4 and M10long+3-M5CC, need to spiral around the actin filament to continue the processive walk [9, 143, 146]. Even the short processive runs for M10short-GCN4 that occur on filaments demonstrate the potential need for the motor to spiral around the filament [123]. This is likely due to the fact that the myosin motor does not have a long enough step size to support walking on top of the actin filaments, unlike myosin-5 and myosin-6 motors so the motor must compensate for this shorter stepsize by binding actin at sites shorter than the pseudohelical pitch. While the spiraling around actin is allowable for actin filaments suspended in solution, this is less likely of a possible motility behavior for myosin in filopodia due to crowding [123, 151].

4.4.3 Implications for interpreting in vitro *studies*

The determination of the stable coiled-coil in M10short-GCN4 that the M10long-GCN4 and M10long+3-M5CC could have regions of flexibility in the coiled-coil domains. Grouping the structured coiled-coil of M10short-GCN4 with the previously demonstrated bundle-selective motility [108] suggests that this could be the main cause. Likewise the structures for neither M10long-GCN4 and M10long+3-M5CC could be determined, and both of these constructs did not demonstrate track specificity. Since only the coiled-coil domains differed between the three myosin motility studies, the coiled-coil is a likely culprit causing the different behaviors for these constructs to exist. The extra flexibility is supported by the introduction of flexible linker regions before and after the SAH domain diminishing bundle M10short-GCN4 bundle selectivity [109]. This experiment found that the lack of myosin-10 track selectivity is caused by flexible regions occuring before and in the SAH domain.

M10short-GCN4, M10long-GCN4, and M10long+3-M5CC were all designed before the

orientation of the wild-type coiled-coil was determined. The structural determination attempted on the coiled-coil domains of all three of these artificial myosin-10 constructs demonstrates that the association strength of two proteins fused together cannot predict the orientation or association of fused proteins. While this project provides a cautionary protein engineering tale, the main goal of this project is to determine how small changes in the coiled-coil domains of these three proteins could significantly affect observed motility behavior. Currently we are proposing that the introduction of flexibility in myosin-10 allows the motor feet to choose a track and allowing the motor to stretch between actin islands that the native construct may not be able to. Effectively the increased flexibility can act like the lever arms known to exist in myosin-6, which can extend the motor foot conformational change by swinging [141]. Indeed experiments on M10long-GCN4 attempted to propose a similar mechanism present in myosin-10's motility [146].

4.5 Myosin-10 motility in cellular context

4.5.1 Myosin-10 constructs in context with wild-type myosin-10 motility

Due to myosin-10's limited ability to dimerize *in vitro* without additional nucleation domains, artificial constructs like the three described above are the best tool to determining how the wild-type myosin-10 walks inside filopodia on actin tracks. Since all three motor constructs contain unaltered motor feet, IQ domains, and the SAH domain, the coiled-coil becomes the target domain in predicting wild-type myosin-10 motility. Even though both M10long-GCN4 and M10long+3-M5CC both contain the entire M10CC sequence, the M10short-GCN4 coiled-coil has closer structural similarity to the resolved wild-type coiled-coil. The lifetime of the wild-type coiled-coil was measured on the magnitude of days by amide exchange detection, and the experimenters concluded that none of the residues in the coiled-coil exchanged hydrogens with solution [96]. M10short-GCN4's coiled-coil also stably forms one conformation that did not measurable degrade or change over the span of a few

months [159].

One of the largest differences between the coiled-coils of M10short-GCN4 and the myosin-10 wild-type is the N-terminal spacing. Residues 883, the N-termini of the *Homo sapiens* wild-type coiled-coil, have a spacing of 47.1 Å. Residues 884 in M10short-GCN4, the N-termini for this construct and the *Bos taurus* myosin-10 coiled-coil, are spaced 100 Å apart. This means that the length of the M10short-GCN4 coiled-coil is double that from wild-type myosin-10 (Figure 2.12). However myosin-5/myosin-10 chimeras demonstrated that extra length in the leg domains does not diminish bundle selectivity. The replacement of myosin-10's three IQ domains with myosin-5's six IQ domains did not change the motility selection [109]. Therefore we can conclude that the additional length from the M10short-GCN4 coiled-coil compared to the wild-type coiled-coil will not significantly alter the bundle selective behavior of myosin-10. Based on this information, we propose that wild-type myosin-10 selects for bundled actin to locate and select filopodial actin in the cellular environment.

4.5.2 Mechanism of myosin-10 selectivity leads to filopodial selection

Myosin-10's characteristic behavior is the localization to filopodia and concentration at the tips [140]. While the PH domains in myosin-10 may be able to help localize inactive myosin-10 motors to the filopodial base, the track selection is performed by a different mechanism once the motors activate and dimerize [139, 156]. Since filopodial actin contains parallel bundles of actin, the motors are able to find a perfect actin track to initiate and maintain processive motility. Bundle selective motility for myosin-10 would allow the motor to seek out tracks that are enriched in filopodia, rather than select a track that would lead the motor away from filopodial actin and the target cargo destination. Short runs on actin filaments could help myosin-10 motors seek out the correct route when seeking to start a processive run in filopodia by allowing the motor and cargo to move in short bursts until a bundled actin track is found. Bundled actin selection could also lead to the delivery of cargo, such as Mena/VASP, involved in bundled actin polymerization at the end of the track [150]. If no

actin rafts are accessible to the active myosin-10 motor, the processive run can be terminated and the cargo delivered to encourage the growth of more actin in a growing filopodia.

4.6 Future Directions for Myosin-10 Research

4.6.1 Measure the minimal filament composition for bundle controlled myosin-10 activation

Another adaptation of the single molecule TIRF assay includes the polymerization of actin filaments during data collection. This has been previously applied to studies measuring the sensitivity of myosin-5 and myosin-6 to the actin ATP state. Filaments are built by having a mixture of actin monomers with and without a cross-linked conjugate or dye and polymerized on the microscope slide surface (opposite of previous TIRF measurements that included the pre-polymerization of actin tracks in tubes before affixing to the slide surface) [181].

This technique can also be applied to actin bundles by included cross-linking proteins in the polymerization buffers. The orientation of the bundles is confirmed by directly watching the actin polymerization direction, since actin polymerizes at the barbed end of the actin. Additionally the number of filaments at each point in the bundle can be determined by watching the polymerization occur and measuring the relative intensity of the filaments and changes in the fluorescence of the actin over time. Once two or three actin filaments have bundled together, the myosin are monitored for processive walks, and the regions of actin known to contain bundles with different filament compositions can be compared.

Combining this information with previously measured motor step sizes [123] will allow for the refinement of how myosin-10 walks on bundle actin. Determining the minimum number of filaments will, most vitally, provide the step width of myosin-10 during a processive walk and tell us how far the motor heads must stretch to walk along actin. This information would support or refute the presence of a "lever arm," a semi-flexible structure that can stretch when force is applied and is associated with the gating of myosin-6 steps, in myosin-10. This

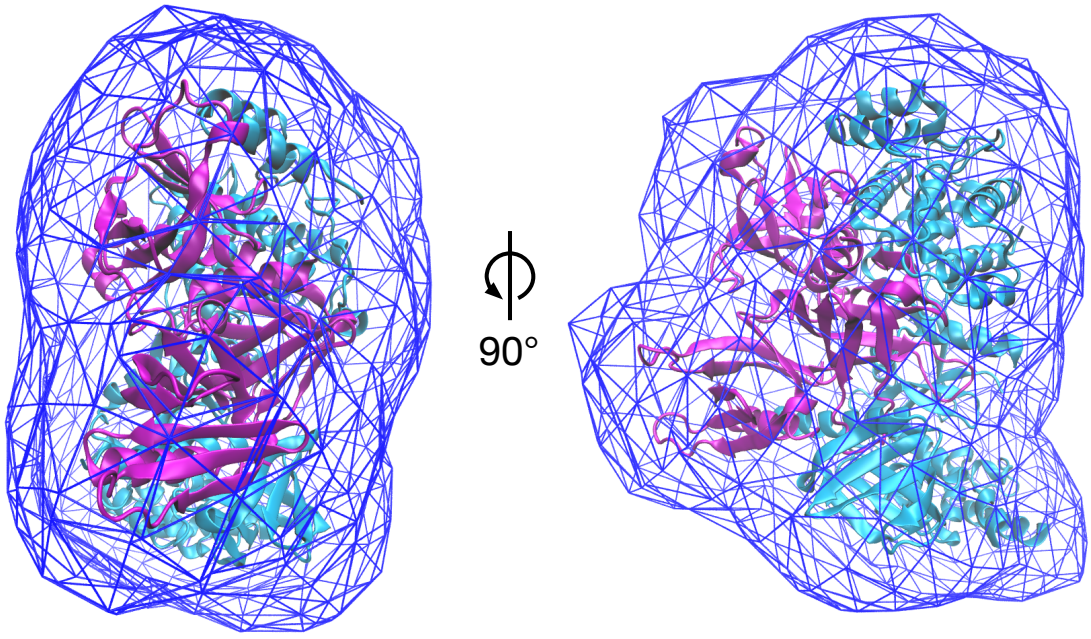

Figure 4.3: PH-MyTH4FERM model shows potential inhibitory interactions. Rigid-body model generated using the PH1-2 structure [97], a homology-based model for PH3 [75, 97], and the MyTH4FERM structure [62]. PH domains (magenta) interact with the cargo-binding regions of the MyTH4-FERM tandem (cyan), and both of these domains fit into a DAMAVER-generated wire frame from the experimental data (blue) The docking of these two domains in the cargo- and lipid-free environment suggests that both domains stabilize each other. More experiments are needed to determine the mechanism for and order of activation in the tail domains.

would also allow for us to apply the structural information gained about the SAH and the coiled-coil in the creation of new models for myosin-10's processive walk [58].

4.6.2 Structural Assessment of myosin-10 lipid and cargo binding in context of motor activation

Myosin-10 in cells is currently predicted to be expressed as an inactive monomer potentially folded upon itself so the cargo-binding tail domains are bound to the motor foot [156]. Individual motors are concentrated in the lamellipodia by PIP_3-enriched membrane present in this region, bring the local concentration to a range that is more compatible with the

lower dimerization affinity of the myosin-10 coiled-coil. The current model predicts that PIP_3 disrupts the stability between the motor foot and the cargo-binding MyTH4-FERM tandem, freeing the MyTH4-FERM domain to bind cargoes concentrating in the lamellopodia [156]. However, this current model has not yet been experimentally verified. We are currently using SAXS to measure the binding order of proteins and lipids to the three PH and MyTH4-FERM domains using a construct called PHMFshort.

Initial SAXS experiments were performed on the PHMFshort contained only the protein construct in solution to determine the structure of the apo domains. Rigid-body modelling creates series multidomain models by connecting known protein structures with flexible linker regions. CORAL was used to create rigid body models of the PHMFShort domains and compared predicted SAXS curves of the models to experimental SAXS data collected on these domains [118]. The structure of the first and second PH domain were previously resolved by X-ray crystallography [97]. The third PH domain currently does not have a publicly deposited structure, but with a 28 % sequence homology and 48 % sequence similarity with PH2, a model of the third PH domain was created using Phyre2 protein homology modelling [75]. One apo MyTH4FERM structure is currently deposited at the PDB [62], so structure was used to model the MyTH4FERM domain. Interestingly, the rigid-body model showed the PH domains in the pocket where the DCC (deleted in colorectal cancer, a myosin-10 cargo) peptide beinds to the MyTH4FERM domain. This suggests a potential stabilization between these two domains with neither lipid nor cargo are present for binding. However, more experiments are needed to conclude this information and find a potential cargo- and lipid-based activation of myosin-10.

We propose continuing these SAXS experiments while using other biochemical characterizations, such as ITC (define), to measure if there is a required order for cargo and lipid binding of PHMFshort. If there is, then the model proposed by Umeki *et al.* [156] is correct. However, the cargo could compete for the MyTH4-FERM binding pocket and push the PH domains out, suggesting that cargo destabilizes inactive myosin-10 monomers and enhances

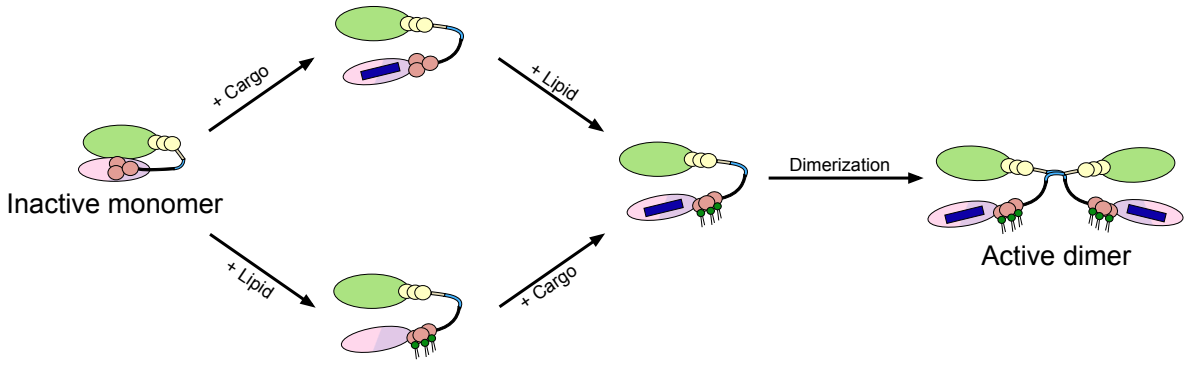

Figure 4.4: The tail domain controls myosin-10 activation through cargo and lipid binding. Diagram of proposed myosin-10 activation based on Umeki *et al.* (2011) [156] findings. Cargo and PIP_3 binding of myosin-10 to the MyTH4-FERM and PH domains, respectively, control myosin-10 activity. Myosin-10 motors are initially expressed as inactive monomers with the motor foot bound to the tail domain, preventing motor activity. Once the lipid and cargo are bound, the monomers and then dimerize via the coiled-coil, leading to an active dimer. Right now it is unknown if cargo or lipid binding is a requisite initial step in the activation pathway we hope to determine using the SAXS experiments described above.

the binding of motors to the membrane only once cargo is bound. Due to technical limitations of measuring lipids with SAXS, mainly over lipid heterogeneity causing artifacts in scattering data, the inositide from PIP_3 will be used as a substitute in preliminary experiments. DCC p3 peptide, which has been shown to bind the MyTH4-FERM tandem, will be used as the cargo in this system [62].

4.6.3 Development of in vitro *assay using wild type myosin-10*

All of the artificial constructs used to measure myosin-10's motility use dimerization schemes that are naturally occurring proteins [108, 109, 123, 143, 151]. Even though these studies and this thesis conclude that wild type myosin-10 selects for bundled actin in oder to localize to filopodia, this statement cannot be conclusively tested without performing single molecule microscopy of wild type motor. Therefore, our research group has a long term goal to apply conclusions about myosin-10's activation to the development of a single molecule assay capable of measuring activated full length motors. Information on tail domain activation with lipid and cargo can provide insight on how myosin-10 initially turns on. This could

potentially be applied to expression and purification protocols for full-length myosin-10 in order to create a better understanding of how wild-type myosin-10 moves into the cells. Currently the proposed assay in our lab uses PIP_3 contained in nanodiscs and an engineered dimer of the small DCC p3 peptide. These two components added during the expression, purification, and/or assay portions of our experiment could provide appropriate signals not present in traditional single molecule assays [76, 130].

The main goal of these studies is to thoroughly test methods myosin-10 uses to select for filopodial actin in the crowded cell environment, especially in the context of the structure of myosin-10 to its behavior. Initially, the structures of individual myosin-10 domains were solved, mostly at the tail domain [62, 97, 96, 167]. This project started with the wildtype myosin-10 coiled coil and looked into the structure of different constructs to link orientation and flexibility to increased and decreased bundle selectivity of *in vitro* constructs [159]. Next we attempted to link the coiled-coil to the SAH domain to determine how regions between the motor feet and the coiled-coil domain can impact motor behavior. At the same time, our structural studies also expanded to the tail domain since these domains are thought to be important in the regulation of myosin-10 [156].

The ability for myosin-10 motors to exhibit bundle selectivity has been associated with a stable antiparallel coiled coil in this thesis [159]. However there are still many other unknown aspects to myosin-10's activation and motility that need to be better understood. One important question relates to myosin-10 activation and the mechanisms by which this happens. Studying the conformational changes associated when the addition of cargo and lipid are present is the first step in answering how the activation occurs. Additionally the current definition of how myosin-10 remains inactive without signal is unclear [156], so conformational changes associated with myosin-10 tail domain lipid- and cargo-binding could help explain the link between the tail domains and motor feet in activation signalling.

Additionally the design and optimization of a single molecule assay using an activated full length myosin-10 motor can benefit from further studies about myosin-10's structure and

function, since technical limitations still impact the ability to study a wildtype construct [76]. The current model linking the orientation of the coiled-coil domain to motility behavior is clear, but bundle selection by the wildtype motor is based on conclusions in Chapter 2 [159]. This model works to link coiled-coil orientation to bundle selectivity, but the model could be improved with a future measurement of full length myosin-10 if the assay can include the appropriate activation and lipid binding signals.

BIBLIOGRAPHY

[1] Alexei A Adzhubei, Michael JE Sternberg, and Alexander A Makarov. Polyproline-II helix in proteins: structure and function. *Journal of molecular biology*, 425(12):2100–2132, 2013.

[2] Sohail Ahmed, Wah Ing Goh, and Wenyu Bu. I-BAR domains, IRSp53 and filopodium formation. *Semin Cell Dev Biol*, 21(4):350–6, Jun 2010.

[3] Sébastien Almagro, Claire Durmort, Adeline Chervin-Pétinot, Stephanie Heyraud, Mathilde Dubois, Olivier Lambert, Camille Maillefaud, Elizabeth Hewat, Jean Patrick Schaal, Philippe Huber, et al. The motor protein myosin-X transports VE-cadherin along filopodia to allow the formation of early endothelial cell-cell contacts. *Molecular and cellular biology*, 30(7):1703–1717, 2010.

[4] Surya P. Amarachintha, Kenneth J. Ryan, Marilyn Cayer, Nancy S. Boudreau, Nathan M. Johnson, and Carol A. Heckman. Effect of Cdc42 domains on filopodia sensing, cell orientation, and haptotaxis. *Cellular Signalling*, 27(3):683 – 693, 2015.

[5] Hideya Ando, Yoko Niki, Masaaki Ito, Kaoru Akiyama, Mary S Matsui, Daniel B Yarosh, and Masamitsu Ichihashi. Melanosomes are transferred from melanocytes to keratinocytes through the processes of packaging, release, uptake, and dispersion. *J Invest Dermatol*, 132(4):1222–9, Apr 2012.

[6] Thomas G Baboolal, Takeshi Sakamoto, Eva Forgacs, Howard D White, Scott M Jackson, Yasuharu Takagi, Rachel E Farrow, Justin E Molloy, Peter J Knight, James R Sellers, and Michelle Peckham. The SAH domain extends the functional length of the myosin lever. *Proc Natl Acad Sci U S A*, 106(52):22193–8, Dec 2009.

[7] Robert L Baldwin and George D Rose. Molten globules, entropy-driven conformational change and protein folding. *Curr Opin Struct Biol*, 23(1):4–10, Feb 2013.

[8] D W Banner, M Kokkinidis, and D Tsernoglou. Structure of the ColE1 rop protein at 1.7 A resolution. *J Mol Biol*, 196(3):657–75, Aug 1987.

[9] Jianjun Bao, Daniel Huck, Laura K Gunther, James R Sellers, and Takeshi Sakamoto. Actin structure-dependent stepping of myosin 5a and 10 during processive movement. *PLoS One*, 8(9):e74936, 2013.

[10] Christopher Batters and Claudia Veigel. Using optical tweezers to study the fine details of myosin ATPase mechanochemical cycle. *Methods Mol Biol*, 778:97–109, 2011.

[11] James E Bear, Tatyana M Svitkina, Matthias Krause, Dorothy A Schafer, Joseph J Loureiro, Geraldine A Strasser, Ivan V Maly, Oleg Y Chaga, John A Cooper, Gary G Borisy, and Frank B Gertler. Antagonism between Ena/VASP proteins and actin filament capping regulates fibroblast motility. *Cell*, 109(4):509–21, May 2002.

[12] Richard D Bennett, Ariel J Caride, Amy S Mauer, and Emanuel E Strehler. Interaction with the IQ3 motif of myosin-10 is required for calmodulin-like protein-dependent filopodial extension. *FEBS Lett*, 582(16):2377–81, Jul 2008.

[13] Richard D Bennett, Amy S Mauer, Mark R Pittelkow, and Emanuel E Strehler. Calmodulin-like protein upregulates myosin-10 in human keratinocytes and is regulated during epidermal wound healing in vivo. *J Invest Dermatol*, 129(3):765–9, Mar 2009.

[14] J S Berg, B H Derfler, C M Pennisi, D P Corey, and R E Cheney. Myosin-X, a novel myosin with pleckstrin homology domains, associates with regions of dynamic actin. *J Cell Sci*, 113 Pt 19:3439–51, Oct 2000.

[15] Aneerban Bhattacharya, Roberto Tejero, and Gaetano T Montelione. Evaluating protein structures determined by structural genomics consortia. *Proteins*, 66(4):778–95, Mar 2007.

[16] Laurent Blanchoin, Rajaa Boujemaa-Paterski, Cécile Sykes, and Julie Plastino. Actin dynamics, architecture, and mechanics in cell motility. *Physiol Rev*, 94(1):235–63, Jan 2014.

[17] Erich T. Boger, Gregory I. Frolenkov, Thomas B. Friedman, and Inna A. Belyantseva. *Myosins: A Superfamily of Molecular Motors*, chapter Myosin XVA, pages 441–467. Springer Netherlands, Dordrecht, 2008.

[18] Thomas Bornschlögl. How filopodia pull: what we know about the mechanics and dynamics of filopodia. *Cytoskeleton (Hoboken)*, 70(10):590–603, Oct 2013.

[19] Crista M Brawley and Ronald S Rock. Unconventional myosin traffic in cells reveals a selective actin cytoskeleton. *Proc Natl Acad Sci U S A*, 106(24):9685–90, Jun 2009.

[20] Rubén M Buey, Indrani Sen, Oliver Kortt, Renu Mohan, David Gfeller, Dmitry Veprintsev, Ines Kretzschmar, Jörg Scheuermann, Dario Neri, Vincent Zoete, Olivier Michielin, José María de Pereda, Anna Akhmanova, Rudolf Volkmer, and Michel O Steinmetz. Sequence determinants of a microtubule tip localization signal (MtLS). *J Biol Chem*, 287(34):28227–42, Aug 2012.

[21] P A Bullough, F M Hughson, J J Skehel, and D C Wiley. Structure of influenza haemagglutinin at the pH of membrane fusion. *Nature*, 371(6492):37–43, Sep 1994.

[22] Matthew A Caporizzo, Claire E Fishman, Sato Osamu, Mitsuo Ikebe, and Yale E Goldman. Comparing the motility of myosin X with parallel and anti-parallel dimerization domains. In *Proceedings of the 60th Annual Meeting of the Biophysical Society*, February 2016.

[23] Z Y Chen, T Hasson, D S Zhang, B J Schwender, B H Derfler, M S Mooseker, and D P Corey. Myosin-VIIb, a novel unconventional myosin, is a constituent of microvilli in transporting epithelia. *Genomics*, 72(3):285–96, Mar 2001.

[24] R E Cheney and M S Mooseker. Unconventional myosins. *Curr Opin Cell Biol*, 4(1):27–35, Feb 1992.

[25] C Cohen and D A Parry. Alpha-helical coiled coils and bundles: how to design an alpha-helical protein. *Proteins*, 7(1):1–15, 1990.

[26] David S Courson and Richard E Cheney. Myosin-X and disease. *Exp Cell Res*, 334(1):10–15, May 2015.

[27] David S Courson and Ronald S Rock. Actin cross-link assembly and disassembly mechanics for alpha-actinin and fascin. *J Biol Chem*, 285(34):26350–7, Aug 2010.

[28] Dianne Cox, Jonathan S Berg, Michael Cammer, John O Chinegwundoh, Benjamin M Dale, Richard E Cheney, and Steven Greenberg. Myosin X is a downstream effector of PI(3)K during phagocytosis. *Nat Cell Biol*, 4(7):469–77, Jul 2002.

[29] Joseph E. Curtis, Sindhu Raghunandan, Hirsh Nanda, and Susan Krueger. SASSIE: A program to study intrinsically disordered biological molecules and macromolecular ensembles using experimental scattering restraints. *Computer Physics Communications*, 183(2):382 – 389, 2012.

[30] E M De La Cruz, E M Ostap, and H L Sweeney. Kinetic mechanism and regulation of myosin VI. *J Biol Chem*, 276(34):32373–81, Aug 2001.

[31] E M De La Cruz, H L Sweeney, and E M Ostap. ADP inhibition of myosin V ATPase activity. *Biophys J*, 79(3):1524–9, Sep 2000.

[32] E M De La Cruz, A L Wells, S S Rosenfeld, E M Ostap, and H L Sweeney. The kinetic mechanism of myosin V. *Proc Natl Acad Sci U S A*, 96(24):13726–31, Nov 1999.

[33] Enrique M De La Cruz and E Michael Ostap. Relating biochemistry and function in the myosin superfamily. *Curr Opin Cell Biol*, 16(1):61–7, Feb 2004.

[34] F. Delaglio, S. Grzesiek, G. W. Vuister, G. Zhu, J. Pfeifer, and A. Bax. NMRPipe: a multidimensional spectral processing system based on UNIX pipes. *J Biomol NMR*, 6(3):277–293, 1995.

[35] Yiqun Deng, Jie Liu, Qi Zheng, David Eliezer, Neville R Kallenbach, and Min Lu. Antiparallel four-stranded coiled coil specified by a 3-3-1 hydrophobic heptad repeat. *Structure*, 14(2):247–55, Feb 2006.

[36] Erik W Dent, Adam V Kwiatkowski, Leslie M Mebane, Ulrike Philippar, Melanie Barzik, Douglas A Rubinson, Stephanie Gupton, J Edward Van Veen, Craig Furman, Jiangyang Zhang, Arthur S Alberts, Susumu Mori, and Frank B Gertler. Filopodia are required for cortical neurite initiation. *Nat Cell Biol*, 9(12):1347–59, Dec 2007.

[37] Alexey Drozdetskiy, Christian Cole, James Procter, and Geoffrey J Barton. JPred4: a protein secondary structure prediction server. *Nucleic Acids Res*, 43(W1):W389–94, Jul 2015.

[38] Robert A Edwards and Joseph Bryan. Fascins, a family of actin bundling proteins. *Cell motility and the cytoskeleton*, 32(1):1–9, 1995.

[39] E Eisenberg and C Moos. The adenosine triphosphatase activity of acto-heavy meromyosin. a kinetic analysis of actin activation. *Biochemistry*, 7(4):1486–9, Apr 1968.

[40] Jan Faix and Klemens Rottner. The making of filopodia. *Curr Opin Cell Biol*, 18(1):18–25, Feb 2006.

[41] D. Franke and D. I. Svergun. DAMMIF, a program for rapid ab-initio shape determination in small-angle scattering. *J. Appl. Cryst*, 42:342–346, 2009.

[42] Daniel Franke, Alexey G. Kikhney, and Dmitri I. Svergun. Automated acquisition and analysis of small angle x-ray scattering data. *Nuclear Instruments and Methods in Physics Research Section A: Accelerators, Spectrometers, Detectors and Associated Equipment*, 689:52 – 59, 2012.

[43] Catherine G Galbraith, Kenneth M Yamada, and James A Galbraith. Polymerizing actin fibers position integrins primed to probe for adhesion sites. *Science*, 315(5814):992–5, Feb 2007.

[44] Holger Gerhardt, Matthew Golding, Marcus Fruttiger, Christiana Ruhrberg, Andrea Lundkvist, Alexandra Abramsson, Michael Jeltsch, Christopher Mitchell, Kari Alitalo, David Shima, and Christer Betsholtz. VEGF guides angiogenic sprouting utilizing endothelial tip cell filopodia. *J Cell Biol*, 161(6):1163–77, Jun 2003.

[45] Daniel G Gibson, Lei Young, Ray-Yuan Chuang, J Craig Venter, Clyde A Hutchison, 3rd, and Hamilton O Smith. Enzymatic assembly of DNA molecules up to several hundred kilobases. *Nat Methods*, 6(5):343–5, May 2009.

[46] Wah Ing Goh, Thankiah Sudhaharan, Kim Buay Lim, Kai Ping Sem, Chew Ling Lau, and Sohail Ahmed. Rif-mDia1 interaction is involved in filopodium formation independent of Cdc42 and Rac effectors. *Journal of Biological Chemistry*, 286(15):13681–13694, 2011.

[47] Timothy M Gomez and Paul C Letourneau. Actin dynamics in growth cone motility and navigation. *J Neurochem*, 129(2):221–34, Apr 2014.

[48] L Gonzalez, Jr, J J Plecs, and T Alber. An engineered allosteric switch in leucine-zipper oligomerization. *Nat Struct Biol*, 3(6):510–5, Jun 1996.

[49] Norma J Greenfield. Using circular dichroism spectra to estimate protein secondary structure. *Nat Protoc*, 1(6):2876–90, 2006.

[50] Gevorg Grigoryan and William F Degrado. Probing designability via a generalized model of helical bundle geometry. *J Mol Biol*, 405(4):1079–100, Jan 2011.

[51] Gevorg Grigoryan and Amy E Keating. Structural specificity in coiled-coil interactions. *Curr Opin Struct Biol*, 18(4):477–83, Aug 2008.

[52] Barry M Gumbiner. Cell adhesion: the molecular basis of tissue architecture and morphogenesis. *Cell*, 84(3):345–357, 1996.

[53] Stephanie L Gupton and Frank B Gertler. Filopodia: the fingers that do the walking. *Sci STKE*, 2007(400):re5, Sep 2007.

[54] Daniel G Gurnon, Jennifer A Whitaker, and Martha G Oakley. Design and characterization of a homodimeric antiparallel coiled coil. *J Am Chem Soc*, 125(25):7518–9, Jun 2003.

[55] Erik B Hadley and Samuel H Gellman. An antiparallel alpha-helical coiled-coil model system for rapid assessment of side-chain recognition at the hydrophobic interface. *J Am Chem Soc*, 128(51):16444–5, Dec 2006.

[56] Erik B Hadley, Oliver D Testa, Derek N Woolfson, and Samuel H Gellman. Preferred side-chain constellations at antiparallel coiled-coil interfaces. *Proc Natl Acad Sci U S A*, 105(2):530–5, Jan 2008.

[57] Young-Hoon Han, Chang Y Chung, Deborah Wessels, Stephen Stephens, Margaret A Titus, David R Soll, and Richard A Firtel. Requirement of a vasodilator-stimulated phosphoprotein family member for cell adhesion, the formation of filopodia, and chemotaxis in dictyostelium. *J Biol Chem*, 277(51):49877–87, Dec 2002.

[58] Rizal F Hariadi, Mario Cale, and Sivaraj Sivaramakrishnan. Myosin lever arm directs collective motion on cellular actin network. *Proceedings of the National Academy of Sciences*, 111(11):4091–4096, 2014.

[59] Marcus D Hartmann, Oswin Ridderbusch, Kornelius Zeth, Reinhard Albrecht, Oli Testa, Derek N Woolfson, Guido Sauer, Stanislaw Dunin-Horkawicz, Andrei N Lupas, and Birte Hernandez Alvarez. A coiled-coil motif that sequesters ions to the hydrophobic core. *Proc Natl Acad Sci U S A*, 106(40):16950–5, Oct 2009.

[60] Yosuke Hashimoto, Marek Skacel, and Josephine C Adams. Roles of fascin in human carcinoma motility and signaling: prospects for a novel biomarker? *Int J Biochem Cell Biol*, 37(9):1787–804, Sep 2005.

[61] Andreas Hinz, Guy Schoehn, Heribert Quendler, David Lutje Hulsik, Gabi Stiegler, Hermann Katinger, Michael S Seaman, David Montefiori, and Winfried Weissenhorn. Characterization of a trimeric MPER containing HIV-1 gp41 antigen. *Virology*, 390(2):221–7, Aug 2009.

[62] Yoshinori Hirano, Taiki Hatano, Aya Takahashi, Michinori Toriyama, Naoyuki Inagaki, and Toshio Hakoshima. Structural basis of cargo recognition by the myosin-X MyTH4-FERM domain. *EMBO J*, 30(13):2734–47, Jul 2011.

[63] Matthew K Hoelzle and Tatyana Svitkina. The cytoskeletal mechanisms of cell-cell junction formation in endothelial cells. *Mol Biol Cell*, 23(2):310–23, Jan 2012.

[64] James Holton and Tom Alber. Automated protein crystal structure determination using ELVES. *Proc Natl Acad Sci U S A*, 101(6):1537–42, Feb 2004.

[65] K Homma, J Saito, R Ikebe, and M Ikebe. Motor function and regulation of myosin X. *J Biol Chem*, 276(36):34348–54, Sep 2001.

[66] Kazuaki Homma and Mitsuo Ikebe. Myosin X is a high duty ratio motor. *J Biol Chem*, 280(32):29381–91, Aug 2005.

[67] W. Humphrey, A. Dalke, and K. Schulten. VMD - visual molecular dynamics. *Journal of Molecular Graphics*, 14:33–38, 1996.

[68] A Jacinto, W Wood, T Balayo, M Turmaine, A Martinez-Arias, and P Martin. Dynamic actin-based epithelial adhesion and cell matching during Drosophila dorsal closure. *Curr Biol*, 10(22):1420–6, Nov 2000.

[69] Guillaume Jacquemet, Hellyeh Hamidi, and Johanna Ivaska. Filopodia in cell adhesion, 3D migration and cancer cell invasion. *Curr Opin Cell Biol*, 36:23–31, Oct 2015.

[70] Colin Jamora and Elaine Fuchs. Intercellular adhesion, signalling and the cytoskeleton. *Nat Cell Biol*, 4(4):E101–8, Apr 2002.

[71] Silvia Jansen, Agnieszka Collins, Changsong Yang, Grzegorz Rebowski, Tatyana Svitkina, and Roberto Dominguez. Mechanism of actin filament bundling by fascin. *Journal of Biological Chemistry*, 286(34):30087–30096, 2011.

[72] Nathan H Joh, Tuo Wang, Manasi P Bhate, Rudresh Acharya, Yibing Wu, Michael Grabe, Mei Hong, Gevorg Grigoryan, and William F DeGrado. De novo design of a transmembrane Zn2+-transporting four-helix bundle. *Science*, 346(6216):1520–4, Dec 2014.

[73] G E Jones. Cellular signaling in macrophage migration and chemotaxis. *J Leukoc Biol*, 68(5):593–602, Nov 2000.

[74] Toshiyuki Kakumoto and Takao Nakata. Optogenetic control of PIP3: PIP3 is sufficient to induce the actin-based active part of growth cones and is regulated via endocytosis. *PLoS One*, 8(8):e70861, 2013.

[75] Lawrence A Kelley, Stefans Mezulis, Christopher M Yates, Mark N Wass, and Michael J E Sternberg. The Phyre2 web portal for protein modeling, prediction and analysis. *Nat Protoc*, 10(6):845–58, Jun 2015.

[76] Michael L Kerber and Richard E Cheney. Myosin-X: a MyTH-FERM myosin at the tips of filopodia. *J Cell Sci*, 124(Pt 22):3733–41, Nov 2011.

[77] Michael L Kerber, Damon T Jacobs, Luke Campagnola, Brian D Dunn, Taofei Yin, Aurea D Sousa, Omar A Quintero, and Richard E Cheney. A novel form of motility in filopodia revealed by imaging myosin-X at the single-molecule level. *Curr Biol*, 19(11):967–73, Jun 2009.

[78] Andrea Ketschek and Gianluca Gallo. Nerve growth factor induces axonal filopodia through localized microdomains of phosphoinositide 3-kinase activity that drive the formation of cytoskeletal precursors to filopodia. *J Neurosci*, 30(36):12185–97, Sep 2010.

[79] Seema Khurana and Sudeep P George. The role of actin bundling proteins in the assembly of filopodia in epithelial cells. *Cell adhesion & migration*, 5(5):409–420, 2011.

[80] Joshua S Klein, Siduo Jiang, Rachel P Galimidi, Jennifer R Keeffe, and Pamela J Bjorkman. Design and characterization of structured protein linkers with differing flexibilities. *Protein Eng Des Sel*, 27(10):325–30, Oct 2014.

[81] Jane A Knappenberger, Jennifer E Smith, Sarah H Thorpe, Jill A Zitzewitz, and C Robert Matthews. A buried polar residue in the hydrophobic interface of the coiled-coil peptide, GCN4-p1, plays a thermodynamic, not a kinetic role in folding. *J Mol Biol*, 321(1):1–6, Aug 2002.

[82] Peter J Knight, Kavitha Thirumurugan, Yuhui Xu, Fei Wang, Arnout P Kalverda, Walter F Stafford, 3rd, James R Sellers, and Michelle Peckham. The predicted coiled-coil domain of myosin 10 forms a novel elongated domain that lengthens the head. *J Biol Chem*, 280(41):34702–8, Oct 2005.

[83] Michel H Koch, Patrice Vachette, and Dmitri I Svergun. Small-angle scattering: a view on the properties, structures and structural changes of biological macromolecules in solution. *Q Rev Biophys*, 36(2):147–227, May 2003.

[84] David R Kovar, Elizabeth S Harris, Rachel Mahaffy, Henry N Higgs, and Thomas D Pollard. Control of the assembly of ATP- and ADP-actin by formins and profilin. *Cell*, 124(2):423–35, Jan 2006.

[85] Holger Kress, Ernst H K Stelzer, Daniela Holzer, Folma Buss, Gareth Griffiths, and Alexander Rohrbach. Filopodia act as phagocytic tentacles and pull with discrete steps and a load-dependent velocity. *Proc Natl Acad Sci U S A*, 104(28):11633–8, Jul 2007.

[86] Sonja Krugmann, Ingrid Jordens, Kris Gevaert, Maritte Driessens, Joel Vandekerckhove, and Alan Hall. Cdc42 induces filopodia by promoting the formation of an IRSp53:Mena complex. *Current Biology*, 11(21):1645 – 1655, 2001.

[87] Mingming Lai, Ye Guo, Jun Ma, Huali Yu, Dongdong Zhao, Wenqiang Fan, Xingda Ju, Muhammad A Sheikh, Yousra S Malik, Wencheng Xiong, et al. Myosin X regulates neuronal radial migration through interacting with N-cadherin. *Frontiers in cellular neuroscience*, 9, 2015.

[88] David Lambright, Andrew W Malaby, Sagar V Kathuria, R Paul Nobrega, Osman Bilsel, C Robert Matthews, Uma Muthurajan, Karolin Luger, Rajiv Chopra, Thomas C Irving, et al. Complementary techniques enhance the quality and scope of information obtained from SAXS. *ACA Trans*, pages 1–12, 2013.

[89] Maik J Lehmann, Nathan M Sherer, Carolyn B Marks, Marc Pypaert, and Walther Mothes. Actin- and myosin-driven movement of viruses along filopodia precedes their entry into cells. *J Cell Biol*, 170(2):317–25, Jul 2005.

[90] Yu Li, Suet Mui, Jerry H Brown, James Strand, Ludmilla Reshetnikova, Larry S Tobacman, and Carolyn Cohen. The crystal structure of the C-terminal fragment of striated-muscle alpha-tropomyosin reveals a key troponin T recognition site. *Proc Natl Acad Sci U S A*, 99(11):7378–83, May 2002.

[91] Y Liang, A Wang, I A Belyantseva, D W Anderson, F J Probst, T D Barber, W Miller, J W Touchman, L Jin, S L Sullivan, J R Sellers, S A Camper, R V Lloyd, B Kachar, T B Friedman, and R A Fridell. Characterization of the human and mouse unconventional myosin XV genes responsible for hereditary deafness DFNB3 and shaker 2. *Genomics*, 61(3):243–58, Nov 1999.

[92] Diane S Lidke, Keith A Lidke, Bernd Rieger, Thomas M Jovin, and Donna J Arndt-Jovin. Reaching out for signals: filopodia sense EGF and respond by directed retrograde transport of activated receptors. *J Cell Biol*, 170(4):619–26, Aug 2005.

[93] Xingcheng Lin, Nathanial R Eddy, Jeffrey K Noel, Paul C Whitford, Qinghua Wang, Jianpeng Ma, and José N Onuchic. Order and disorder control the functional rearrangement of influenza hemagglutinin. *Proc Natl Acad Sci U S A*, 111(33):12049–54, Aug 2014.

[94] H. Lodish, A. Berk, S. Lawrence Zipursky, P. Matsudaira, D. Baltimore, and J. Darnell. *Molecular Cell Biology*, chapter Myosin, the Actin Motor Protein. W.H. Freeman, New York, 4th edition edition, 2000.

[95] Laura Anne Lowery and David Van Vactor. The trip of the tip: understanding the growth cone machinery. *Nat Rev Mol Cell Biol*, 10(5):332–43, May 2009.

[96] Qing Lu, Fei Ye, Zhiyi Wei, Zilong Wen, and Mingjie Zhang. Antiparallel coiled-coil-mediated dimerization of myosin X. *Proc Natl Acad Sci U S A*, 109(43):17388–93, Oct 2012.

[97] Qing Lu, Jiang Yu, Jing Yan, Zhiyi Wei, and Mingjie Zhang. Structural basis of the myosin X PH1(N)-PH2-PH1(C) tandem as a specific and acute cellular PI(3,4,5)P(3) sensor. *Mol Biol Cell*, 22(22):4268–78, Nov 2011.

[98] R W Lymn and E W Taylor. Mechanism of adenosine triphosphate hydrolysis by actomyosin. *Biochemistry*, 10(25):4617–24, Dec 1971.

[99] Laura M Machesky. Lamellipodia and filopodia in metastasis and invasion. *FEBS Lett*, 582(14):2102–11, Jun 2008.

[100] A Mallavarapu and T Mitchison. Regulated actin cytoskeleton assembly at filopodium tips controls their extension and retraction. *J Cell Biol*, 146(5):1097–106, Sep 1999.

[101] Pieta K Mattila and Pekka Lappalainen. Filopodia: molecular architecture and cellular functions. *Nat Rev Mol Cell Biol*, 9(6):446–54, Jun 2008.

[102] A V McDonnell, T Jiang, A E Keating, and B Berger. Paircoil2: improved prediction of coiled coils from sequence. *Bioinformatics*, 22(3):356–8, Feb 2006.

[103] Alphée Michelot and David G Drubin. Building distinct actin filament networks in a common cytoplasm. *Curr Biol*, 21(14):R560–9, Jul 2011.

[104] J E Molloy, J E Burns, J Kendrick-Jones, R T Tregear, and D C White. Movement and force produced by a single myosin head. *Nature*, 378(6553):209–12, Nov 1995.

[105] M S Mooseker and R E Cheney. Unconventional myosins. *Annu Rev Cell Dev Biol*, 11:633–75, 1995.

[106] A. Morin, B. Eisenbraun, J. Key, P. C. Sanschagrin, M. A. Timony, M. Ottaviano, and P. Sliz. Cutting edge: Collaboration gets the most out of software. *eLife*, 2, Sep 2013.

[107] Stefanie Mühlhausen and Martin Kollmar. Whole genome duplication events in plant evolution reconstructed and predicted using myosin motor proteins. *BMC Evol Biol*, 13:202, 2013.

[108] Stanislav Nagy, Benjamin L Ricca, Melanie F Norstrom, David S Courson, Crista M Brawley, Philip A Smithback, and Ronald S Rock. A myosin motor that selects bundled actin for motility. *Proc Natl Acad Sci U S A*, 105(28):9616–9620, 2008.

[109] Stanislav Nagy and Ronald S Rock. Structured post-IQ domain governs selectivity of myosin X for fascin-actin bundles. *J Biol Chem*, 285(34):26608–17, Aug 2010.

[110] C D Nobes and A Hall. Rho, rac, and cdc42 GTPases regulate the assembly of multimolecular focal complexes associated with actin stress fibers, lamellipodia, and filopodia. *Cell*, 81(1):53–62, Apr 1995.

[111] M G Oakley and J J Hollenbeck. The design of antiparallel coiled coils. *Curr Opin Struct Biol*, 11(4):450–7, Aug 2001.

[112] Florian Odronitz and Martin Kollmar. Drawing the tree of eukaryotic life based on the analysis of 2,269 manually annotated myosins from 328 species. *Genome Biol*, 8(9):R196, 2007.

[113] E K O'Shea, J D Klemm, P S Kim, and T Alber. X-ray structure of the GCN4 leucine zipper, a two-stranded, parallel coiled coil. *Science*, 254(5031):539–44, Oct 1991.

[114] Michelle Peckham. Coiled coils and SAH domains in cytoskeletal molecular motors. *Biochem Soc Trans*, 39(5):1142–8, Oct 2011.

[115] Michelle Peckham and Peter J. Knight. When a predicted coiled coil is really a single alpha-helix, in myosins and other proteins. *Soft Matter*, 5:2493–2503, 2009.

[116] Stéphanie Pellegrin and Harry Mellor. The Rho family GTPase Rif induces filopodia through mDia2. *Curr Biol*, 15(2):129–33, Jan 2005.

[117] Jun Peng, Bradley J Wallar, Akiko Flanders, Pamela J Swiatek, and Arthur S Alberts. Disruption of the Diaphanous-related formin Drf1 gene encoding mDia1 reveals a role for Drf3 as an effector for Cdc42. *Curr Biol*, 13(7):534–45, Apr 2003.

[118] M. V. Petoukhov, D. Franke, A. V. Shkumatov, G. Tria, A. G. Kikhney, M. Gajda, C. Gorba, H. D. T. Mertens, P. V. Konarev, and D. I. Svergun. New developments in the ATSAS program package for small-angle scattering data analysis. *J. Appl. Cryst*, 45:342–350, 2012.

[119] M. V. Petoukhov, P. V. Konarev, A. G. Kikhney, and D. I. Svergun. ATSAS 2.1 - towards automated and web-supported small-angle scattering data analysis. *J. Appl. Cryst*, 40:223–228, Apr 2007. Supplement.

[120] Laure Plantard, Antti Arjonen, John G Lock, Ghasem Nurani, Johanna Ivaska, and Staffan Strömblad. PtdIns(3,4,5)P3is a regulator of myosin-X localization and filopodia formation. *J Cell Sci*, 123(Pt 20):3525–34, Oct 2010.

[121] Alexander N Raines, Sarbajeet Nagdas, Michael L Kerber, and Richard E Cheney. Headless Myo10 is a negative regulator of full-length Myo10 and inhibits axon outgrowth in cortical neurons. *J Biol Chem*, 287(30):24873–83, Jul 2012.

[122] I Rayment. The structural basis of the myosin ATPase activity. *J Biol Chem*, 271(27):15850–3, Jul 1996.

[123] Benjamin L Ricca and Ronald S Rock. The stepping pattern of myosin X is adapted for processive motility on bundled actin. *Biophys J*, 99(6):1818–26, Sep 2010.

[124] Anne J Ridley. Rho GTPases and actin dynamics in membrane protrusions and vesicle trafficking. *Trends Cell Biol*, 16(10):522–9, Oct 2006.

[125] Dmitri Rozanov, Paul Spellman, Alexei Savinov, and Alex Y Strongin. A humanized leucine zipper-TRAIL hybrid induces apoptosis of tumors both in vitro and in vivo. *PLoS One*, 10(4):e0122980, 2015.

[126] Juha Saarikangas, Hongxia Zhao, Anette Pykäläinen, Pasi Laurinmäki, Pieta K Mattila, Paavo K J Kinnunen, Sarah J Butcher, and Pekka Lappalainen. Molecular mechanisms of membrane deformation by I-BAR domain proteins. *Curr Biol*, 19(2):95–107, Jan 2009.

[127] V Saudek, A Pastore, M A Morelli, R Frank, H Gausepohl, and T Gibson. The solution structure of a leucine-zipper motif peptide. *Protein Eng*, 4(5):519–29, Jun 1991.

[128] Antje Schirenbeck, Till Bretschneider, Rajesh Arasada, Michael Schleicher, and Jan Faix. The diaphanous-related formin dDia2 is required for the formation and maintenance of filopodia. *Nat Cell Biol*, 7(6):619–25, Jun 2005.

[129] Marie Schoumacher, Robert D Goldman, Daniel Louvard, and Danijela M Vignjevic. Actin, microtubules, and vimentin intermediate filaments cooperate for elongation of invadopodia. *J Cell Biol*, 189(3):541–56, May 2010.

[130] Gerhard J Schütz, Gerald Kada, Vassili Ph Pastushenko, and Hansgeorg Schindler. Properties of lipid microdomains in a muscle cell membrane visualized by single molecule microscopy. *The EMBO journal*, 19(5):892–901, 2000.

[131] C. D. Schwieters, J. J. Kuszewski, N. Tjandra, and G. M. Clore. The Xplor-NIH NMR molecular structure determination package. *J Magn Reson*, 160(1):65–73, 2003.

[132] Giorgio Scita, Stefano Confalonieri, Pekka Lappalainen, and Shiro Suetsugu. IRSp53: crossing the road of membrane and actin dynamics in the formation of membrane protrusions. *Trends Cell Biol*, 18(2):52–60, Feb 2008.

[133] Glynis Scott, Sonya Leopardi, Stacey Printup, and Brian C Madden. Filopodia are conduits for melanosome transfer to keratinocytes. *J Cell Sci*, 115(Pt 7):1441–51, Apr 2002.

[134] Yang Shen, Frank Delaglio, Gabriel Cornilescu, and Ad Bax. TALOS+: a hybrid method for predicting protein backbone torsion angles from NMR chemical shifts. *J Biomol NMR*, 44(4):213–23, Aug 2009.

[135] Nathan M Sherer, Maik J Lehmann, Luisa F Jimenez-Soto, Christina Horensavitz, Marc Pypaert, and Walther Mothes. Retroviruses can establish filopodial bridges for efficient cell-to-cell transmission. *Nat Cell Biol*, 9(3):310–5, Mar 2007.

[136] Suman K Singh, Robin Kurfurst, Carine Nizard, Sylvianne Schnebert, Eric Perrier, and Desmond J Tobin. Melanin transfer in human skin cells is mediated by filopodia–a model for homotypic and heterotypic lysosome-related organelle transfer. *FASEB J*, 24(10):3756–69, Oct 2010.

[137] S Sivaramakrishnan, J Sung, M Ali, S Doniach, H Flyvbjerg, and J A Spudich. Combining single-molecule optical trapping and small-angle x-ray scattering measurements to compute the persistence length of a protein ER/K alpha-helix. *Biophys J*, 97(11):2993–9, Dec 2009.

[138] C L Smith. Cytoskeletal movements and substrate interactions during initiation of neurite outgrowth by sympathetic neurons in vitro. *J Neurosci*, 14(1):384–98, Jan 1994.

[139] Aurea D Sousa, Jonathan S Berg, Brian W Robertson, Rick B Meeker, and Richard E Cheney. Myo10 in brain: developmental regulation, identification of a headless isoform and dynamics in neurons. *J Cell Sci*, 119(Pt 1):184–94, Jan 2006.

[140] Aurea D Sousa and Richard E Cheney. Myosin-X: a molecular motor at the cell's fingertips. *Trends Cell Biol*, 15(10):533–9, Oct 2005.

[141] James A Spudich and Sivaraj Sivaramakrishnan. Myosin VI: an innovative motor that challenged the swinging lever arm hypothesis. *Nat Rev Mol Cell Biol*, 11(2):128–37, Feb 2010.

[142] Sergei V Strelkov and Peter Burkhard. Analysis of alpha-helical coiled coils with the program TWISTER reveals a structural mechanism for stutter compensation. *J Struct Biol*, 137(1-2):54–64, 2002.

[143] Yujie Sun, Osamu Sato, Felix Ruhnow, Mark E Arsenault, Mitsuo Ikebe, and Yale E Goldman. Single-molecule stepping and structural dynamics of myosin X. *Nat Struct Mol Biol*, 17(4):485–91, Apr 2010.

[144] D Svergun, C Barberato, and MHJ Koch. CRYSOL–a program to evaluate x-ray solution scattering of biological macromolecules from atomic coordinates. *Journal of applied crystallography*, 28(6):768–773, 1995.

[145] Tatyana M Svitkina, Elena A Bulanova, Oleg Y Chaga, Danijela M Vignjevic, Shinichiro Kojima, Jury M Vasiliev, and Gary G Borisy. Mechanism of filopodia initiation by reorganization of a dendritic network. *J Cell Biol*, 160(3):409–21, Feb 2003.

[146] Yasuharu Takagi, Rachel E Farrow, Neil Billington, Attila Nagy, Christopher Batters, Yi Yang, James R Sellers, and Justin E Molloy. Myosin-10 produces its power-stroke in two phases and moves processively along a single actin filament under low load. *Proc Natl Acad Sci U S A*, 111(18):E1833–42, May 2014.

[147] Hideyo Takatsuki, Elina Bengtsson, and Alf Månsson. Persistence length of fascin-cross-linked actin filament bundles in solution and the in vitro motility assay. *Biochimica et Biophysica Acta (BBA)-General Subjects*, 1840(6):1933–1942, 2014.

[148] Joseph Tcherkezian, Perry A Brittis, Franziska Thomas, Philippe P Roux, and John G Flanagan. Transmembrane receptor DCC associates with protein synthesis machinery and regulates translation. *Cell*, 141(4):632–644, 2010.

[149] Christopher Toepfer and James R Sellers. Use of fluorescent techniques to study the in vitro movement of myosins. *EXS*, 105:193–210, 2014.

[150] Hiroshi Tokuo and Mitsuo Ikebe. Myosin X transports Mena/VASP to the tip of filopodia. *Biochem Biophys Res Commun*, 319(1):214–20, Jun 2004.

[151] Hiroshi Tokuo, Katsuhide Mabuchi, and Mitsuo Ikebe. The motor activity of myosin-X promotes actin fiber convergence at the cell periphery to initiate filopodia formation. *J Cell Biol*, 179(2):229–38, Oct 2007.

[152] Claudio Tonlolo and Ettore Benedetti. The polypeptide 3 10-helix. *Trends in biochemical sciences*, 16:350–353, 1991.

[153] Fumiko Toyoshima and Eisuke Nishida. Integrin-mediated adhesion orients the spindle parallel to the substratum in an EB1-and myosin X-dependent manner. *The EMBO journal*, 26(6):1487–1498, 2007.

[154] Y Y Toyoshima, S J Kron, E M McNally, K R Niebling, C Toyoshima, and J A Spudich. Myosin subfragment-1 is sufficient to move actin filaments in vitro. *Nature*, 328(6130):536–9, 1987.

[155] K M Trybus, Y Freyzon, L Z Faust, and H L Sweeney. Spare the rod, spoil the regulation: necessity for a myosin rod. *Proc Natl Acad Sci U S A*, 94(1):48–52, Jan 1997.

[156] Nobuhisa Umeki, Hyun Suk Jung, Tsuyoshi Sakai, Osamu Sato, Reiko Ikebe, and Mitsuo Ikebe. Phospholipid-dependent regulation of the motor activity of myosin X. *Nat Struct Mol Biol*, 18(7):783–8, Jul 2011.

[157] Ronald D Vale. Myosin V motor proteins: marching stepwise towards a mechanism. *J Cell Biol*, 163(3):445–50, Nov 2003.

[158] V Vasioukhin, C Bauer, M Yin, and E Fuchs. Directed actin polymerization is the driving force for epithelial cell-cell adhesion. *Cell*, 100(2):209–19, Jan 2000.

[159] Kevin C Vavra, Youlin Xia, and Ronald S Rock. Competition between coiled-coil structures and the impact on myosin-10 bundle selection. *Biophysical Journal*, 110(11):2517–2527, 2016.

[160] Danijela Vignjevic, Shin-ichiro Kojima, Yvonne Aratyn, Oana Danciu, Tatyana Svitkina, and Gary G Borisy. Role of fascin in filopodial protrusion. *J Cell Biol*, 174(6):863–75, Sep 2006.

[161] Danijela Vignjevic, Marie Schoumacher, Nancy Gavert, Klaus-Peter Janssen, Gloria Jih, Marick Laé, Daniel Louvard, Avri Ben-Ze'ev, and Sylvie Robine. Fascin, a novel target of beta-catenin-TCF signaling, is expressed at the invasive front of human colon cancer. *Cancer Res*, 67(14):6844–53, Jul 2007.

[162] V. V. Volkov and D. I. Svergun. Uniqueness of ab initio shape determination in small-angle scattering. *J. Appl. Cryst*, 36:860–864, 2003.

[163] W. F. Vranken, W. Boucher, T. J. Stevens, R. H. Fogh, A. Pajon, M. Llinas, E. L. Ulrich, J. L. Markley, J. Ionides, and E. D. Laue. The CCPN data model for NMR spectroscopy: development of a software pipeline. *Proteins*, 59(4):687–696, 2005.

[164] Jun-Jie Wang, Xiu-Qing Fu, Yu-Guang Guo, Lin Yuan, Qian-Qian Gao, Hua-Li Yu, Heng-Liang Shi, Xing-Zhi Wang, Wen-Cheng Xiong, and Xiao-Juan Zhu. Involvement of headless myosin X in the motility of immortalized gonadotropin-releasing hormone neuronal cells. *Cell Biol Int*, 33(5):578–85, May 2009.

[165] Tomonobu M Watanabe, Hiroshi Tokuo, Kohsuke Gonda, Hideo Higuchi, and Mitsuo Ikebe. Myosin-X induces filopodia by multiple elongation mechanism. *J Biol Chem*, 285(25):19605–14, Jun 2010.

[166] Kari L Weber, Anna M Sokac, Jonathan S Berg, Richard E Cheney, and William M Bement. A microtubule-binding myosin required for nuclear anchoring and spindle assembly. *Nature*, 431(7006):325–329, 2004.

[167] Zhiyi Wei, Jing Yan, Qing Lu, Lifeng Pan, and Mingjie Zhang. Cargo recognition mechanism of myosin X revealed by the structure of its tail MyTH4-FERM tandem in complex with the DCC P3 domain. *Proc Natl Acad Sci U S A*, 108(9):3572–7, Mar 2011.

[168] W Weissenhorn, A Carfí, K H Lee, J J Skehel, and D C Wiley. Crystal structure of the Ebola virus membrane fusion subunit, GP2, from the envelope glycoprotein ectodomain. *Mol Cell*, 2(5):605–16, Nov 1998.

[169] Hadley Wickham. *ggplot2: elegant graphics for data analysis*. Springer New York, 2009.

[170] William Wood and Paul Martin. Structures in focus–filopodia. *Int J Biochem Cell Biol*, 34(7):726–30, Jul 2002.

[171] Sarah Woolner, Lori L O'Brien, Christiane Wiese, and William M Bement. Myosin-10 and actin filaments are essential for mitotic spindle function. *The Journal of cell biology*, 182(1):77–88, 2008.

[172] W. Wriggers and P. Chacón. Using situs for the registration of protein structures with low-resolution bead models from x-ray solution scattering. *J. Appl. Cryst*, 34:773–776, 2001.

[173] Maneesh K Yadav, Luke J Leman, Daniel J Price, Charles L Brooks, 3rd, C David Stout, and M Reza Ghadiri. Coiled coils at the edge of configurational heterogeneity. structural analyses of parallel and antiparallel homotetrameric coiled coils reveal configurational sensitivity to a single solvent-exposed amino acid substitution. *Biochemistry*, 45(14):4463–73, Apr 2006.

[174] Maneesh K Yadav, James E Redman, Luke J Leman, Julietta M Alvarez-Gutiérrez, Yanming Zhang, C David Stout, and M Reza Ghadiri. Structure-based engineering of internal cavities in coiled-coil peptides. *Biochemistry*, 44(28):9723–32, Jul 2005.

[175] Changsong Yang and Tatyana Svitkina. Filopodia initiation: focus on the Arp2/3 complex and formins. *Cell Adh Migr*, 5(5):402–8, 2011.

[176] Hongquan Zhang, Jonathan S Berg, Zhilun Li, Yunling Wang, Pernilla Lång, Aurea D Sousa, Aparna Bhaskar, Richard E Cheney, and Staffan Strömblad. Myosin-X provides a motor-based link between integrins and the cytoskeleton. *Nat Cell Biol*, 6(6):523–31, Jun 2004.

[177] Yongwei Zhang, Uwe Werling, and Winfried Edelmann. Seamless ligation cloning extract (SLiCE) cloning method cloning method. *Methods Mol Biol*, 1116:235–44, 2014.

[178] Hongxia Zhao, Anette Pykäläinen, and Pekka Lappalainen. I-BAR domain proteins: linking actin and plasma membrane dynamics. *Curr Opin Cell Biol*, 23(1):14–21, Feb 2011.

[179] Xiao-Juan Zhu, Cheng-Zhong Wang, Peng-Gao Dai, Yi Xie, Ning-Ning Song, Yu Liu, Quan-Sheng Du, Lin Mei, Yu-Qiang Ding, and Wen-Cheng Xiong. Myosin X regulates netrin receptors and functions in axonal path-finding. *Nature Cell Biology*, 9(2):184–192, 2007.

[180] Sally H Zigmond. Formin-induced nucleation of actin filaments. *Curr Opin Cell Biol*, 16(1):99–105, Feb 2004.

[181] Dennis Zimmermann, Alicja Santos, David R Kovar, and Ronald S Rock. Actin age orchestrates myosin-5 and myosin-6 run lengths. *Curr Biol*, 25(15):2057–62, Aug 2015.

APPENDIX: BACULOVIRUS DESIGN AND CLONING

The target plasmid pBlueBac His C was linearized using BamHI-HF (New Englage Biolabs). A modified SLiCE cloning reaction with 3 units of T5 Exonuclease (Epicentre Biotechnologies) added was performed to clone the myosin-10 constructs into the pBlueBac His C vector in a fashion that removed the 6xHis tag and all the extra residues that were between the start codon and the multiple cloning site. Baculovirus constructs of the resulting BlueBac vectors with the motor domains were made using the BestBac 2.0 kit following the manufacturer's directions (Expression Systems).

The myosin-10 ROP motor construct was created using the previously described construct used by Nagy *et al.* for the single molecule stepping for the DNA template for the motor feet, IQ, and SAH domains [108]. The pBiEx3BS [123] vector containing this motor sequence linearizes in the middle of the M10short-GCN4 coiled-coil sequence using AflII (New England Biolabs). The ROP domain was created using a gBlock (Integrated DNA Technologies) with the protein sequence reverse translated from the ROP sequence deposited in the PDB as 1ROP [8]. The ROP gBlock was PCR amplified following the manufacturer's instructions before being used as the cloning insert for the previously described SLiCE cloning method [177]. The myosin-10 M10short-GCN4 and myosin-10 ROP motor constructs were then PCR amplified from the pBiEx3BS vectors.